

January 2012

Development of a Reliable Metal-Insulator-Metal Bilayer Tunnel Junction for Wideband Detectors

Rudraskandan Ratnadurai

University of South Florida, rratnadu@mail.usf.edu

Follow this and additional works at: <http://scholarcommons.usf.edu/etd>

 Part of the [Electrical and Computer Engineering Commons](#), and the [Materials Science and Engineering Commons](#)

Scholar Commons Citation

Ratnadurai, Rudraskandan, "Development of a Reliable Metal-Insulator-Metal Bilayer Tunnel Junction for Wideband Detectors" (2012). *Graduate Theses and Dissertations*.
<http://scholarcommons.usf.edu/etd/4394>

This Dissertation is brought to you for free and open access by the Graduate School at Scholar Commons. It has been accepted for inclusion in Graduate Theses and Dissertations by an authorized administrator of Scholar Commons. For more information, please contact scholarcommons@usf.edu.

Development of a Reliable Metal-Insulator-Metal Bilayer Tunnel Junction for Wideband
Detectors

by

Rudraskandan Ratnadurai

A dissertation submitted in partial fulfillment
of the requirements for the degree of
Doctor of Philosophy
Department of Electrical Engineering
College of Engineering
University of South Florida

Co-Major Professor: Elias Stefanakos, Ph.D.
Co-Major Professor: Yogi Goswami, Ph.D.
Andrew Hoff, Ph.D.
Dennis Killinger, Ph.D.
Shekhar Bhansali, Ph.D.

Date of Approval:
November 19, 2012

Keywords: Sputtering, MIM, Tunneling, Multi Frequency Detection, Sensing

Copyright © 2012, Rudraskandan Ratnadurai

DEDICATION

To all the failures I encountered during this course that proved to be stepping stones. To all the dreams that inspired me to pick myself up from every fall and turn failures into successes.

ACKNOWLEDGMENTS

I would like to thank my professors Dr. Stefenakos, Dr. Goswami and Dr. Bhansali for giving me the opportunity to work under them and developing cutting edge research. Their support when situations became tough is immeasurable. I would also like to thank Dr. Hoff, for giving his consult at short notice and Dr. Killinger for serving as a committee member. I especially would like to thank my mentor Dr. Krishnan and Dr. Koiry for endless brainstorming sessions that led to many interesting developments in the project. The bulk of the fabrication which involved sputtering would not have been possible without the help of Kevin Luongo who went to great lengths to help me repair and modify the sputtering system during breakdowns. My heartfelt thanks to Joe Register and Justin Boone for helpful suggestions and support. The RF measurements which determined the applicability of the research would not have been possible without Scott Skidmore's inestimable help at the last minute. Thanks to Rob Tufts, Rich Everly, Dr. Yusuf Emirov and Jay Bieber for training and allowing me to use their facility. Their help will not go unnoticed. A huge thank you to Michael Konrad for helping me bring near dead systems back to life. I would also like to extend my gratitude to Ginny and Barbara for the helping with administrative tasks and express orders. Last but not least, I would like to express my sincere appreciation to Michael Celestin for being the devil's advocate

and helping me see the other side of the coin and to Supriya Ketkar whose immense support both intellectually and emotionally will never be forgotten.

TABLE OF CONTENTS

LIST OF TABLES	iii
LIST OF FIGURES	iv
ABSTRACT.....	viii
CHAPTER 1: INTRODUCTION	1
1.1 Overview of MIM Junctions	1
1.2 Goals and Objectives	4
1.3 Organization of Manuscript	5
CHAPTER 2: BACKGROUND.....	7
2.1 Single Layer MIM Junctions	9
2.2 Multilayered MIM Junctions	10
2.3 Motivation.....	13
CHAPTER 3: OPERATION OF MIM TUNNEL JUNCTIONS	20
3.1 Intrinsic Working	20
3.2 Wentzel Kramer Brillouin (WKB) Model	22
3.3 Brinkman Dynes Rowel (BDR) Model.....	22
3.4 Simmons Model.....	23
3.5 Other Models	26
3.6 Resonant Tunnel Model For Multilayered Tunnel Junctions	31
CHAPTER 4: DEVELOPMENT OF MIM TUNNEL JUNCTIONS	34
4.1 Processing Techniques.....	35
4.2 Optimization of the Dielectric Layer	42
CHAPTER 5: EVOLUTION OF MIM TUNNEL JUNCTION DESIGNS	58
5.1 Generation 1- Stacked Design (SK).....	58
5.2 Generation 2- Stepped Design (ST).....	61
5.3 Generation 3- Spaced Design (SP)	64
CHAPTER 6: DEVICE CHARACTERIZATION	69
6.1 DC and Low Frequency Measurements.....	69
6.2 RF Measurements	83
CHAPTER 7: CONCLUSIONS AND RECOMMENDATIONS FOR FUTURE WORK	91

7.1 Future Outlook	92
REFERENCES	95
APPENDICES	106
Appendix A: Process Flow of SK Design.....	107
Appendix B: Process Flow of ST Design	111
Appendix C: Process Flow of SP Design	116
Appendix D: Matlab Code for Simmons Fit.....	122
Appendix E: Labview Program for Electrical Measurements – Front Control Panel	137
Appendix F: Permissions	138

LIST OF TABLES

Table 1 Rectification ratios of various MIM tunnel junctions in literature	18
Table 2 Table of metals with work function difference.....	41
Table 3 Roughness characterization of NiO films deposited at various oxygen concentrations	53
Table 4 Effective barrier of the devices when fitted with the FN model.....	77
Table 5 Summary of the measured rectified current from each device.	90
Table 6 Possible design of experiments to better characterize the bilayer and single layer devices.	94

LIST OF FIGURES

Figure 1. Side view of a typical MIM sandwich device	9
Figure 2. MIM with same metal electrodes (0V Bias).....	9
Figure 3. Working theory of semiconducting tunnel diodes [46-48].....	11
Figure 4. Band structure for a multilayered MIM tunnel junction.	12
Figure 5. Application map of tunnel junction based rectennas.....	17
Figure 6. RF power levels of current state of the art devices operating up to 1THz.	18
Figure 7. Energy band diagram of an MIM device with different electrodes.....	25
Figure 8. Illustration of different types of tunneling.....	28
Figure 9. Output current of a tunnel junction w.r.t film thickness [98].....	31
Figure 10. Electron tunneling probability in a bi-layered tunnel junction as a function of energy	32
Figure 11. Illustration of whisker diode.....	34
Figure 12. Crosshair type design of the tunnel junction.....	36
Figure 13. Edge diode structure	37
Figure 14. Illustrations of various artifacts edges created on the edges during fabrication of an MIM diode.....	38
Figure 15. Energy band diagram of an MIM tunnel junction using two dissimilar metals	39
Figure 16. Energy band diagram of an MIM tunnel junction using two dissimilar metals at applied voltage V_{bias}	39
Figure 17. Illustration of completed and distorted lattices	43
Figure 18. Schematic of a reactive sputtering process.....	46
Figure 19. Fitted XRR spectrum of film deposited at 20% O ₂ partial pressure for 30mins.....	48

Figure 20. Fitted XRR spectrum of film deposited at 33% O ₂ partial pressure for 30mins.....	48
Figure 21. Fitted XRR spectrum of film deposited at 40% O ₂ partial pressure for 30mins.....	49
Figure 22. Plot of sputtering rate as a function of Oxygen concentration	49
Figure 23. XRD spectra of films deposited with different Oxygen partial pressures.....	50
Figure 24. Roughness as a function of O ₂ concentration during deposition.....	51
Figure 25. Starting from top left going clockwise, AFM images of NiO films deposited at 0%, 20%, 33%, 40%, 80%, 100%	51
Figure 26. XRD spectrum of ZnO film showing strong c-axis orientation	54
Figure 27. Reflectance mode UV-Vis spectra of NiO film, ZnO film and the bilayer film.....	55
Figure 28. Band gap determination of NiO film, ZnO film and their combination.....	56
Figure 29. Energy band diagram of a Ni/NiO/ZnO/Cr bilayered tunnel junction device.	57
Figure 30. Side view schematic of the SK design.	59
Figure 31. Process schematic of the SK device.	59
Figure 32. Sideview schematic of ST design.....	62
Figure 33. Optical image of ST design	62
Figure 34. Process schematic of the ST design.....	63
Figure 35. (top) Optical image of the SP design; (bottom) Side view schematic of the SP design.....	65
Figure 36. Overall layout of mask showing the functions of each feature	66
Figure 37. Process flow schematic of the SP design	67
Figure 38. (top) Cross section schematic of parasitic capacitance due to spacer layer.....	68
Figure 39. Four wire measurements of the spacer device.....	68
Figure 40. Cascade Probestation with Keithley 2400 Sourcemeter used to conduct DC measurements of the devices.....	70
Figure 41. Schematic of the electrical measurement setup.....	71

Figure 42. I-V responses for different top electrodes Ni, Al and Cr.	71
Figure 43. I-V responses of devices fabricated with different oxygen partial pressures.....	72
Figure 44. Sensitivities of each device at their fabricated oxygen partial pressures.	72
Figure 45. Sensitivities of the device plotted with respect to oxygen partial pressure.	73
Figure 46. I-V Responses for all 3 generations of devices.	73
Figure 47. Simmons fit of the 3 devices: (a)Stacked; (b) Stepped: and (c) Spaced.	74
Figure 48. Comparison of I-V responses of devices fabricated with individual films as the insulator layer and the combination of the two.	76
Figure 49. FN fit of the devices.	76
Figure 50. TAT fit of the devices.....	77
Figure 51. Modified chuck of Signatone system to allow liquid nitrogen to be used as a coolant.	78
Figure 52. Plot of $\log(J/V)$ as a function of temperature at different bias voltage of the Bilayer device.	79
Figure 53. Schematic of the low frequency measurements setup.	80
Figure 54. Rectification using the bilayer device at 500Hz.....	80
Figure 55. Rectification using the bilayer device at 5 kHz.....	81
Figure 56. Rectification using the bilayer device at 50 kHz.....	81
Figure 57. Rectification using the bilayer device at 5 MHz.	82
Figure 58. Comparison of sensitivity Vs turn on voltage of the NiO, ZnO and Bilayer based devices.....	82
Figure 59. Classification of fabricated devices in this research towards application in high frequency detection.....	83
Figure 60. RF Measurement Setup used to detect rectified current with applied bias.	85
Figure 61. Detected current from NiO devices.	86
Figure 62. Detected current from ZnO devices.	86
Figure 63. Detected current from Bi-layered devices.....	87

Figure 64. Closeup of the Bilayer devices at 1GHz and 10GHz with 1mW and 316 μ W of input power	87
Figure 65. (a) Current vs frequency analysis of NiO, ZnO and bilayer devices with 1mW input power	88
Figure 66. (a) Output power vs frequency analysis of NiO, ZnO and bilayer devices with 1mW input power	88
Figure 67. (a) Efficiency vs frequency analysis of NiO, ZnO and bilayer devices with 1mW input power	89

ABSTRACT

Detectors and sensors are an integral part of modern electronics and are crucial to highly sensitive applications. Metal-Insulator-Metal (MIM) tunnel junctions have been explored for the past five decades and are still being investigated due to its wide use of applications such as mixers, capacitors, detectors, rectifiers and energy conversion devices. In this research, various designs of thin film based tunnel junctions have been investigated and the optimum one picked for the purpose of a wide band detector up to 10GHz based on their sensitivities. A modified design with an isolation layer incorporating a self-aligning method to increase fabrication throughput was developed. A mask for the reliability testing of multiple devices with different areas was also developed. Nickel Oxide based insulators with different stoichiometries have been incorporated in the fabrication of the device to identify which stoichiometry gives the best performance for high frequency applications. Nickel Oxide (NiO), Zinc Oxide (ZnO) and the combination of the two have been deposited using reactive sputtering and investigated as insulator materials. The bilayer devices showed increased sensitivities at lower turn on voltages and very good efficiencies at 100MHz and 1GHz. Although, the MIM device provides a simple structure, some of the critical parameters required to quantify the device functionality are still being explored. Based on the parameters, a criterion was developed to help engineer a tunnel device for a desired detectivity.

CHAPTER 1: INTRODUCTION

Metal-Insulator-Metal (MIM) tunnel junctions have been studied since the 1950s starting with Leo Esaki who invented the Esaki diode. Metal-Insulator-Metal (MIM) tunnel junctions, also known as Metal-Oxide-Metal (MOM) or Metal-Barrier-Metal (MBM) tunnel junctions are essentially sandwich structures consisting of a metal electrode, a thin dielectric layer and an additional metal electrode. MIM junctions have been investigated since the late forties and early fifties [1]. MIM is a device which works on the principle of quantum tunneling whereby electrons tunnel through the insulating barrier from one metal electrode to the other. With the turn of the century, the window of useful frequencies in the electromagnetic spectrum widened considerably. There was a need for technology being able to operate at higher frequencies and many breakthroughs were made with electronic materials one of them being the tunnel diode. The tunnel diode surpassed normal diodes in that tunnel diodes have very high switching speeds and sensitivities [2]. It was first successfully demonstrated by Leo Esaki (Esaki Reiona) in August 1957 [3, 4] which marked a new era for electronic devices.

1.1 Overview of MIM Junctions

There are a multitude of applications for the MIM tunnel junction such as magnetic tunnel junctions (MTJ) [5], capacitors [6], waveguides [7] and rectifiers[8, 9],

the latter being quite a new research field. MTJs utilize electrons as a source of current on the application of a magnetic field and the MIMs utilize the tunneling of electrons as a current source on the application of an electric field. Shortly after the discovery by Esaki, many groups experimented on the magnetic effects of MIMs and the MTJs were born. In the seventies, IBM developed the first MTJ for MRAM applications thus paving a way to store data without an applied voltage[10]. The rectifying behavior of MIMs led them to be investigated as energy conversion devices comprising of detectors and energy harvesters where detectors use external circuits to amplify the rectified signal, and energy harvesters utilize the rectified signal as usable power. Around the time of the development of MTJs by IBM, groups such as Gustafson et al [4, 11-13] were working on detection and mixing of infrared (IR) and optical frequencies using MIM as a diode [14-18], because Metal-Insulator-Metal tunnel junctions had gained increased popularity due to their ability to exhibit extremely low turn on voltage in “diodic” operations. MIM diodes do not operate like normal semiconductor tunnel diodes since tunnel diodes exhibit negative resistance and MIMs don’t, except in special conditions[19]. As far as the literature shows, Frank et al [6] produced in 1968 Metal-Insulator-Semiconductor (MIS) and MIM capacitors using reactive sputtering as a method of fabrication for silicon ICs. While there have been other rectifiers available to compete with MIM junctions, it is undeniable that due to its simplistic architecture and its ability to operate at high frequencies, it is unbeatable in device performance. This was one primary reason great attention was given to this particular device in the seventies and today. Superconductor-Insulator-Superconductor (SIS) devices [20, 21] have also been used as quantum detectors and mixers but will not be discussed as it is outside the scope of this work.

In particular the MIM junction is being investigated for its applications in energy conversion devices such as infrared and optical detection. The MIM junction as an energy-harvesting device and infrared (IR) detector is a new and upcoming research field. By coupling an antenna, designed for the THz frequency range, to the MIM tunnel junction, one can rectify IR radiation to derive usable power from the device. Whether it is used as a capacitor, resistor or diode, it can be surmised that the four main aspects of the MIM, that is, top electrode, insulating layer, bottom electrode, geometry[22] and configuration play crucial roles in the working efficiency of the device. The Proper selection of the two electrodes determines whether the MIM's I-V response is asymmetric or symmetric. Asymmetry cannot be the only governing reason for choosing the right electrode materials since the compatibility of the metals with that of the insulator is important. Lattice mismatch between the metal and insulator layer, and delamination are issues one has to contend with. The insulating layer must also be conditioned to facilitate conduction (tunneling) of electrons. When fabricating the insulating layer, non-uniformities and pinholes can lead to non-repeatability and shorter device life time. Since the MIM is essentially a stacked device, careful fabrication of subsequent layers is imperative to the working of the device. Artifacts caused during fabrication techniques such as liftoff and etching can cause detrimental effects to the proper working of the device. Oxygen vacancies lead to electron traps and the intermittent operation of the device, thereby leading to the conclusion that not only the conditions while fabricating the insulator as well as the remaining layers affect the device performance. While performing electrical characterization of the device, improper positioning of probes, puncturing of the electrodes or voltage annealing can lead to

skewed or false results. Literature search on MIM diodes for rectification at THz frequencies shows that proper understanding of the rectification process still needs to be developed. There is also a need to establish a well-defined link between the mathematical modeling and the choice of dielectric materials in order to achieve a high current output from the device.

Even though there are many other constraints in the development of a MIM based energy conversion device, such as, impedance matching and antenna response, the objective of this research focuses on the rectification response (sensitivity) and tunneling mechanisms with respect to the dielectric layer characterization which influences the reliability of the tunnel junction.

1.2 Goals and Objectives

The main goal of this research was to obtain a device with a high efficiency/sensitivity. Towards this goal, the specific objectives are as follows:

- (i) To tune the dielectric so as to increase the asymmetry of the diode- To achieve good diodic behavior, not only must the work function difference of the two metals be large, but the dielectric must also facilitate better electron transport in one direction. Insulators with different oxygen concentrations would affect the electron transport through the barrier. Bilayer insulators used in the tunnel junctions might be able to accomplish this due to resonant tunneling.

- (ii) To develop a reliable MIM tunnel junction that can be integrated with an antenna with a Co-Planar Waveguide feed. Since the primary use of the tunnel junction is to be used like a diode for detection of radiation, it has to be seamlessly integrable with an antenna designed for the detecting frequency.
- (iii) To investigate the tunneling mechanism in a bi-layered tunnel device- Various tunneling mechanisms such as Fowler-Nordheim tunneling and trap assisted tunneling. DC electrical measurements are carried out at various temperatures and the results fitted with various tunneling models to determine the tunneling mechanism.
- (iv) To determine the efficiency of the tunnel device in a wide range of frequencies- For the device to be effectively used as a wide band detector/sensor, the output power must be significant to derive any usable signal.

1.3 Organization of Manuscript

Chapter two discusses in detail single layer and bilayer tunnel junctions, stating the properties, advantages and shortcomings of each. The motivation for this research and the current state of the art of devices operating at very high frequencies are also presented in this chapter. In chapter three, the operation of the tunnel junction with its various tunneling mechanisms and models are discussed. The band diagrams of the NiO only based devices and the NiO/ZnO bilayer based devices are also introduced. Chapter four

gives a brief overview of the development of MIM tunnel junction devices in general with major concentration on the optimization of the insulator layer used in developing the tunnel junction devices described in this research. Various oxygen concentrations used to fabricate the NiO layer and its material properties will be presented. The ZnO characteristics and the NiO/ZnO bilayer bandgap measurements will also be discussed. It is interesting to ascertain that the combined bandgap of the bilayer is smaller than the individual ones. This suggests that a natural quantum well is produced at the interface. Chapter five describes in detail the evolution of MIM tunnel junction based rectifying devices fabricated and studied in this research. The design and fabrication of a simple stacked device, its pitfalls and lessons learned leading to the design and fabrication of the optimized spaced device are discussed in detail. Chapter six presents and analyzes the results of the designed and fabricated devices. In section 6.1 the responses of the devices operating from DC to 5kHz are presented illustrating the rectifying behavior of NiO, ZnO and bilayer devices. In section 6.2, the high frequency response of the devices is presented and the results are compared for 3 different dielectrics.

CHAPTER 2: BACKGROUND

The MIM junction, used for detection and mixing of infrared (IR) and optical radiation, was initially investigated by Frayne et al [18] and Dees et al [23]. A point contact configuration also known as the cat-whisker diode configuration was used for the detection and characterization experiment. However, due to its poor stability and reproducibility, other detectors such as thermopiles or bolometers were considered. Detectors prior to their introduction were mainly bolometers and bulk bimetallic contacts which relied heavily on liquid Helium as a cooling system [24, 25]. Bolometers, and later micro-bolometers, have a crippling disadvantage since they lack the required sensitivity and speed of response. Existing IR imaging/detection systems use focal plane arrays (FPA) which consist of an array of either thermopiles, bolometers, pyroelectrics [26] or biomaterial cantilevers [27] to detect temperature changes in the form of voltage change, carrier density change, resistance or capacitance change. Although some very recent advances have been made with such IR imaging devices, the underlying principle poses a problem; they all rely on the temperature change of the detecting material. The pyroelectric responses of each material must be taken into account when choosing them and even slight thermal noise can distort the output quality. The point contact diodes, and subsequently MIM diodes, eliminated the need for such cooling thereby heralding the era of un-cooled IR/photo detectors [15-17]. In this regard MIM based IR sensors can be

deemed superior since they do not rely on thermal effects for sensing and their response speeds are much higher than thermal based sensors. Matyi [9] proposed substituting each pixel of the FPA with double band nanoantennas that detect radiation in the Low IR and THz regions. Moreover, MIM based sensors can also operate in mm-wave regions and can detect signals which are not in the line of sight and under adverse weather conditions [8]. One must note that although the point contact diode can be regarded as an MIM diode, it is generally not referred to as such.

Metal-Insulator-Metal structures are also used as capacitors in MMICs for the increased capacitance they exhibit due to very thin high k dielectrics, and their excellent role in blocking the DC in MMICs [6, 28, 29]. The MIM tunnel junction can essentially be used for two purposes; that is, to allow electrons to tunnel through directly and/or under certain bias conditions, or to behave like a true capacitor and prevent leakage currents under certain bias conditions. Martin et al [7] also used an MIM like structure as a wave guide although it was quite unclear which materials were the metals and insulators. In the case of an MIM structure being used as a capacitor, the breakdown field is typically desired to be high and the insulating material to behave as close to an ideal insulator as possible. If the MIM structure is to be used as a tunneling junction, the insulating material would typically be very thin of the order of 50\AA or less. The operation of a MIM tunnel junction and the governing equations as well as the numerical models used to predict the junction behavior are discussed in the following section.

2.1 Single Layer MIM Junctions

A typical MIM, as its acronym suggests, is just a dielectric barrier sandwiched between 2 metal electrodes as shown in Fig. 1. The barrier can either be a native oxide of any one of the metal electrodes, or a non-native one. When a voltage is applied across the electrodes, electrons tunnel from one metal to the other through the insulating barrier layer. In a semiconductor tunnel diode, the thin heavily doped p-n junction creates a broken band-gap allowing electrons in the 'n' side to align with holes in the 'p' side. This reduced k-vector causes the electrons to tunnel over to the 'p' side which in turn allows for an increased current to flow when the applied voltage is very low. The MIM is similar in comparison but for the fact that the 'p' and 'n' type regions are electrodes and not semiconductors. In a way the semiconductor effect is being replicated here by using metal electrodes sandwiching a very thin barrier with the exception that very low turn on voltages can be acquired and usage at very high frequencies is possible.

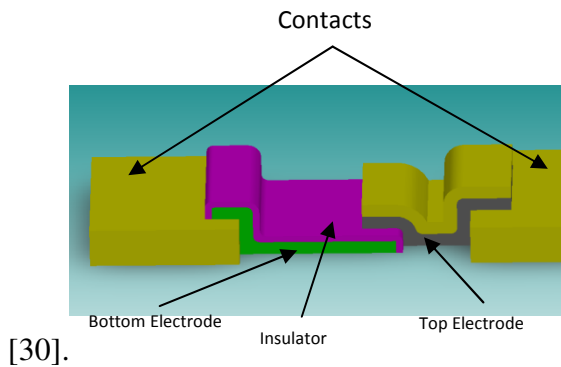


Figure 1. Side view of a typical MIM sandwich device

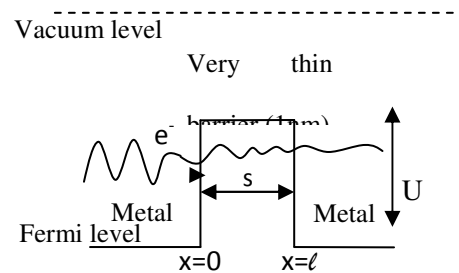


Figure 2. MIM with same metal electrodes (0V Bias)

If the MIM is used to rectify high frequencies it must have a very high sensitivity and nonlinearity since it has to rectify very small amplitudes [31-35]. It also must have low impedance so that it can be matched with the antenna circuitry. For its use as an energy harvester, it has to exhibit high current near zero bias. In this case, the operation will greatly depend on the difference of the work functions, $\Delta\Phi$. However, $\Delta\Phi$ alone is not sufficient to overshadow the other characteristics of the MIM that limits its performance as a detector or harvester. The next section gives a brief overview of engineering the insulator layers to achieve high sensitivity, curvature (non-linearity) and asymmetry of an MIM tunnel junction.

2.2 Multilayered MIM Junctions

The single layer MIM tunnel junction is a revolutionary device in its own right, since unlike semiconductors, the usage of oxides as an insulating layer allows an easier way to directly control how electron transport takes place. Also, the manufacture of such devices is far easier, compared to other semiconductor based devices, as will be seen in chapter four. Nevertheless, the single layer MIM tunnel junction is limited by its work function difference and the properties of the dielectric at high operating frequencies. In an effort to enhance the tunneling mechanism and thereby the electron transport, multilayered MIM tunnel junctions have been developed [31-38]. So far there is limited development on multilayered tunnel junctions for detectors and energy harvesters [31, 33, 34, 37, 39], instead such tunnel junctions have been extensively used as magnetic tunnel junctions for sensors, and Magnetic Random Access memory (MRAM) devices [40-45].

The multilayered tunnel junction mainly utilizes the resonant tunneling effect that was established by Esaki in 1974 [3] and is more frequently called Resonant Tunnel Diode (RTD). The p-n junction tunnel diode exhibits a negative differential resistance in its Current-Voltage response which proved to be very useful in amplifiers and high frequency triggers. The theory is as depicted below:

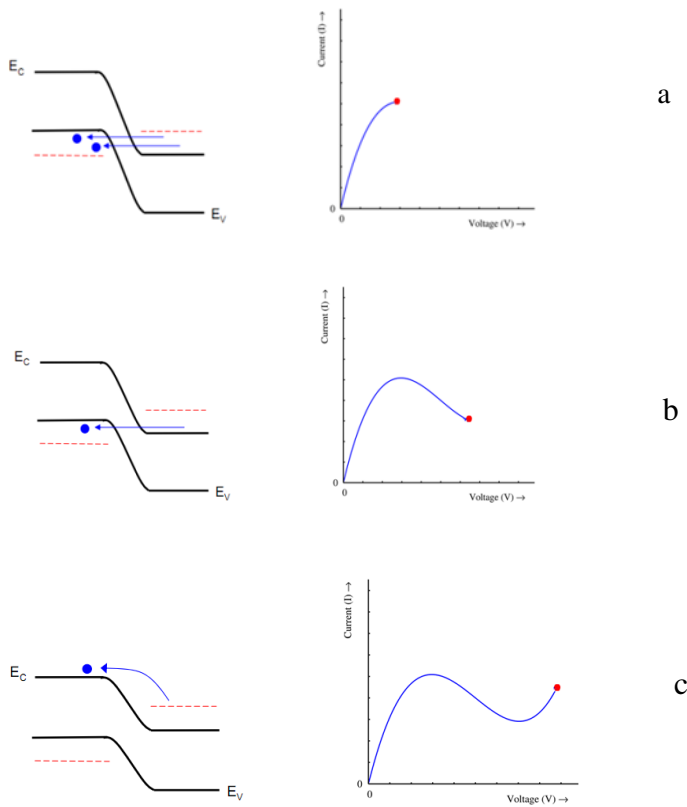


Figure 3. Working theory of semiconducting tunnel diodes [46-48]

In Fig. 3 the depletion layer acts as a thin barrier enabling tunneling to take place. (a) The barrier thickness is low and therefore charge carriers tunnel spontaneously or with little applied bias. (b) With an increase in bias, the barrier thickness increases and therefore the tunneling current decreases exhibiting negative differential resistance

(NDR). (c) When the applied bias increases even further, electrons start conducting thermionically. Typically quantum wells do not exist in such devices although defect densities could possibly induce such wells. The band structure for a multilayered tunnel junction is different as is seen in Fig. 4. A low bandgap insulator material is sandwiched between two high bandgap insulator materials which, on either side, are in ohmic contact with metals having different work functions. By tailoring the insulator layers and the configuration of the tunnel stack, quantum well(s) can be introduced where a two dimensional electron gas (2DEG) confinement occurs at the interface. At certain energies that resonate with the quantum wells' energy levels, a large tunneling probability occurs, leading to an increase in the tunneling current. These quantum wells can be physically defined and fabricated or exist in the presence of traps within the insulator or interface [32]. The tunneling in such a case can also be known as a trap assisted tunneling (TAT). Many groups have shown enhanced rectification and increased responsivities using multilayered MIM tunnel junctions [31-34, 37, 39].

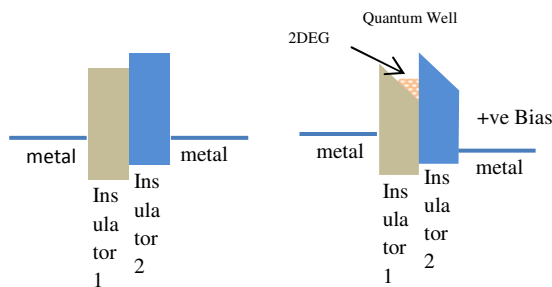


Figure 4. Band structure for a multilayered MIM tunnel junction. This picture depicts a bi-layered device

RTDs typically exhibit NDR, however NDR effects may or may not be seen in oxide based Resonant Tunnel Junctions (RTJs). Many RTDs involving III-V semiconductors as the insulating materials display excellent NDR effects [48]. In this work, limited NDR effects have been noticed with the devices fabricated. More often it is observed in aged devices and therefore attributed to the formation of additional interfaces by diffusion over time consisting of a modified barrier.

2.3 Motivation

The need for clean energy sources has become ever more pressing compared to just a decade ago. Apart from the utilization of renewable energy sources, recycling and reuse of energy is also widely being investigated to eliminate loss and increase efficiency. To this end, solar cells seem to be a very widely used solution for harvesting energy from the sun with the highest efficiency so far being around 60% [49]. Although advances can still be made in coming years increasing the efficiency of solar cells, it is always desirable to develop higher efficiency energy conversion devices. Solar cells utilize the particle nature of light (photons) to excite electrons from the valence band to the conduction band of the solar cell material creating an electron-hole pair. This produces a current which can be harnessed as energy when allowed to pass through an external load. This mechanism of solar conversion can be very lossy since excited electrons thermally relax after the energetic photons transfer their energy to them [31].

In a different concept, the rectenna, instead of using the particle nature of light involving inelastic collisions, one could use the wave nature of light. Electrons are able to resonate within the full length of the electromagnetic spectrum and therefore, designing

an antenna element that resonates at a particular frequency would cause the electrons in the Fermi level of the metal to oscillate at that frequency without almost any loss, provided the impedances are matched. When the antenna is coupled with a diode, the AC oscillations can be rectified to produce usable direct current. For this reason, rectennas have been viewed as promising devices for energy conversion.

Energy converters typically fall into two categories: namely, detectors and energy harvesters with the former being the most widely researched type of device. As mentioned in the introduction, rectennas can also be used as detectors/sensors without depending on a zero-bias current when biased at operating suitable operating voltage. The concept of harnessing microwave power into usable energy was first conceived at Raytheon in the nineteen sixties with a GaAs/Pt Schottky barrier diode based rectenna element and demonstrated an efficiency of 90.6% [50]. The highest conversion efficiency so far (albeit at very high power and at 2.5GHz) has been reported to be around 85%-90% [51]. Yoo et al [52] demonstrated efficiencies of 39% to 60% by using GaAs Schottky diodes coupled with antennas operating at 35GHz and 100mW output power. Devices operating at higher efficiencies, very high frequencies and very low power still need to be developed. Subsequently thin film rectenna arrays were developed sporting efficiencies of 85% for detecting microwave radiation with high power [53, 54]. The use of the MIM as an energy harvesting device can be regarded as a spinoff from its original use as an IR detector. The MIM device would be able to scavenge or harvest usable power from primary and stray sources, such as thermal energy (solar, blackbody radiation or other kinds of waste heat) [55]. Since thermal (IR) radiation falls in the THz frequency range, antennas that are designed to capture THz radiation can be coupled to MIM diodes

to produce IR rectifying devices. Theoretically, MIM based rectennas could be more advantageous compared to solar cells in harnessing power from the sun. However there are many serious issues one must address and resolve before this can be realized.

MIM detectors on the other hand have been developed and studied since the nineteen seventies, with their frequencies of detection ranging from 50MHz to UV [4, 9, 11, 13, 14, 17, 21, 23, 56-69]. The essential difference between an energy harvesting MIM device and a detecting MIM device is that the turn-on voltage for the former should be zero or near zero meaning that the efficiency must be almost 100% which is practically impossible. The separating line between a harvester and a detector can be modified depending on how much of the obtained power one considers as useful. By maximizing the voltage derived from the antenna(s) and reducing the power output expectations from the diode, a rectenna may be operated as an energy harvester. On the other hand, it can be used as a detector or sensor by merely amplifying the signal derived from the diode.

Whether it is used in energy harvesting or detection, there are essentially 4 characteristics or features of the MIM diode that are crucial to its optimized operation. They are: asymmetry, resistivity, non-linearity and sensitivity. These features are inter-dependent upon one another and also upon the MIM's electrodes, insulator, geometry and process parameters. The sensitivity of the device is the deciding factor of whether the device can be used as an energy harvester, detector or linear rectifier and is defined as the current rectified by the device per unit of incident RF power [33]. It is defined mathematically as the ratio of the differential conductance to the non-linearity of the device and is given by I'/I'' where I' is the differential conductance calculated as

dI/dV and I'' is the non-linearity calculated as d^2I/dV^2 . A linear rectifier is a simple AC to DC converting device that operates in the order of kHz to tens of MHz.

The applications of tunnel junction based rectennas can be easily understood from the application map shown in Fig. 5. The turn-on voltage which is related to the non-linearity defines the voltage at which a large rectified current is produced by the device. For a device to behave as an energy harvester, the antenna element should also be able to deliver to the diode as high a voltage as possible. Unfortunately it is difficult to obtain a large voltage at very high frequencies because of the radiation small signal amplitude. Therefore the diode has to be able to exhibit a very high sensitivity and a very low turn on voltage. For the device to be used as a detector, the constraint on the turn on voltage and sensitivity is less since the device can be biased by an external power source and therefore the sensitivity need not be very high. However, a detector with too low a sensitivity would not be desirable. For the device to be used as a linear rectifier, the requirements for a high turn on voltage and sensitivity are more relaxed. Such devices can be used as basic rectifying diodes or in oscillator circuits. The advantages of such devices are that they are very easy to fabricate compared to CMOS devices which involve a multitude of steps such as diffusion, doping and thermal treatments. The need for rectenna detectors is as great as is the need for energy harvesters. Millimeter wave and higher frequency detectors are used in a number of applications ranging from medical imaging to security and surveillance [70, 71].

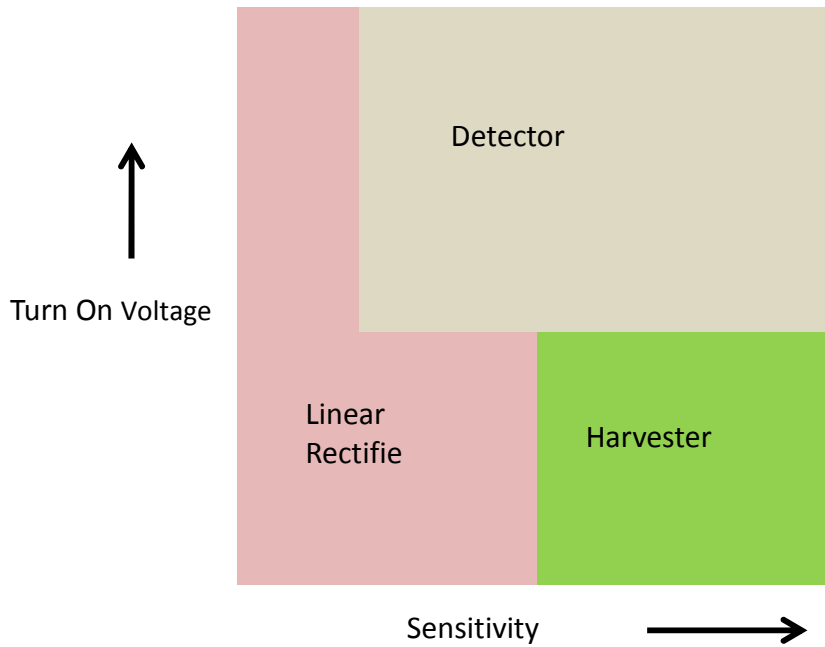


Figure 5. Application map of tunnel junction based rectennas

There are many devices operating in the frequency range of 10GHz to 1THz, such as impact avalanche transit time (IMPATT) diodes [72], Gunn diodes [73], tunnel injection transit time (TUNNETT) diodes [74], Heterojunction bipolar transistors (HBT) [75], high electron mobility transistors (HEMT) [76], Schottky diode chains [77] and RTDs [78, 79]. A comparison of current state of the art tunneling diodes presently being used up to 1THz is shown in Fig. 6. One can discern that RTDs and Schottky diodes seem to be the best choices for higher frequencies. The work presented in this dissertation continues along this path involving Resonant Tunnel Junctions (RTJs) with an aim to further the state of the art of devices operating in the near-IR and IR regions. Table 1 highlights the asymmetry characteristics of various tunnel junctions in literature.

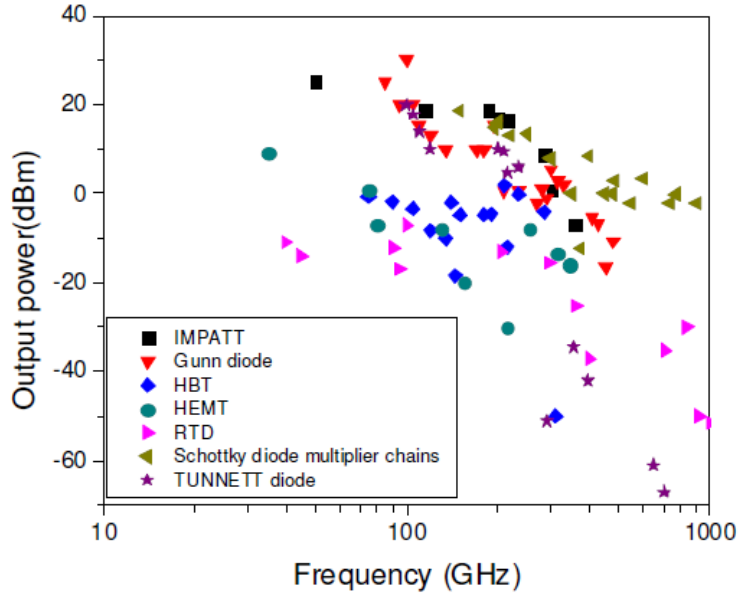


Figure 6. RF power levels of current state of the art devices operating up to 1THz. Reprinted with permission [48]

Table 1 Rectification ratios of various MIM tunnel junctions in literature

MIM Configuration	η	Reference
Al/Al ₂ O ₃ /Al	1	[58]
Ni/NiO/Pt	3.6	[58]
Al/Al ₂ O ₃ /Al	1	[80]
Al/Al ₂ O ₃ /Sn	1	[80]
Al/Al ₂ O ₃ /Pt	2	[57]
Ti/TiO ₂ /Ti	1.3	[81]
Ti/TiO ₂ /Pt	1.5	[55]

Table 1: (Continued)

Cr/Cr ₂ O ₃ /Au	For Ni-Au junction- 2	[17]
Ni/NiO/Au	For Cr-Au junction- 2.2	
ZrCuAlNi/Al ₂ O ₃ /Al	~100	[82]
Ni/NiO/Cr/Au	3.5	[83]
Ni/NiO/Ni	1	[11]
Nb/NbO _x /Ag	1.1	[84]
Ta/SiO ₂ /Ta	1	[85]
Cr/Cr ₂ O ₃ /Al ₂ O ₃ /Ag	1:2000 @400mV	[31]
W/Nb ₂ O ₅ /Ta ₂ O ₅ /W	~1:16 @450mV	[33]
Cr/Al ₂ O ₃ /HfO ₂ /Cr	1:10 @ 2V	[34]
Cr/Hf ₂ O ₃ /Al ₂ O ₃ /Cr ₂ O ₃ /Cr	1:1750 @ 4V	[37]

CHAPTER 3: OPERATION OF MIM TUNNEL JUNCTIONS

3.1 Intrinsic Working

As mentioned previously, the MIM junction works on the principle of quantum tunneling, where an electron crosses a barrier even though its energy is smaller than that needed to surmount the barrier. The barriers mentioned are walls of a potential well. Quantum tunneling utilizes the dual nature of a particle (an electron in the present case) postulated by the quantum theory [86]. The electron is considered a wave when it traverses through the barrier and the solution to that wave function is given by the Schrodinger's wave equation from which the transmission coefficient of the tunneling electron can be obtained. In the following discussions, the electron is considered a wave packet given by

$$\psi(x) = A \sin\left(\frac{2\pi x}{\lambda}\right) = A \sin(kx) \quad (1)$$

Where

$$k = \left(\frac{2\pi}{\lambda}\right) \quad (2)$$

Let us consider an ideal rectangular barrier as shown in Fig. 2. U is the potential energy of the barrier with the Fermi level of each metal generally aligned to one another. If there is a difference in work function between the two metals, band bending would take place giving rise to a trapezoidal barrier.

The Schrodinger time independent equation for a wave packet moving along the x-axis is given as

$$\frac{d^2\psi}{dx^2} = -\left(\frac{2m}{\hbar}\right)(E-U)\psi(x) \quad (3)$$

Where

$$\hbar = \frac{h}{2\pi}$$

The complex wave function $\psi(x)$ can be solved from equation 3 and is given as

$$\psi(x) = \{Ae^{ik_1x} + Be^{-ik_1x}\} \quad x \leq 0 \quad (4)$$

$$\psi(x) = \{Ce^{ik_2x} + De^{-ik_2x}\} \quad 0 \leq x \leq l$$

$$\psi(x) = \{Fe^{ik_1x}\} \quad a \leq l$$

Where k_1 and k_2 are wave numbers denoted as

$$k_1 = \frac{\sqrt{2mE}}{\hbar} \quad (5)$$

$$k_2 = \frac{\sqrt{2m(U_o - E)}}{\hbar}$$

The transmission coefficient of the electrons is given as [10]:

$$T = \exp\left\{\frac{-2}{\hbar} \int_0^l \sqrt{2m(U(x) - E)} dx\right\} \quad (6)$$

Most models on tunnel junctions are based on the transmission coefficient from which the current densities are approximated.

3.2 Wentzel Kramer Brillouin (WKB) Model

For barrier penetrability we use the Wentzel Kramers Brillouin (WKB) approximation which allows for more general calculations, where detailed barrier shape and possible resonances associated with reflections at the barrier faces are not taken into account [31]. The reasoning is that scattering and interface roughness make them insignificant although there is a disadvantage in using the WKB model that will be discussed shortly. The current density J according to the WKB approximation is given as [87],

$$J = \int_0^{E_m} D_T(E_x) \xi dE_x \quad (7)$$

If ϕ_B is the barrier height and x_2-x_1 the barrier width, then the probability $D_T(E_x)$ that an electron at energy level E_x can penetrate it is given as

$$D_T(E_x) = e^{-\left(\frac{4\pi}{h}\right) \int_{x_1}^{x_2} \sqrt{2m[\phi_B(x) - E_x]} dx} \quad (8)$$

ξ is called the supply function and ξdE_x represents the difference in the number of electrons incident on one side per second per unit area to those incident on the opposite side of the barrier having energy in the range E_x to E_x+dE_x .

3.3 Brinkman Dynes Rowel (BDR) Model

The WKB model set a precedent for future tunneling models such as the Brinkman-Dynes-Rowell (BDR) [88] and the Simmons models [89]. Rowell identified that the tunneling conductance can be approximated by a parabola with its axis offset

from zero bias, a phenomena they call zero bias anomalies [90]. This meant that tunneling took place even when no bias voltage was applied. This was more pronounced with asymmetric barriers. The tunneling current density is given as[56],[91]:

$$j = \frac{2e}{h} \iint \exp\left(-\frac{2}{\hbar} \int_0^s \sqrt{2m\phi(x,V,E)} dx\right) \times [f(E(k)) - f(E(k) - eV)] dE dk \quad (9)$$

Where, 's' is the barrier thickness, $\Phi(x,V,E)$ is the position dependent barrier height for bias V for an electron with incident energy E, e is the positive electron charge, m is the mass of a free electron, k are wave vectors parallel to the junction interface and f is the Fermi function. The drawback of the BDR model is that it failed to explain large offsets in the conductance minimum attributing its cause to contaminated junctions [90].

It is standard practice in MIM literature to use the WKB model for the electron tunneling probability and to use the Simmons model [92] to approximate the I-V curve. Furthermore, according to Miller et al [93] the negligence of the interface roughness inherent in the WKB model gives rise to quadratic tunneling conductance even at anomalously high biases; which causes serious discrepancies when applied into the full functional form of the model. It was theorized that the band structure of the barrier and the roughening of the interfaces seemed to give rise to unrealistic tunnel barrier parameters. As a result, a modification or deviation from the WKB model is desired.

3.4 Simmons Model

As far as modeling most MIM tunnel junctions, it is safer to use the Simmons model. Simmons effectively derives the current density vs. voltage calculations for symmetric and asymmetric barriers.

According to the Simmons model the current density, J , due to a net flow of electrons tunneling through a barrier is given by,

$$J = J_0 \left\{ \bar{\phi} e^{-A\sqrt{\bar{\phi}}} - (\bar{\phi} + eV) e^{-A\sqrt{\bar{\phi} + eV}} \right\} \quad (10)$$

$$A = \frac{4\pi\beta s}{h} \sqrt{2m} \quad (11)$$

$$J_0 = \frac{e}{2\pi h (\beta s)^2} \quad (12)$$

$$\beta = 1 - \left\{ \frac{1}{8\bar{\phi}^2 \Delta\phi} \right\} \int_{\phi_1}^{\phi_2} [\phi(x) - \bar{\phi}]^2 dx \quad (13)$$

where $\bar{\phi}$ the mean barrier height, h is Planck's constant, ϕ_1 , ϕ_2 are the work functions of metal 1 and 2, $\Delta\phi$ is the difference in work function, $\phi(x)$ is the barrier height function, β is the correction factor [92] and s is the dielectric thickness.

From the above equations, one could logically conclude, that the larger the difference in work functions of the electrodes, the larger the asymmetry. Work function is also known to affect nonlinearity of the device output [15]. Apart from the work functions, barrier height is also a deterministic factor of the tunneling current. More investigations would be made to determine the barrier height and its dependencies. Another crucial feature of the MIM for increased tunneling current is the contact area of the top electrode. Since the resistance is inversely proportional to the area according to the equation $R = \frac{\rho l}{A}$, larger areas are found to give higher current. Unfortunately, since

the capacitance is directly proportional to the area $C = \frac{\epsilon\epsilon A}{d}$ the operating frequency of the device goes down as area increases since $f = \frac{1}{2\pi RC}$. We can circumvent this problem by using a material with a lower dielectric constant.

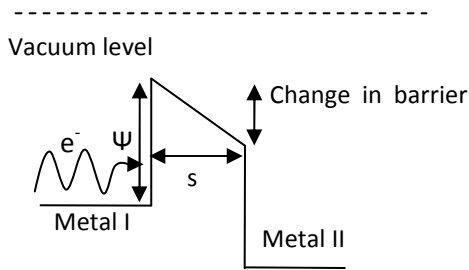


Figure 7. Energy band diagram of an MIM device with different electrodes

Fig. 2 depicted the band diagram of a MIM junction where both the metal electrodes are of the same material. If there is a difference in work function between the two metals or if bias is applied between the two metals, band bending would take place giving rise to a trapezoidal barrier. This will cause substrate electrons to tunnel into the conduction band of the insulator, where they ballistically travel across the metal's Fermi levels to the vacuum interface as illustrated by Fig. 7.

It has been theorized by Simmons et al [92] that if the rectangular barrier is replaced by a trapezoidal one, the tunneling will take place more easily and it would be possible for zero bias current to flow through the device. Since the work functions of various metals are different, the introduction of dissimilar metals as the electrodes creates an asymmetric potential barrier [92]. If the applied bias and/or work function difference between the two metals is large enough such that band bending results in a triangular

shape, the tunneling current density would increase. As a result an intrinsic field F_i exists

and is given by $F_i = \frac{\phi_1 - \phi_2}{es}$ where Φ_1 and Φ_2 are the 2 work functions, e is the charge of electron and s is the barrier thickness in angstroms. Thus if Φ_1 is the barrier height at Metal I, and Φ_2 is the barrier height at metal II, the change in barrier height $\Delta\Phi$ can be given as $\phi = \phi_1 - \phi_2$

3.5 Other Models

There are many factors influencing the tunneling of electrons across the barrier, such as, thermal assisted tunneling, phonon assisted tunneling, photo assisted tunneling, trap assisted tunneling, field assisted tunneling or Fowler-Nordheim (FN) tunneling, hopping assisted tunneling [94], chaos assisted tunneling and so on. Although the main causes of tunneling are photo assisted, thermal assisted and field assisted [11, 94] are depicted in Fig. 8.

The thermal effects on the MIM, mainly from absorption of radiation, can cause the electrons to be thermally excited above the potential barrier height and play a significant role in the detector response. In the case of Fumeaux et al [59], IR radiation absorbed by the SiO₂ layer heats the diode contributing to thermal assisted tunneling. Thermal assisted tunneling and phonon assisted tunneling go hand in hand whereby impinging photons couple with phonons within the material to increase the metal's temperature [11]. According to the Fermi-Dirac distribution, the electrons would gain $k\Delta T$ of additional energy, where k is the Boltzmann constant, thus increasing the tunneling current. One must note that this effect is inherently slow because it is limited by the thermal time constant of the junction and is not directly related to the junction area. A

byproduct of phonon assisted tunneling is the “spreading resistance” [30] where electrons are inelastically scattered by phonons in the bulk material. Evidence was shown by Wilke et al that the spreading resistance also contributes to the nonlinear operation of the diodes thus contributing also to its tunneling mechanisms. Photo assisted tunneling, which is an inherently fast phenomenon, depends linearly on the junction area. Electrons in the metal electrodes absorb photons and become excited by the energy $\hbar\nu$ thus grossly increasing their probability to surmount the barrier. Electrons which have not been excited by photons also manage to pass through the barrier producing dark current; however, the highest quantum yield reported did not exceed 0.1. Therefore, this type of assisted tunneling produces a current much smaller than the other two types of assisted tunneling [11].

In conjunction with these tunneling mechanisms, trap assisted tunneling, Poole-Frenkel emission of electrons and Schottky emission of electrons also take place mostly due to the above mentioned tunneling mechanisms. Trap assisted tunneling (TAT), as the name suggests, takes place when electrons from the electrode occupy unoccupied defects within the dielectric and tunnel from one trap to another till they reach the vacuum interface of the second electrode. When an electric field is applied, Poole-Frenkel emission takes place whereby the conduction band of the dielectric is lowered and electrons trapped within the defect levels of the dielectric move to the conduction band. Schottky emission takes place when the conduction band of the dielectric is lowered in the presence of an electric field and thermal effects cause electrons to move from the Fermi level of the electrode directly to the conduction band of the dielectric [95]. It can be noted that the latter three tunneling mechanisms are subsets of the previously

mentioned tunneling mechanisms. The Poole-Frenkel emissions and TAT rely on thermal effects and are accompanied by thermal assisted tunneling. The Schottky emission typically occurs in conjunction with FN tunneling and is affected by thermal effects.

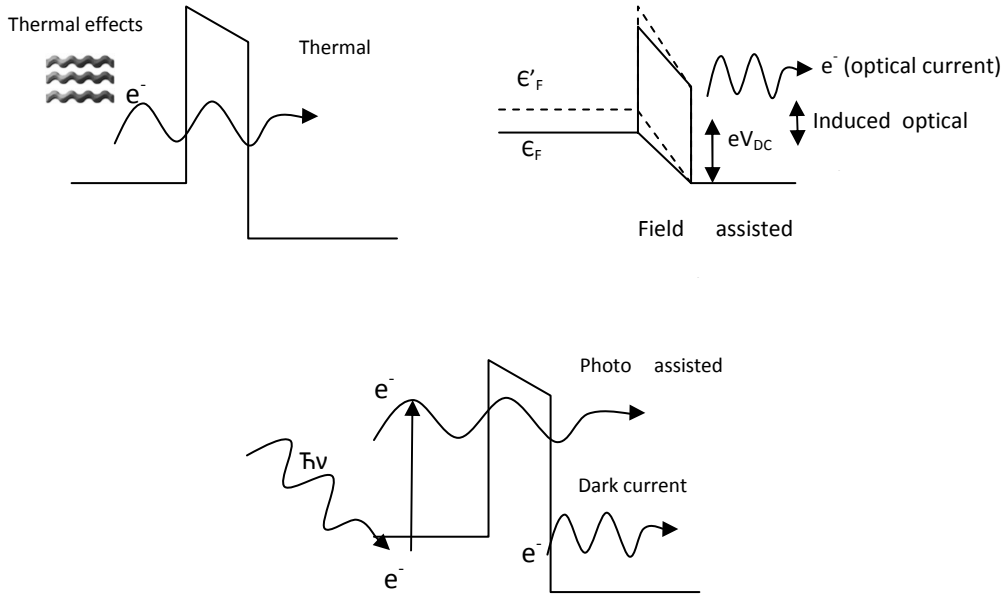


Figure 8. Illustration of different types of tunneling

At this point we can conclude that the tunneling current in a MIM tunnel junction is dependent on many factors and any model that is constructed to predict its electrical behavior must take these factors into consideration. Ramprasad [95] determined the current densities for each of the three mechanisms as shown below. The time dependent current density for trap assisted tunneling is,

$$J_{TAT}(t) = q \int_{x=0}^{\infty} \int_{E=-\infty}^{-qFx} N^{ff}(x, E + qFx) (f_{\infty} - f_0) \left[\frac{e^{-t/\tau} x}{\tau L} \right] dE dx \quad (11)$$

Where q is the charge, x is the spatial location away from the electrode into the dielectric E is the energy level of the trap measures down from the conduction band edge of the

dielectric, F is the electric field, N^{ff} is the field free distribution functions given as $N(x, E) = N^{\text{ff}}(x, E + QFx)$; f_0, f_∞ - are lower and upper Fermi levels respectively, τ is the tunneling relaxation time, and L is the thickness of the dielectric.

The analytical equation for fitting to a TAT model is given as [96]

$$J_{TAT} = Ae^{\left[\frac{-8\pi\sqrt{2qm}\phi^{3/2}}{3hV}\right]} \quad (12)$$

The Poole-Frenkel emission current density is given as,

$$J_{PF} = q\mu F \int_{x=0}^{\infty} \int_{E=-\infty}^{-qFx} f_{PF} n(x, E, t) dE dx \quad (13)$$

Where

μ is the electronic mobility in the dielectric, ϵ is the permittivity of the dielectric

PFF – the Pole-Frenkel factor=

$$\exp\left\{-\frac{q}{kT}\left(-E - \sqrt{\frac{qF}{\pi\epsilon}}\right)\right\} \quad (14)$$

The Schottky emission total current density is given by

$$J_s = \frac{qmk^2}{2\pi h^3} T^2 = \exp\left\{-\frac{q}{kT}\left(-\Phi_s - \sqrt{\frac{qF}{4\pi\epsilon}}\right)\right\} \quad (15)$$

Where, Φ_s is the offset between the conduction band minimum of the dielectric and the Fermi level of the electrode. Ramprasad [95] states that the leakage current measured at short times is mostly due to TAT. When the applied bias is maintained for longer periods

of time, the Poole-Frenkel or Schottky tunneling mechanisms take over. He also observed that the Poole-Frenkel current increased as TAT decreased which leads us to infer that there are fewer electrons making it to the Fermi level of the second electrode and, instead, they are exiting through the conduction band of the dielectric. The dependence of the TAT current on temperature was found to be weaker than that of the other two mechanisms. He theorized that the temperature affects the TAT only through the distortion of the Fermi levels, which is a weak effect. It would seem that tunneling between traps would greatly benefit from thermal effects although a drastic increase in temperature might cause lattice vibrations shifting the traps thereby impeding the tunneling of trapped electrons. Also intermediate annealing might take place reducing the number of traps and thus reducing the TAT. This theory seems plausible as Ramprasad further confirms that Schottky tunneling is more pronounced with increases in temperature than the other mechanisms, especially since Schottky tunneling does not depend on the defects of the dielectric. According to Hu et al [97], direct tunneling is associated with electrons traversing a trapezoidal barrier and FN tunneling occurs when electrons traverse a triangular barrier. The total current density is given as,

$$J_{eq} = J_{FN} \times J_{trapezoid} \quad (16)$$

$$J_{eq} = (AE_{ox}^2) \left(\frac{\Phi_b}{V_{ox}} \right) \left(\left(\frac{2\Phi_b}{V_{ox}} \right) - 1 \right) e^{-\frac{B \left(1 - \left(1 - \frac{V_{ox}}{\Phi_b} \right)^2 \right)^{\frac{3}{2}}}{E_{ox}}} \quad (17)$$

Where $B = 8\pi\sqrt{2m_{ox}}\Phi_b^{\frac{3}{2}}$, m_{ox} is the oxide effective mass and E_{ox} is the oxide field.

Fig. 9 depicts the output current as a function of applied bias for oxide films with thicknesses between 2.2nm to 9.7nm. Pure direct tunneling without FN tunneling takes place when the oxide thickness is below 2.2nm [98]. Hu's paper also states that according to the above model as the barrier height is changed from triangular to trapezoidal, the leakage current increases. This is in contradiction to the Simmon's model which states the opposite. Logically the Simmons model seems to make sense since the probability of an electron to tunnel through a triangular barrier where the electronic thickness is lesser than that of a trapezoidal barrier is higher.

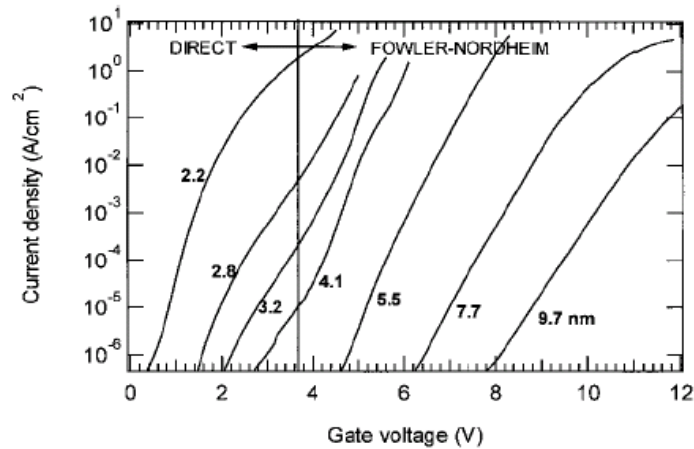


Figure 9. Output current of a tunnel junction w.r.t film thickness [98]

3.6 Resonant Tunnel Model For Multilayered Tunnel Junctions

The resonant tunneling mechanism that takes place in a multi layered device can be modeled using the transfer matrix method [99]. Eliasson and Grover et al have shown how tunneling probability increases at certain bias energies that correspond with the barrier energies of the quantum well or trap states in eqn (18) [31, 33]. The electron tunneling probability as a function of energy is simulated and plotted in Fig. 10. The band

diagram is superimposed on the simulation to show the increased tunneling at various states. The voltage drop across each layer is given as

$$\Delta V_j = (V_{bias} - V_{bi}) \frac{x_j / \epsilon_j}{\sum x_j / \epsilon_j} \quad (18)$$

$$V_{bi} = \Delta\phi$$

V_{bi} is the built in potential given as

Where x_j and ϵ_j are the thickness and dielectric constant of the j th layer respectively [33]

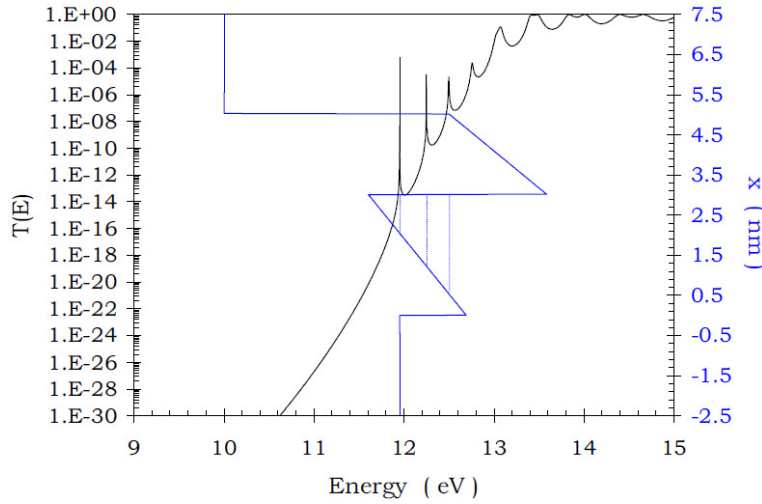


Figure 10. Electron tunneling probability in a bi-layered tunnel junction as a function of energy [31]

The tunneling models fitted to the results in this research are the TAT model using eqn (12) and the FN model which is given by eqn (17)

$$J = CV^2 \exp(-B/V) A / cm^{-2} \quad (19)$$

Where V is the field at the Metal-Insulator interface. B and C are defined by

$$B = 6.83 \times 10^7 \left(\frac{m_{ox}}{m} \right)^{1/2} (\phi^{3/2}) \quad \text{and} \quad C = 1.541 \times 10^{-6} (1/\phi),$$

Where ϕ is the barrier height and m_{ox} is the effective mass of electrons in the insulator.

The measured data was fitted to the model [96]

$$\text{Log}(J / V^2) \approx -\phi / V \quad (20)$$

Based on the fits of eqns (12) and (20), a suitable band energy diagram is illustrated for the NiO device, the ZnO device and the bilayer device as will be discussed in chapter six.

CHAPTER 4: DEVELOPMENT OF MIM TUNNEL JUNCTIONS

One of the first MIM devices were the point contact which consisted of a thin metallic wire with a fine etched tip in weak contact with an oxidized metallic surface, as shown in Fig. 11. These diodes were called “whisker diodes” [59]. The whisker, mostly tungsten, has a tip radius of less than 50nm and a contact area of about $0.01\mu\text{m}^2$. The whisker acts like an antenna and thus was used as a diode coupled antenna. But the point-contact configuration of this device has a significant disadvantage, the devices do not operate in the infrared or visible regions and they have very low mechanical stability apart from being highly unreliable. Moreover the sensitivity and response times are strongly dependent on the contact area which is a difficult parameter to control due to its structure [59], hence leading to the development of thin film MIMs. It has been mentioned that the asymmetry of the tunnel junction determines the output of the device and depends on the electrode materials [100].

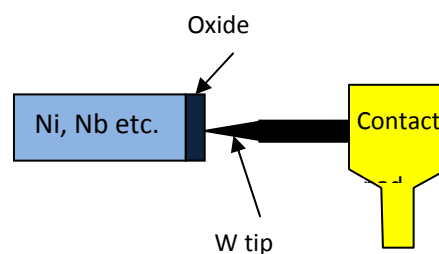


Figure 11. Illustration of whisker diode

4.1 Processing Techniques

With the advent of efficient optical lithography and advanced deposition systems, the active area of the diodes and thickness of a thin film could be highly controlled although its thickness was much larger than that of the point-contact diodes. By utilizing deposition processes such as thermal evaporation, sputtering (PVD), chemical vapor deposition (CVD), atomic layer deposition (ALD) and molecular beam epitaxy (MBE), the uniformity of the dielectric could be controlled to a high degree, unlike the point contact devices which are affected by atmospheric contamination [98] or the highly unpredictable surface area of the tip. Various methods have been investigated to achieve very thin films. Fisher et al [101] suggest that insulating layers thicker than a few tens of angstroms are nearly impenetrable by electrons and their tunneling probability falls off exponentially with an increase in thickness. He concludes that at very small voltages the resistance is ohmic whereas at larger voltages the current increases exponentially with voltage. It is contingent to acquire very thin films if one wants to facilitate tunneling through it and thus achieve a high tunneling current although determining whether the tunneling current is high or low depends on the operational purpose of the device. In the 1960 article, Fisher et al tried three different ways of producing the layer: oxidizing the insulating layer in air, oxygen atmospheres and distilled water. With current technologies, depending on the material, different deposition methods can be considered efficient. If the material is one that readily oxidizes, the PVD or CVD methods can be employed after which a passivation process is immediately applied. If the material is one that does not readily oxidize in an ambient atmosphere, an oxidation layer can be formed either in air or in a pure oxygen atmosphere. The prior method though controllable, cannot achieve

very thin thicknesses, and the latter though uncontrollable, can achieve thicknesses of a few angstroms. The active area and the thickness of the dielectric can be considered as the critical dimensions for an MIM diode. The active or contact area of the layer determines the current density and also the parasitic capacitance which would be inherent within the device and the thickness of the dielectric layer determines the number of electrons that can tunnel through. Many designs can be used to attain the sandwich structure. A simple planar structure, a stepped structure (shown in Fig. 1) [8] and a cross hair [17] shown in Fig. 12 below are all effective structures that can be used to construct an MIM junction. Wang et al [102] fabricated Ta-Ta₂O₅-Ta based MIM structures whose thicknesses ranged from 1nm to 4nm. It was found that as the area of the top electrode increases, the breakdown field strength decreased considerably mainly due to the fact that the larger area increases the roughness and the probability to contain more impurities.

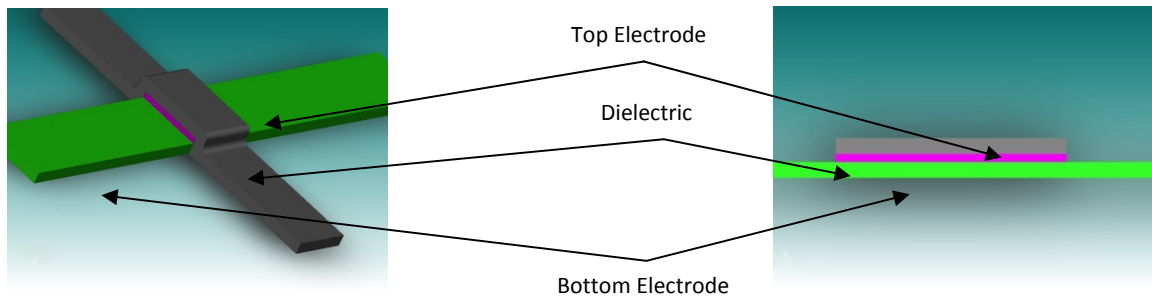


Figure 12. Crosshair type design of the tunnel junction

Although there was some asymmetry observed, the current was very low since the dielectric constant of Ta₂O₅ is about 25. This makes it a good capacitor rather than a diode. Many groups have tried creating very thin barriers, and very small areas [11, 103]. Heiblum et al and Havemann proposed and fabricated a totally new type of configuration

of the MIM structure viz. a vertical one. The area would now be the thickness of the metal layer with a very thin layer of oxide atop it.

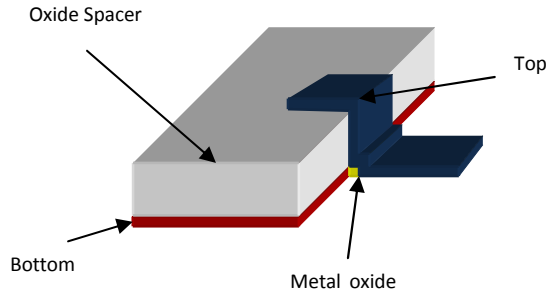


Figure 13. Edge diode structure

Areas as small as tens of nanometers, and thicknesses as small as a few angstroms, can be achieved in this configuration. Havemann's group fabricated an Al-Al₂O₃-Al, Ni-NiO-Ni, Pb-PbO₂-Pb and Ni-NiO-Au structures as shown in Fig. 13, the top and bottom electrode was about 100 to 300nm thick.

A thick spacer oxide was deposited on top of the bottom electrode prior to sputter depositing the oxide layer. Though this configuration shows great promise, there are a number of issues regarding its proper characterization and workings, the main issue being the formation of the edge. It is very difficult to control the geometry of a structure as we approach the nanometer and angstrom realms. What one would expect to be a straight edge would invariably end up being something different as shown for the possible edge geometries that could end up being fabricated, Fig. 14. One could end up with a slanted edge when employing wet etching techniques, or a jagged edge due to scalloping if dry etching techniques, such as metal RIE and DRIE, were to be employed. Even if it was possible to obtain a vertical straight wall, upon the deposition of the metal oxide,

especially physical vapor deposition, it would invariably end up as a curved edge [104]. If lift off is applied, the sidewall would tear at the edge tips leaving fin like structures which could pierce the films laid thereafter or cause non-uniformities in the stack [105, 106]. As a result the control of the area through geometry is very difficult giving rise to nonrepeatable device results. The DC measurements done so far on MIM diodes, be it planar or vertical, are mostly in the nano or pico ampere range. Those in the mA range do not show much of non-linearity or asymmetry and thus cannot be used as a diode for rectification purposes. It is for this reason that typically dissimilar electrode metals are used.

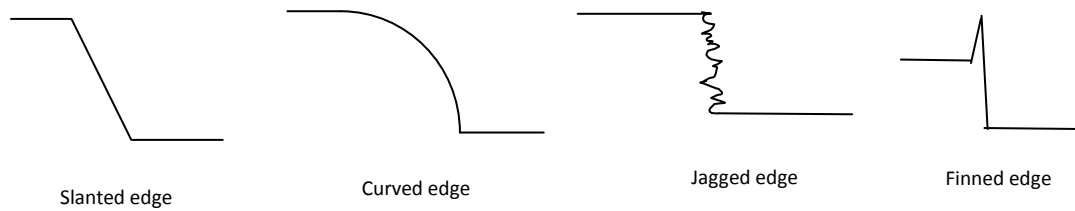


Figure 14. Illustrations of various artifacts edges created on the edges during fabrication of an MIM diode

The introduction of dissimilar metal electrodes was investigated with the hope that larger asymmetry would be observed. Asymmetry of the MIM tunnel junction is determined by the difference in work function of the top and bottom electrodes. As mentioned in a previous section, Fig. 16 shows the band diagram of an MIM tunnel junction using two dissimilar metals, at zero bias the difference in barrier height being $\Delta\phi$. Fig. 17 shows the same band diagram with an applied bias voltage V_{Bias} . As can be seen, even at zero bias there is a higher probability of electron tunneling than that of the same metal MIM junction. The application of a very small bias voltage increases the flow of electrons through the barrier. If one could achieve the same amount of current flow

with the rectangular barrier configuration, the bias voltage needed would be much higher. Wilke et al [30] surmised that Nickel Oxide (NiO) thin films used as the potential barrier give the best tunneling results when used in the infrared region although the exact reasons were not stated [107].

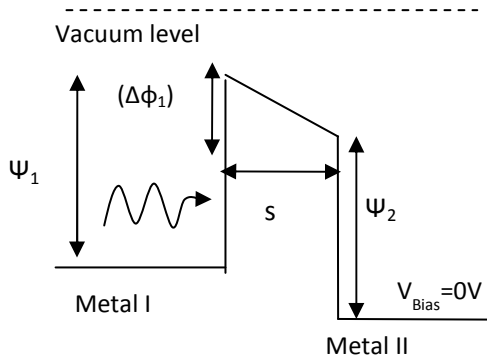


Figure 15. Energy band diagram of an MIM tunnel junction using two dissimilar metals

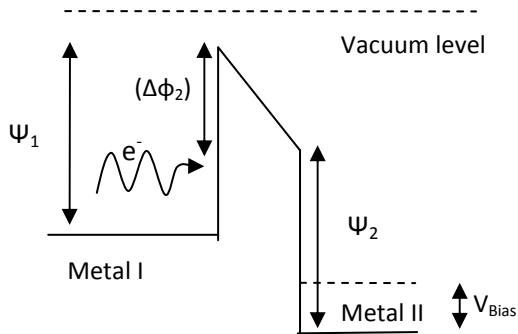


Figure 16. Energy band diagram of an MIM tunnel junction using two dissimilar metals at applied voltage V_{bias}

A very early dissimilar electrode diode which was fabricated Gupta et al in 1976 [107] used barium stearate as the dielectric and was deposited using the Langmuir-Blodgett deposition technique. But the current output of the device's I-V response was in the range of nA, and hence too low to be put to appreciable use.

One might wrongly assume that merely changing the electrode materials so as to introduce a large work function difference would result in a large current density at zero bias voltage, but this is not the case as there are many factors involved when using different electrode materials. If a readily oxidizing metal and its oxide are chosen, it must ideally be placed as the bottom electrode since its oxidation can be easily controlled prior to deposition of the top electrode. The challenges to using a readily oxidizing metal as the bottom electrode with a different metal oxide as the insulating layer, lies in its fabrication. If one was to use lithographic processes, after laying down the metal it would be very difficult to pattern its surface due to continual ambient oxidation. In such cases it would be in one's best interests to pattern the device accordingly so as to fabricate the bottom electrode and the insulating layer in the same deposition environment. If a readily oxidizing metal is to be used as a top electrode it would be advisable to deposit a passivation layer atop the metal so as to prevent non uniform charge density due to depletion of the oxidized metal. Also the conductivity of the metals used as electrodes should preferably be large and the resistivity should preferably be negligible so as to not contribute to the characteristic impedance of the device when used in high frequency applications. Table 2 illustrates a table of metals that could be used as electrodes for the tunnel junctions studied in this work. The table was arranged with increasing work function and the electrode combinations with the highest $\Delta\Phi$ are highlighted in yellow. Nickel Oxide was chosen as the insulating material for the devices presented in this work because of very low resistivity and superior electrical stability [8], which will be discussed in the following section. The Ni-Cr combination was chosen for this work due to the feasibility of the material targets and availability of fabrication equipment.

Table 2 Table of metals with work function difference

		Ba:	Hf:	Nb:	Ta:	Zr:	Al:	Mn:	Ti:	Cr:	Ag:	Mo:	Zn:	Ni:
		2.52	3.9	3.95	4	4.05	4.06	4.1	4.33	4.5	4.52	4.63	4.9	5.35
Ba:	2.52	0	1.38	1.43	1.48	1.53	1.54	1.58	1.81	1.98	2	2.11	2.38	2.83
Hf:	3.9	1.38	0	0.05	0.1	0.15	0.16	0.2	0.43	0.6	0.62	0.73	1	1.45
Nb:	3.95	1.43	0.05	0	0.05	0.1	0.11	0.15	0.38	0.55	0.57	0.68	0.95	1.4
Ta:	4	1.48	0.1	0.05	0	0.05	0.06	0.1	0.33	0.5	0.52	0.63	0.9	1.35
Zr:	4.05	1.53	0.15	0.1	0.05	0	0.01	0.05	0.28	0.45	0.47	0.58	0.85	1.3
Al:	4.06	1.54	0.16	0.11	0.06	0.01	0	0.04	0.27	0.44	0.46	0.57	0.84	1.29
Mn:	4.1	1.58	0.2	0.15	0.1	0.05	0.04	0	0.23	0.4	0.42	0.53	0.8	1.25
Ti:	4.33	1.81	0.43	0.38	0.33	0.28	0.27	0.23	0	0.17	0.19	0.3	0.57	1.02
Cr:	4.5	1.98	0.6	0.55	0.5	0.45	0.44	0.4	0.17	0	0.02	0.13	0.4	0.85
Ag:	4.52	2	0.62	0.57	0.52	0.47	0.46	0.42	0.19	0.02	0	0.11	0.38	0.83
Mo:	4.63	2.11	0.73	0.68	0.63	0.58	0.57	0.53	0.3	0.13	0.11	0	0.27	0.72
Zn:	4.9	2.38	1	0.95	0.9	0.85	0.84	0.8	0.57	0.4	0.38	0.27	0	0.45
Ni:	5.35	2.83	1.45	1.4	1.35	1.3	1.29	1.25	1.02	0.85	0.83	0.72	0.45	0

Al and Ni were also used as top electrodes to compare the asymmetry shown in Fig. 42 in chapter six. It is interesting to note that although the $\Delta\Phi$ of Ni and Al is almost 1.3eV, no clear asymmetry could be discerned. The experiment only proved that the Ni/NiO/Cr configuration was more stable over a range of measured devices. The bottom electrode (Ni) and the insulator layers were deposited using sputtering and reactive sputtering, respectively. Sputtering was performed when Al and Ni were used as the top electrode, sputtering was performed. When Cr was being used as the top electrode; thermal evaporation was performed followed by thermal evaporation of Au as a capping layer. The RC time constant of the tunnel junction is a limiting factor which affects its performance at very high frequencies. For the RC time constant to be small, the capacitance should be very small in which case either the area or dielectric constant should be very small. The dielectric constant of NiO is 11.9 and its reduction would not make any significant difference. The area however is in the order of microns and

reducing the length by an order of magnitude would reduce the capacitance by its square. For a rectifying device that operates at frequencies of 500GHz and below, the active area of the diode would have to be less than $1\mu\text{m}$. Since such a small area could not be achieved in this research, the smallest area fabricated was $3\mu\text{m} \times 3\mu\text{m}$. The operating frequency for such a device is 51.2GHz. The following section discusses the tailoring of the insulating layers for both NiO and ZnO leading to the optimal choice for its integration in the tunnel junctions described in this work.

4.2 Optimization of the Dielectric Layer

The primary goal of this research is to conceptually identify the intrinsic operation of Nickel Oxide thin films as a tunnel dielectric. The efficiency of a tunnel junction is almost as good as its dielectric layer. The effects of fabrication (pre and post) are leading factors to the modification of the dielectric layer. As mentioned earlier the electrodes play a major role in increasing the density of tunneling electrons, but the oxide is crucial to the probability of those electrons tunneling to the other electrode. The thickness of the film which corresponds to the barrier width determines whether the electron will hop, tunnel or resonate within the barrier. If the barrier width is larger than 10\AA , electrons tend to hop rather than tunnel [87]. Depending on the barrier height it is possible that a combination of electron tunneling and hopping takes place. The crystallinity of the barrier is also important as better conduction of electrons would take place in highly crystalline films. Unless the insulating layer is an epitaxial film, it would almost always contain impurities [87]. These impurities serve as traps for electrons and hence they are also called electron traps. The space charge due to trapped electrons may seriously affect the tunneling I-V

response. If the phase of the metal oxide is not properly established, O₂ vacancies present would distort the cation lattice and serve as excellent electron traps.

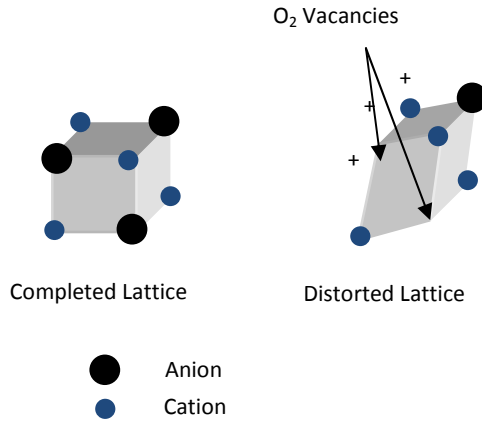


Figure 17. Illustration of completed and distorted lattices

This increases the space charge which in turn increases the barrier width thus limiting tunneling. Upon the application of an external voltage, further distortion or lattice reconstruction may take place thereby trapping or releasing more electrons. Fig. 17 shows the difference between a completed lattice and one with O₂ deficiencies. Such deficiencies also affect the zero bias resistance and the intrinsic impedance of the diode. Lunkenheimer et al [94] verified the frequency and temperature dependence of the electrical conductivity of NiO thin films using a model called the Correlated Barrier Hopping (CBH) model. The model proposes that electron pairs hop over potential barriers between defect sites where the heights of the barriers are correlated with the intersite separation. The films deposited by the reactive evaporation of Nickel Oxide, were around 610 nm and thick enough to contain multiple defects. Nickel Oxide films have very low resistivities of the order of 10^{-4} Ωcm [108] and therefore it was probably advantageous to deposit a thicker film. From the measurements, Lunkenheimer

demonstrated that at low frequencies the conductivity of NiO was ohmic, but at higher frequencies, it exhibited AC conductance. This could have a serious impact on the use of NiO thin films in IR detectors, since it suggests that at THz frequencies the device would not rectify as effectively.

Improper phase formation of the insulating layer is also detrimental to the MIM when used as a diode. The presence of grain boundaries would conduct electrons directly thus acting as a mere resistor instead of a diode. Epitaxial films would not have this problem as the lattice sites would be completed, thus eliminating such impurities or traps, and segregation of grain boundaries would be minimal if not altogether absent. One method to reduce oxygen deficiencies would be to anneal the film in an O₂ atmosphere, but this might lead to other problems, as discussed in the next chapter.

Although the presence of impurities does seem undesirable for the working of an MIM tunnel junction, a positive outcome can be obtained if properly designed. Impurities present in the insulating layer form impurity states in the forbidden energy gap. When localized electronic wave functions of two impurity states overlap, an electron bound to the first impurity state can tunnel to an unoccupied second impurity state without involving activation to the conduction band [109]. The mobility of an electron between impurity states is very low and usually occurs at very low temperatures due to the presence of widely spaced impurities at those temperatures. Gadzuk [109] reported that resonance tunneling may take place through impurity states. He states that impurity states open up new tunneling channels with a concomitant slope of the I-V characteristics. But depending on the impurity concentrations, the change may not rise above noise levels. Since the number of impurity sites and the number of electrons control the probability of

impurity tunneling, careful doping and introduction of impurity sites while fabricating can facilitate electron tunneling in the insulator layer.

Nickel oxide is a sought after material for its use as an antiferromagnetic, transparent conductance, chemical and electrical stability, among many others. It is known to be a Mott oxide exhibiting p-type electrical behavior. Its bulk crystal type is that of a cubic rock salt structure with a lattice parameter of 0.4195 [108, 110-114]. The p-type characteristic of NiO is because of Nickel deficiencies during the deposition of its thin film. The large oxygen atoms in the structure prevent Ni atoms from occupying the interstitial sites resulting in vacancies in the normally occupied Ni sites. In a natural attempt to preserve the electrical neutrality of the crystal, two Ni²⁺ ions are converted to Ni³⁺ for every vacant Ni site. These Ni³⁺ ions are effectively positive holes that move from one vacancy to another [110]. The NiO used as an insulating layer in the fabrication of MIM tunnel junctions, described in this research, was deposited at various oxygen concentrations. The relation of the oxygen concentration and the electrical characteristics of the devices were considered important in the selection of the best stoichiometry for the insulator. The fabrication of the devices is described in detail in the Appendices; in this section the deposition of the Nickel oxide layers with different oxygen concentrations will be presented.

A 3" Ni target was used as the sputtering source since reactive sputtering was being used to deposit the films. Reactive sputtering is the process where a target is bombarded by ions in the presence of a reactive gas to form a chemical reaction with the sputtered atoms and gas resulting in the desired compound. The compound atoms diffuse around on the substrate and its adhesion is determined by the binding energy to the

substrate. Therefore it is paramount to have a very clean substrate and to deposit at ultra-high vacuum conditions (of the order of $1\mu\text{Torr} - 0.1\mu\text{Torr}$). The chemical reaction may take place at the cathode, en route to the substrate, or a combination of the two possibilities. A brief schematic is shown in Fig. 18.

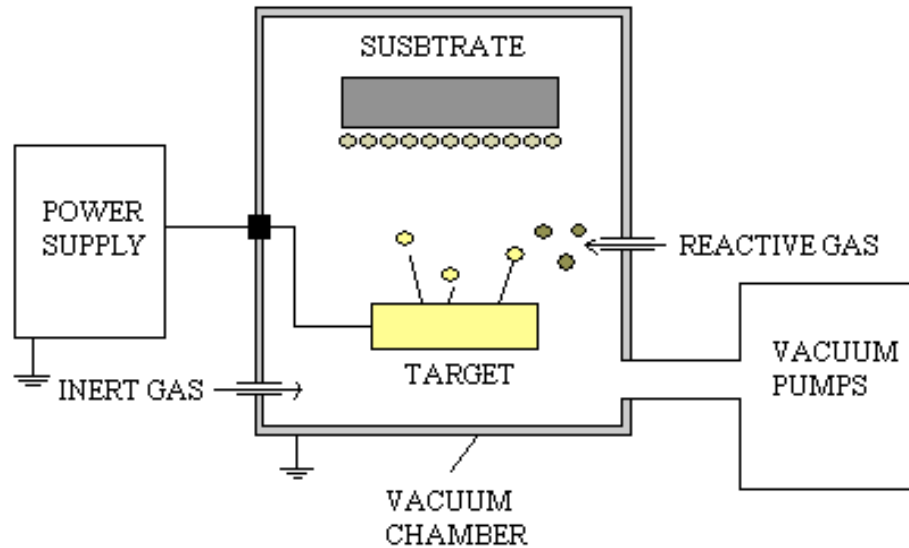


Figure 18. Schematic of a reactive sputtering process. Reprinted with permission [8]

After the chamber has reached a base pressure of a few μTorr , Ar gas is introduced and the pressure is stabilized to 10mTorr . Subsequently O_2 gas is introduced and the chamber pressure is adjusted to re-stabilize it back to 10mTorr . The Ar atoms initiate plasma that strikes the Ni target and releases Ni atoms. O_2 atoms which are in the chamber also get ionized either through physical bombardment or through electrical ionization and react with the Ni atoms to form non stoichiometric NiO. The concentration of the oxygen is controlled by controlling the partial pressure of the O_2 in the chamber during deposition. This is done by controlling the flow ratio of the Oxygen gas to Argon gas using a Mass

Flow Controller (MFC) that operates in Standard Cubic Centimeters per Minute (SCCM). If the ratio of the flows is 5sccm Oxygen to 10sccm Argon, the ratio is 1:2 which results in 33% of oxygen in the chamber compared to Argon. This does not mean that there are 33% of Oxygen atoms present in a unit cell of the NiO crystal lattice, this information can be discerned by quantitative analyses such as X-Ray Photoluminescence, Spectroscopy (XPS) or Energy Dispersive X-Ray Spectroscopy (EDS) and similar techniques.

NiO thin films were deposited on (100) p-type Si substrates by DC magnetron reactive sputtering with a Nickel target in the presence of Ar and O₂. The base pressure was kept at 0.9 μ Torr to avoid any contamination, and the working pressure was 10 mTorr. The ratios of the flow rate of O₂ to Ar for 20%, 33%, 40%, 60%, 80% and 100% were 5sccm:20sccm, 5sccm:10sccm, 4sccm:6sccm, 6sccm:4sccm, 8sccm:2sccm and 10sccm respectively.

X-Ray Reflectography (XRR) measurements were performed using a Phillips X-Pert X-Ray diffraction system and analyses were done by PANalytical X'Pert Reflectivity™ program on some of the films to determine their thickness. Since the limit of the XRR measurements is around 7nm (\pm 1nm), thicker films were fabricated and the sputtering rate was determined. The XRR spectra were fitted (red curve) against the measured data (blue curve) using segmented fits to determine the thickness as can be seen for some of the films in Fig. 19, Fig. 20 and Fig. 21. Fig. 22 gives an idea of the change in sputter rate with respect to Oxygen concentration during deposition.

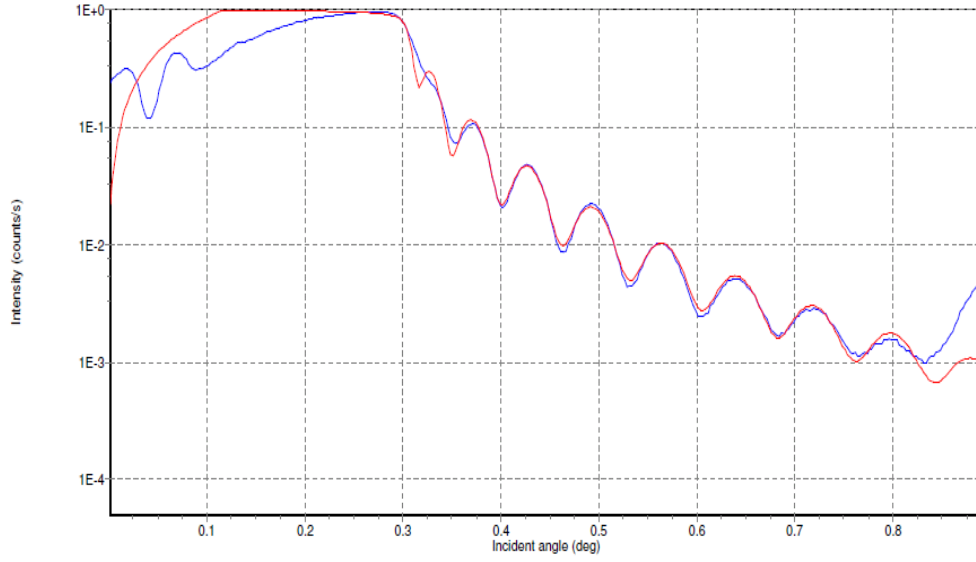


Figure 19. Fitted XRR spectrum of film deposited at 20% O₂ partial pressure for 30mins

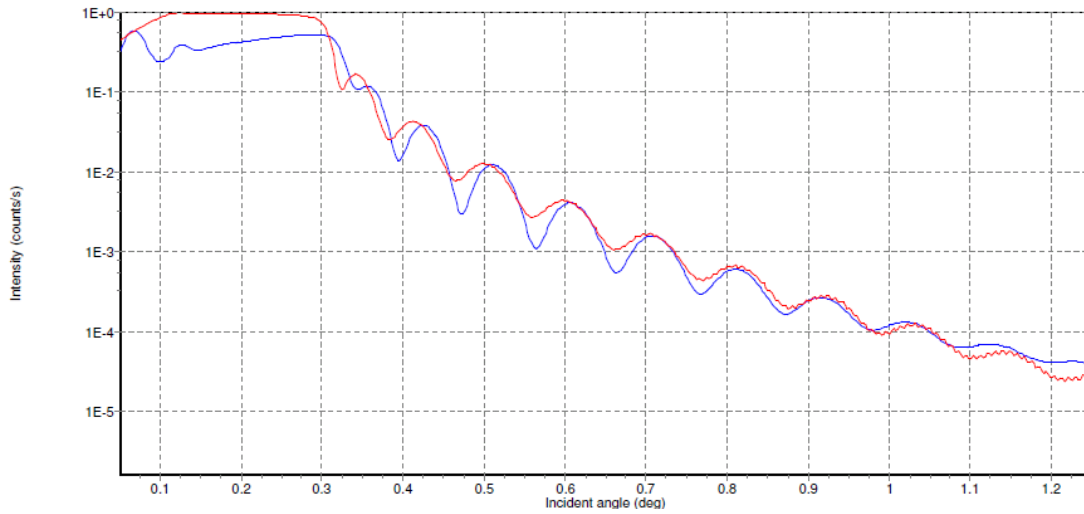


Figure 20. Fitted XRR spectrum of film deposited at 33% O₂ partial pressure for 30mins

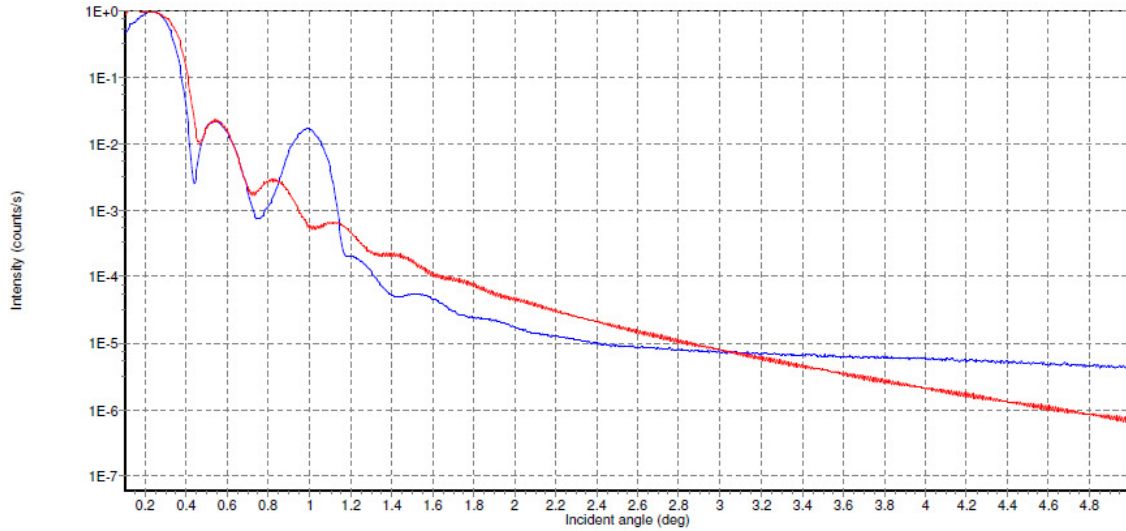


Figure 21. Fitted XRR spectrum of film deposited at 40% O₂ partial pressure for 30mins

As one would identify from the plot, the sputtering rate decreases exponentially although the ionization energy of oxygen is almost 3eV lesser than that of Argon. This could be because, as Oxygen concentration increases in the chamber, the increased reaction that takes place with Nickel atoms and their subsequent ionization causes the mean free path to decrease, thereby leading to a decrease in the sputtering rate.

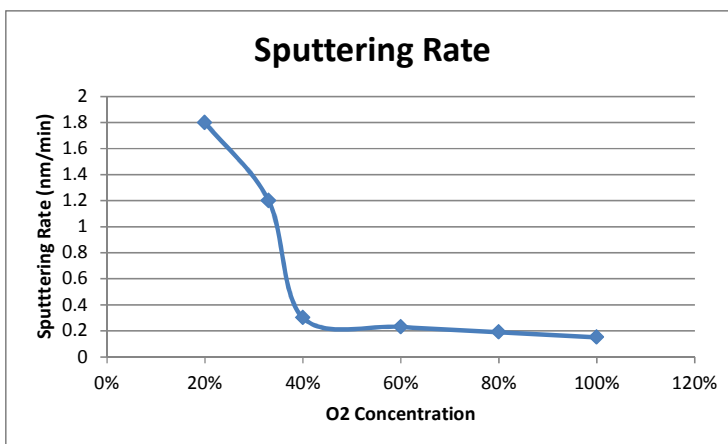


Figure 22. Plot of sputtering rate as a function of Oxygen concentration

The quality of the films was measured using X-Ray Diffraction (XRD) analysis as shown in Fig. 23.

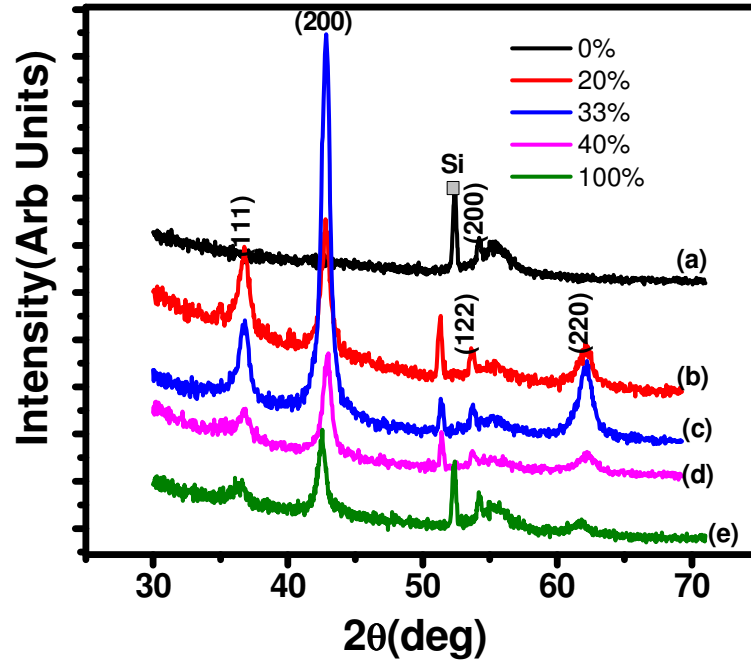


Figure 23. XRD spectra of films deposited with different Oxygen partial pressures. The 0% spectra is a Nickel only film.

From the above Fig. it can be seen that the two characteristic NiO peaks: the (200) and the (220) peaks are very prominent at 33% O₂ concentration even without annealing. This has also been confirmed by Hotovy et al [108, 114]. The roughness of the films was studied by Atomic Force Microscope (AFM) using a Veeco Dimension III system. Fig. 24, Fig. 24 and Table 3 illustrate the roughness of the sputtered NiO films as a function of Oxygen partial pressure during sputtering.

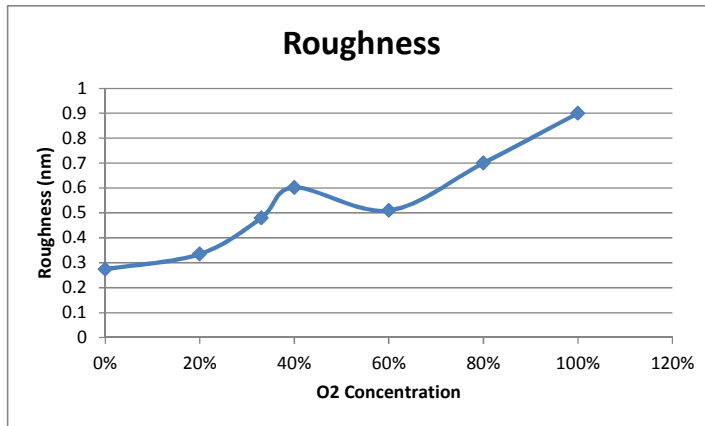


Figure 24. Roughness as a function of O2 concentration during deposition

When the oxygen flow rate is increased, the mean free path decreases leading to very low energies of the atoms arriving at the surface thereby forming an island type growth. At lower flow rates, the mean free path is increased giving sputtered atoms more energy to get deposited on the substrate. However, there is a possibility that oxygen atoms present get ionized and re-sputters the film from the substrate causing it to become rough.

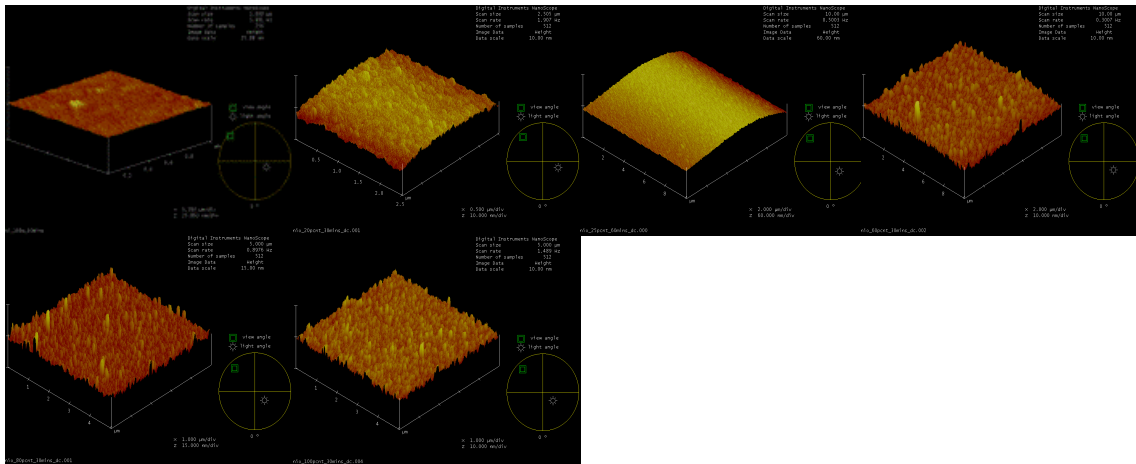


Figure 25. Starting from top left going clockwise, AFM images of NiO films deposited at 0%, 20%, 33%, 40%, 80%, 100%

From the roughness analysis, it can be observed that there is an increase in roughness as the oxygen concentration increases with a large rise from 20% to 40%. Since sputtering below 30% oxygen concentration is typically a metallic mode deposition[114], the next highest oxygen concentration (33%) was deemed suitable in an effort to decrease oxygen vacancies. From the above material characterization, it was clear that a film deposited at 33% oxygen partial pressure yielded better film characteristics. Later electrical measurements on devices consisting of such films also proved to exhibit better responses as will be seen in chapter six [115].

In an effort to produce tunnel junction devices that exhibit a very high degree of non-linearity, the possibility of combining the p-type NiO film and an n-type ZnO film to form a bilayer was explored. The purpose of choosing such a combination was two-fold. One is that the bi-layer junction functions as a resonant tunneling diode at high frequencies. The other is that it can function as a regular P-N junction tunnel diode at low frequencies since NiO is a p-type oxide and ZnO is an n-type oxide. The n type charge carriers in the ZnO layer accumulate at the interface to form a sheet with high conductance. Also polar discontinuities at the interfaces aid in generating or removing charge carriers [116]. Such a bilayer was already investigated by a few groups but mostly for the application as transparent oxide semiconductors. It has also been reported to give very good asymmetry and non-linear characteristics [63, 117-119].

Table 3 Roughness characterization of NiO films deposited at various oxygen concentrations

O2 Concentration	Roughness Å
0%	0.274
20%	0.335
33%	0.48
40%	0.602
60%	0.51
80%	0.7
100%	0.9

Zinc Oxide (ZnO) films were deposited as the second insulator layer by compound reactive sputtering where the target material is not a metal but a compound (in this case it is ZnO) of what one wants to deposit. In this scenario, introducing O₂ gas during the sputtering process is a healing method to aid in eliminating any oxygen vacancies since the sputtered compound would already have Oxygen atoms, but due to ionization may lose some. To keep the processes consistent, the ZnO films were also deposited with 33% oxygen partial pressure. The XRD spectrum of the sputtered ZnO film is shown in Fig. 26. The spectrum shows strong c-axis orientation owing to the increased intensity of the (002) plane. The film is polycrystalline as can be seen by the additional (103) peak crystallinity which is due to nature of thermally un-treated sputter

deposition technique. The XRD spectrum has been confirmed with multiple sources [63, 117-121]. Hall measurements were performed on NiO films and ZnO films individually with thicknesses of around 10nm. The measurements of the NiO layer revealed that it was p-type with a resistivity of 94 Ω and a carrier concentration of 1.832×10^{14} cm⁻³. The ZnO layer yielded a resistivity of 2k Ω and a carrier concentration of 2.32×10^{13} and exhibiting a negative Hall voltage suggesting that it was n-type. This confirms that the NiO and ZnO films deposited in this research conformed to the carrier types mentioned in literature.

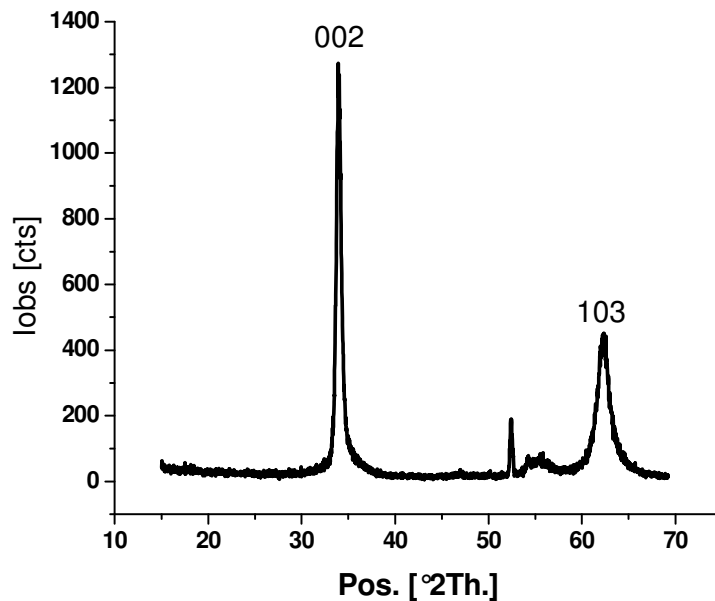


Figure 26. XRD spectrum of ZnO film showing strong c-axis orientation

Reflectance mode UV-Vis measurements were done on the individual films and the bilayer to investigate the presence of energy levels and to determine the bandgap.

Fig. 27 shows the reflectance spectra of the films. The NiO film starts absorbing at around 683nm which renders it a good material for optical electronics from 650nm onwards. The ZnO film absorbs at around 770nm and then sharply reflects at around 480nm allowing it to be used in optical sensors. The bilayer on the other hand shows a very gradual increase in absorption from around 950nm and increases again gradually from 450nm. Compared to the ZnO spectrum, the bilayer spectrum possesses a very broad peak. This indicates that there are many energy levels present in the film supporting the trap assisted tunneling mechanism.

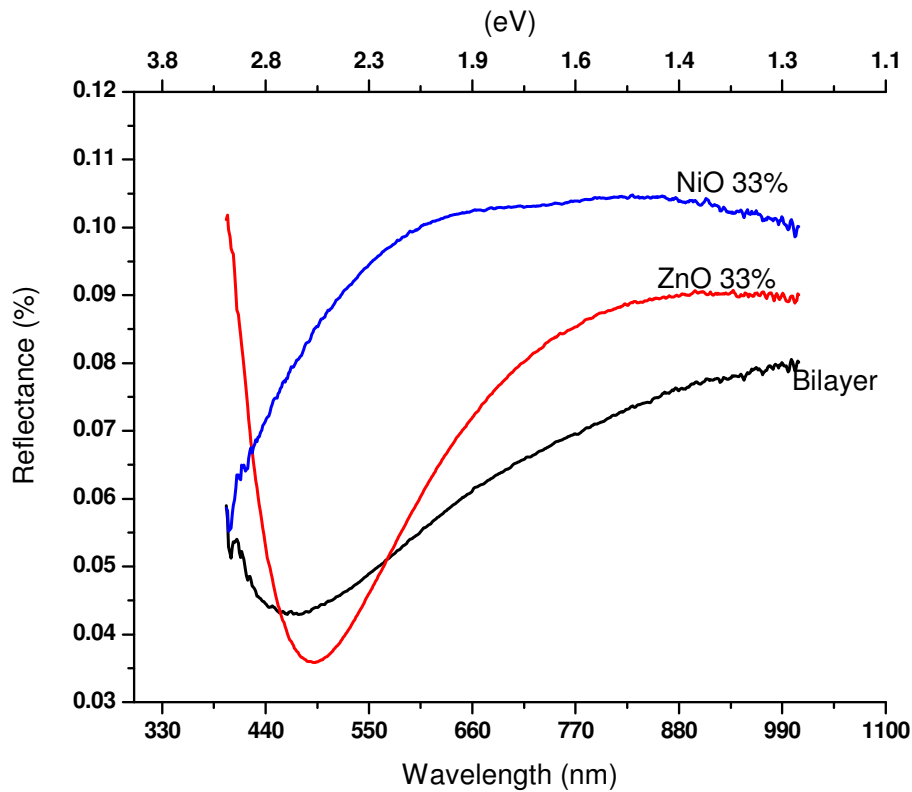


Figure 27. Reflectance mode UV-Vis spectra of NiO film, ZnO film and the bilayer film

The bandgap was calculated by plotting the reflection coefficient k with respect to $h\nu$ and determining the intercept on the x-axis as shown in Fig. 28. The relation between k and ν is given as $(kh\nu)^2 = A(h\nu - E_g)$ Where A is a constant [122-124] and k is given by $\ln\left(\frac{R_{\max} - R_{\min}}{R - R_{\min}}\right)$.

The theoretical and experimental values of NiO and ZnO thin films have been reported as 3.54eV and 3.4eV respectively [63, 117, 118, 125], and the calculated band gap values of the films deposited in this work is found to be 3.04eV and 2.4eV respectively.

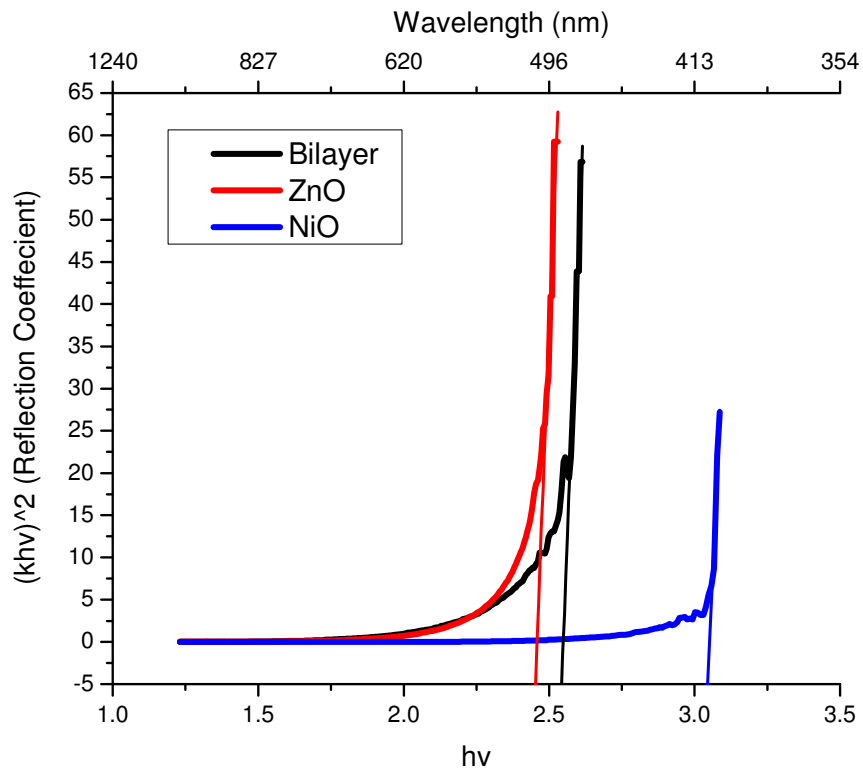


Figure 28. Band gap determination of NiO film, ZnO film and their combination

This slight deviation could be attributed to defects in the films, which can be better understood with Deep Level Transient Spectroscopy (DLTS) that can measure defect densities [125]. However to at least get a partial confirmation of the existence of defects (traps) in the films, the measured IV curves were fitted using the Trap Assisted Tunneling (TAT) model which seemed to fit very well as will be discussed in the next chapter. Following the calculated values of the bandgaps from Fig. 28, the energy band diagram of the bilayer tunnel junction that was studied in this work consisting of the Ni/NiO/ZnO/Cr configuration can be assumed to be as shown in Fig. 29.

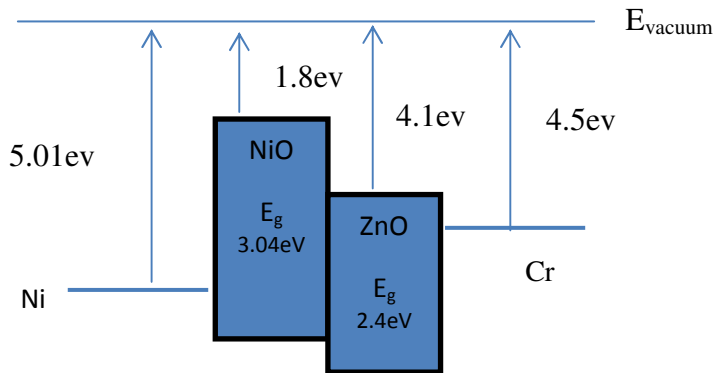


Figure 29. Energy band diagram of a Ni/NiO/ZnO/Cr bilayered tunnel junction device.

CHAPTER 5: EVOLUTION OF MIM TUNNEL JUNCTION DESIGNS

One of the goals in this research is to arrive at an optimum design for the integration of MIM tunnel junctions with antennas to realize a fully functional rectenna for use as an energy conversion device. The geometry of the device and the fabrication method can both positively and negatively affect its performance as experimented exhaustively by Choi et al [100]. Over the course of this research, 3 generations of tunnel junction designs were designed and studied. Each successive design was an improvement from the previous one in various aspects. The first design was the stacked design (SK), however, because of its shortcomings, the stepped design (ST) was developed. Subsequently a Spaced design was developed and fabricated to address issues identified with the stepped design [126].

5.1 Generation 1- Stacked Design (SK)

The stacked structure was one of the first MIM tunnel junction designs to be fabricated and studied in this research. Although the ultimate goal was to use the tunnel junction in a rectenna as a detector, initially, a device was designed as a proof of concept. A schematic of the side view of the device is shown in Fig. 30. The active area is defined by Cr/Au dots directly deposited on top of the insulator film, where the tunnel junction device consists of the vertical path from the top of the dot to the bottom the Ni electrode,

as is detailed below. A schematic process flow is shown in Fig. 31 with the detailed process flows for all the generations given in the appendices.

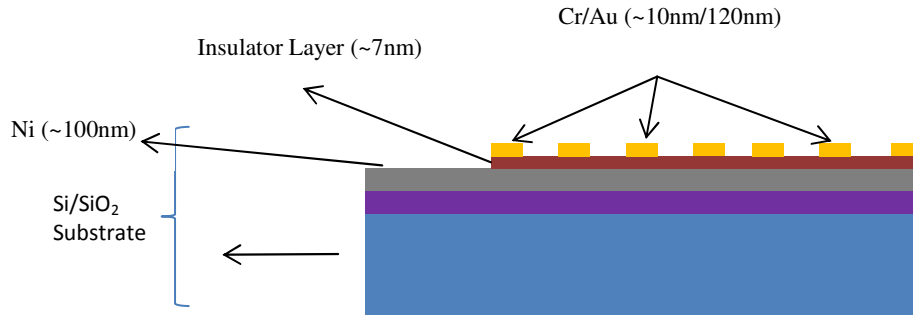
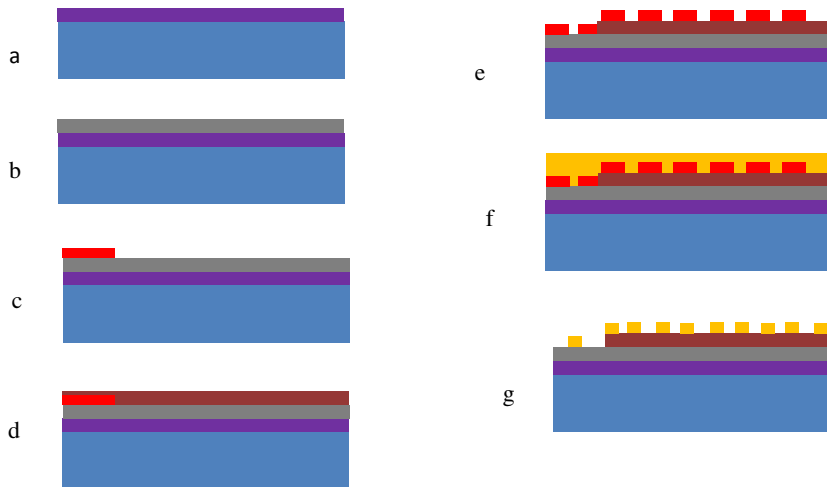


Figure 30. Side view schematic of the SK design



(a) SiO₂ Substrate Conditioning (b) Blanket deposition of Ni (c) masking of the Ni layer for bottom electrode contact (d) deposition of NiO layer (e) masking of NiO layer for Cr/Au dots as top electrode (f) deposition of Cr/Au (g) removal of top electrode mask

Figure 31. Process schematic of the SK device

The SK device was fabricated by blanket depositing a 100nm Ni layer on a clean Si substrate that had about 1µm of thermally grown SiO₂. The Ni layer was then masked on

one side to define the bottom electrode contact. The mask used was either photo resist or Kapton™ tape depending on the urgency of the process and the insulator layer was then deposited atop. Alternatively, in order to not break vacuum between the deposition of the bottom electrode and insulator layer, thereby introducing a contaminated interface, the two layers were deposited one after the other and the bottom contact made by puncturing the insulator layer with the probe through to the bottom electrode. The film was then masked again using a shadow mask with 1mm diameter holes for the top electrode which consisted of 150nm of Cr/Au. Optical lithography was also performed for defining the top electrode area using a chrome mask with openings of 500nm in length. The fabrication of these devices proved to be advantageous in two ways. First, it is a very quick process that enables one to determine the electrical characteristics of the MIM junction. Second, it enabled one to include coupon wafers during the deposition of the insulator layer and thereby perform material analysis of the deposited film. This is not possible in the later generation devices as will soon be identified, but it was not a significant drawback since this type of device was designed for characterizing the electrical and material characteristics of the insulator film.

The obvious drawbacks of the device are that it is not integrable with an antenna, its active area is limited to 1mm which is the size of the holes in the shadow mask and its thickness variations are responsible for variations in the electrical characteristics. But the most important drawback is that the landing of the probes during measurement is affected since excess force can puncture the top electrode. Even variations on the amount of force could cause variations in the current-voltage responses. Electrical measurements performed on these devices with a 7nm NiO film are shown in Fig. 46. As can be seen,

there are large variations among the devices (dots) and the measured results are not representative of the junction. However, due to the ease of fabricating this design it was also used to initially characterize the devices using the ZnO and Bilayer as insulator layers.

5.2 Generation 2- Stepped Design (ST)

To address the issues caused by the probing step of the earlier design, a stepped design was implemented and tested. The ST design side view schematic is shown in Fig. 32 and an optical image shown in Fig. 33. The design initially did not include integration with an antenna since DC characterization was the focus at the time. Inclusion of this type of device along with the “spaced” device for rectenna compatibility was later made while designing the mask for the SP design as will be seen in section 5.3. The ST device was fabricated using optical lithography. First, the areas for gold contact pads were patterned and 150nm of Cr/Au was deposited. After liftoff, the areas for the bottom electrode and insulator were patterned and a Ni layer was deposited following an immediate deposition of a 7nm NiO layer, without breaking vacuum. After the liftoff of this layer, the surface of the device was defined for the active area and top electrode. Since optical lithography was being used, the active area of the top electrode was as small as 10um x 10um deeming the design superior to that of the stacked design. The issue arising from such a fabrication process is that although a small active area is achieved, the process is complicated involving three mask layers and liftoff procedures. The area is also not constant since the top electrode is “overlapped” onto the dielectric and the overlap may not be constant due to alignment errors. Furthermore, since the areas are small, the lift-off process is not easy. The wafer has to be subjected to ultrasonication

which in turn leads to tears on the stepped region of the overlap, which would lead to “opens” in the device. To complicate matters, the issue of an un-oxidized step is prevalent in this design as is revealed in the process flow schematic in Fig. 34 which increased the active area by including the step height. From the I-V responses in Fig. 46, although a higher current is achieved, the variance across devices is abnormally large giving evidence of not only user error but also the continuous oxidation of the step.

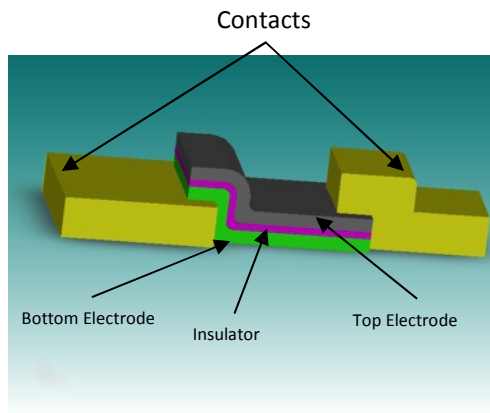


Figure 32. Sideview schematic of ST design

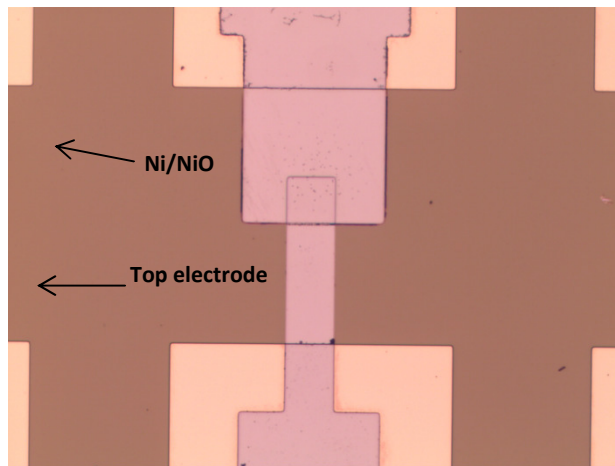
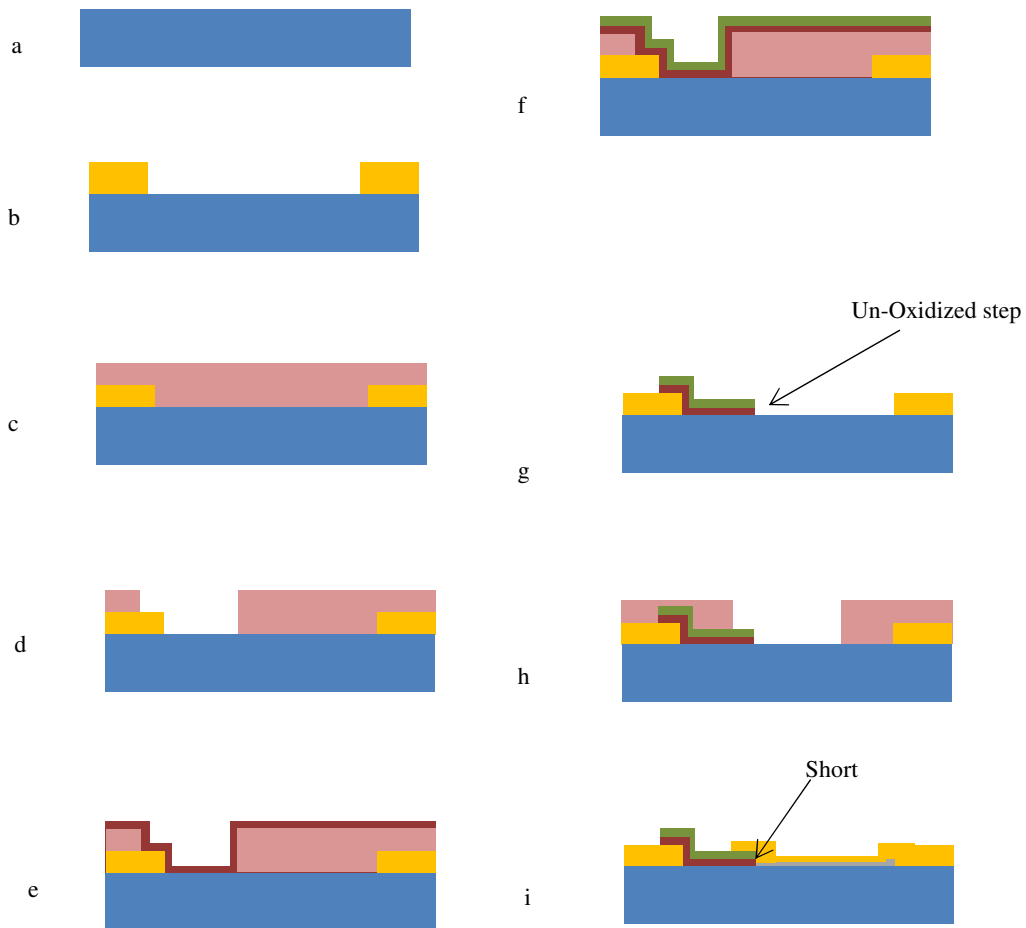


Figure 33. Optical image of ST Design



(a) SiO₂ Substrate Conditioning (b) Pattern and deposition of Cr/Au Contact pads (c) spinning of photoresist (d) patterning of photoresist for bottom Ni electrode and NiO layer (e) deposition of Ni layer (f) deposition of NiO layer (g) liftoff (h) Spinning of photoresist and patterning for top electrode (i) deposition of top electrode.

Figure 34. Process schematic of the ST design

5.3 Generation 3- Spaced Design (SP)

To address the issues mentioned previously, an innovative self-fulfilling design which eliminated the step coverage problem and also presented a relatively well defined active area was implemented. An extra layer was added to the design so that the step could be shielded from the top electrode and could be fabricated using the same photolithographic processes. The bottom electrode and dielectric were fabricated with the same parameters as those mentioned in the previous designs. The extra layer, SiO₂, was sputter deposited and the top electrode was evaporated using thermal evaporation or E-Beam evaporation. The side view schematic and the optical photograph of the fabricated device are shown in Fig. 35. Although the fabrication of this device included an extra layer, it was designed to be self-aligned without requiring much user effort and created a well-defined area which did not include the step height. The SP design included integration with an antenna by way of a Co-Planar Waveguide (CPW). This type of waveguide is typically used where the operating frequency is wideband, not to mention its requirement for planar structures and MIMIC devices [76, 127, 128]. While designing the mask layout for the SP device, consideration was also given to including test features for metrological analyses such as AFM, SEM and FIB in the design. Features for Critical Dimension (CD) checks were also included. This enabled quick checks to verify if a feature with a particular resolution had been exposed and developed correctly without having to check all the device features in every wafer. The alignment marks were modified so that each successive alignment was done with respect to the previous layer and not with the very first layer. It enabled the alignments of the mask for each wafer to be very easy, efficient and quick.

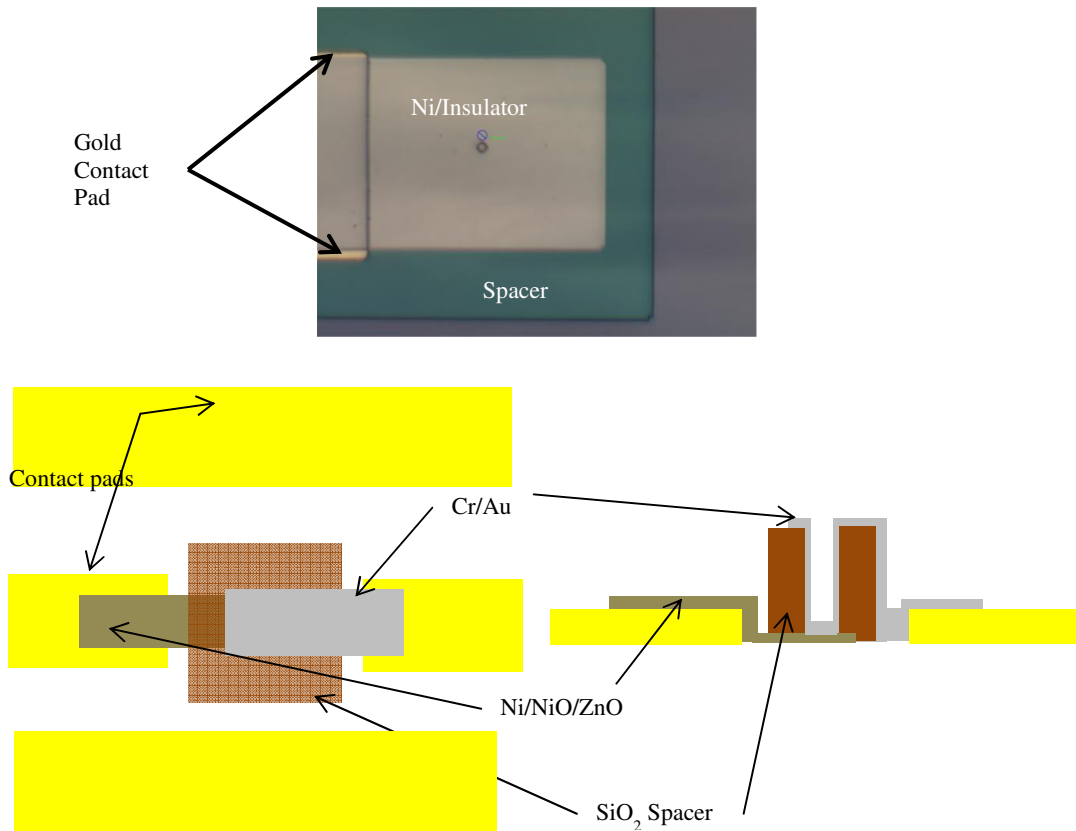


Figure 35. (top) Optical image of the SP design; (bottom) Side view schematic of the SP design.

For AFM test features, all four layers were laid down as individual pads on the wafer. This also served as a tool to measure the deposited thickness of each layer. The SEM and FIB features involved laying long bus lines to dissipate the charging effects that occur during imaging. It also served as good grounding ring surrounding the wafer to minimize electrostatic discharges in the device during handling. A snapshot of the mask layout for the SP design is shown in Fig. 36. The fabrication process steps for the SP device are the same as that of the ST device except that, after the second mask, an extra mask layer is introduced patterning the spacer layer, as shown in Fig. 37. Electrical measurements were performed on a SP device consisting of 10nm NiO as the insulator layer resulting in a decrease in measured current compared to the ST device. The I-V

responses of all 3 generations are plotted in Fig. 46 where the SP responses showed much better stability in the output current among the devices, which was a marked improvement from the ST design. The slight variations among devices can be further minimized by properly mapping the deposition process. One of the problems encountered during the fabrication of this design is that for the $3\mu\text{m}^2$ area, a $3\mu\text{m}^2$ pillar of photoresist is effectively on top of the insulator layers. Therefore if the quality of the insulator films is not adequate, such as poor film adhesion, the insulator layer could get removed during the liftoff process.

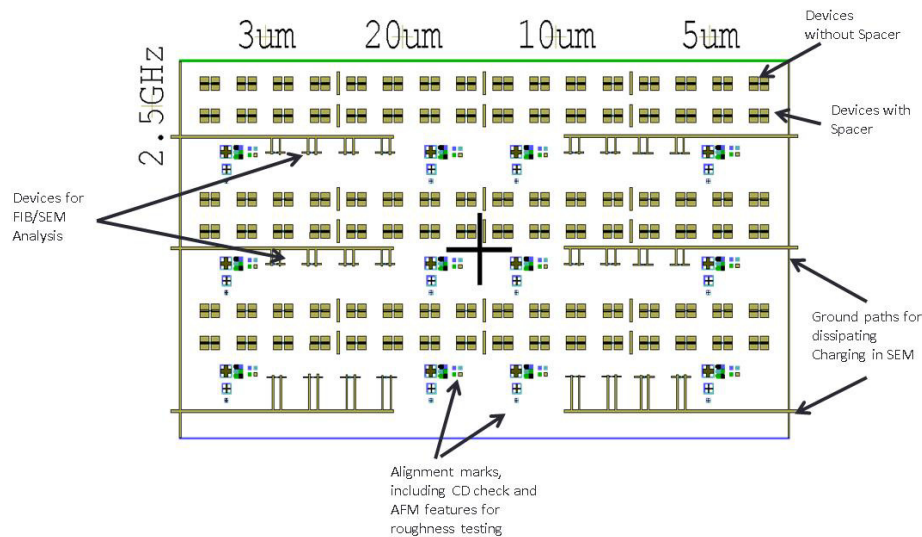
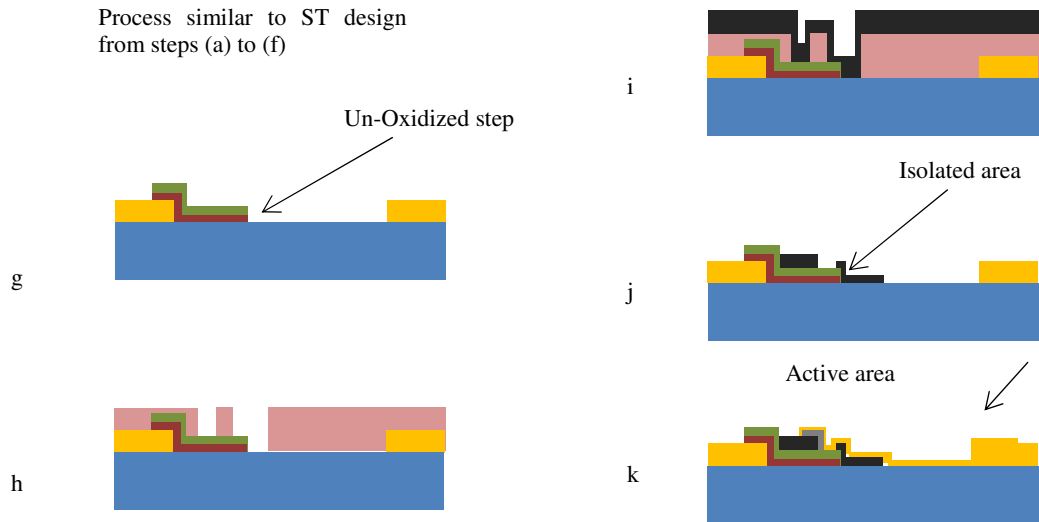


Figure 36. Overall layout of mask showing the functions of each feature

The introduction of the thick spacer layer might also present an intrinsic parasitic capacitance in the device, as shown in Fig. 38. Since the attribute of the device that is most essential is its sensitivity, parasitic capacitances could negatively impact performance of the device as a rectifier. The device measured was the bi-layered one since it was the device of interest.



(g) liftoff after deposition of Ni layer and NiO layer (h) Spinning of photoresist and patterning for SiO₂ spacer (i) deposition of spacer layer (j) liftoff (k) pattern, deposition and liftoff of top electrode revealing active area.

Figure 37. Process flow schematic of the SP design

A capacitive value would inevitably be present in the device which would relate to the RC time constant of the diode. To ensure that the parasitic capacitance is not of concern to the normal rectifying behavior of the device, DC 4 wire measurements were performed to measure how fast the current rises or falls thereby ensuring that its sensitivity is not affected. Fig. 39 shows the measured results when a 500mV bias pulse was toggled on two probes while current was being measured on another two probes. The change in the current when the applied bias voltage is fast enough, suggests that the capacitance of the spacer is not observable and therefore would not substantially affect the sensitivity of the device. From the current-voltage characteristics of the above

designs, it is evident that the most promising candidate is the SP design which has been used in subsequent DC and RF measurements.

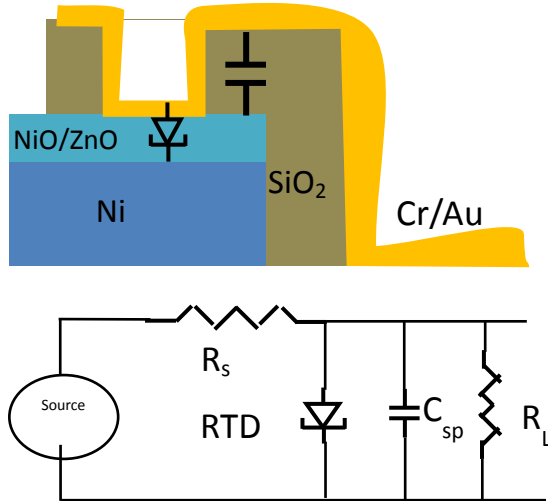


Figure 38. (top) Cross section schematic of parasitic capacitance due to spacer layer. (bottom) Equivalent circuit model of the same. R_s is the series resistance and C_{sp} is the parasitic capacitance due to the SiO₂ spacer.

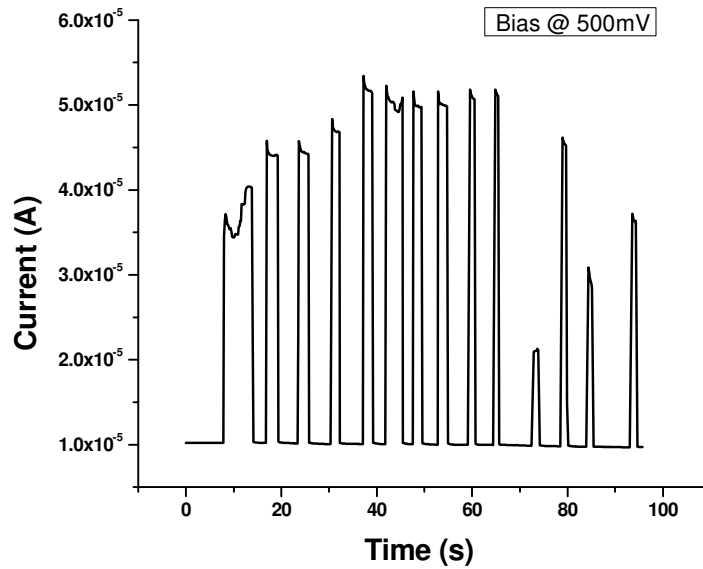


Figure 39. Four wire measurements of the spacer device

CHAPTER 6: DEVICE CHARACTERIZATION

6.1 DC and Low Frequency Measurements

The insulator layer of the MIM tunnel junction is the most important layer for optimum device performance since its quality affects the performance of the entire rectenna device. Changes in the material configuration and design would affect the electrical response of the device either favorably or adversely. The I-V responses were measured using a Keithley 2400 source meter for which a Labview program was written. The devices were measured on a Cascade Probe station shown in Fig. 40. The voltage sensing and the current sourcing are done by the Keithley unit and tungsten probes were attached to micromanipulators which were connected to the ports of the Keithley. A schematic of the setup is shown in Fig. 41.

In chapter four, devices with different electrode combinations were discussed. Fig. 42 shows a comparison of the I-V responses corresponding to each electrode combination. As can be seen, devices with the Ni and Cr as the bottom and top electrodes seem to give the best stability across all devices with the least amount of spread. Continuing the quest for determining a good insulator, the oxygen concentration in the NiO layer was varied and the electrical characteristics measured. Devices were fabricated with the O₂ partial pressures during deposition set at 20%, 33%, 50% and 100%. The

measurements were done on devices of the ST design, fabricated with different O_2 partial pressures during the deposition of the insulator layer and plotted in Fig. 43. The measured current is large due to the large area of the device. The devices that were fabricated with 33% O_2 partial pressure seemed to yield the best results as they exhibited non-linear characteristics and better asymmetry compared to the devices fabricated at the other O_2 partial pressures. The devices fabricated at 100% oxygen partial pressure show almost no non-linear characteristics which can be attributed to the Ni vacancies acting as conduction paths. The devices fabricated at 50% and 20% oxygen partial pressures show similar non-linearities however the current for the 20% device is less, suggesting that oxygen vacancies are acting as traps and are limiting electron transport. The sensitivities of the devices were extracted from the measured data and plotted with respect to O_2 concentration as shown in Fig. 44 and Fig. 45. It can be observed that the devices deposited at 33% oxygen partial pressure resulted in the highest sensitivity with NiO as the insulator layer.

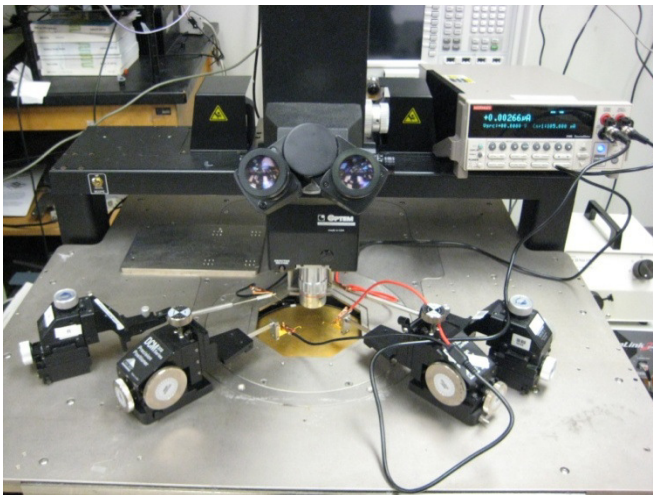


Figure 40. Cascade Probestation with Keithley 2400 Sourcemeter used to conduct DC measurements of the devices

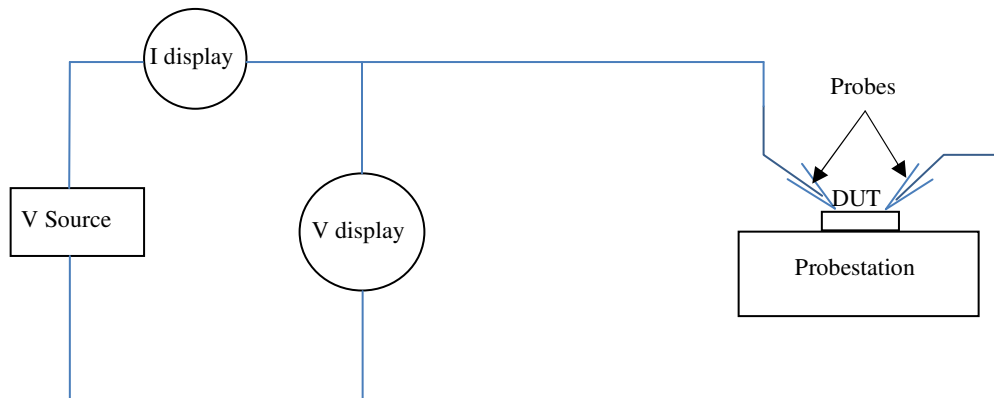


Figure 41. Schematic of the electrical measurement setup

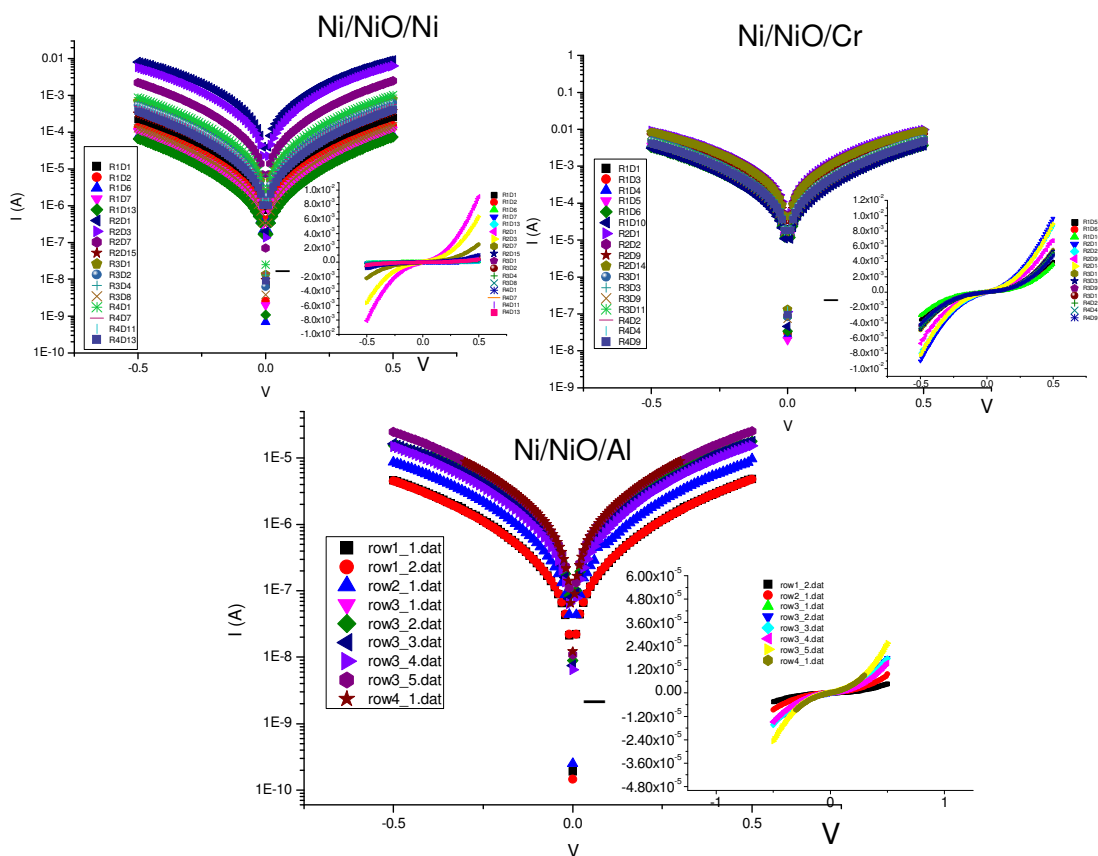


Figure 42. I-V responses for different top electrodes Ni, Al and Cr

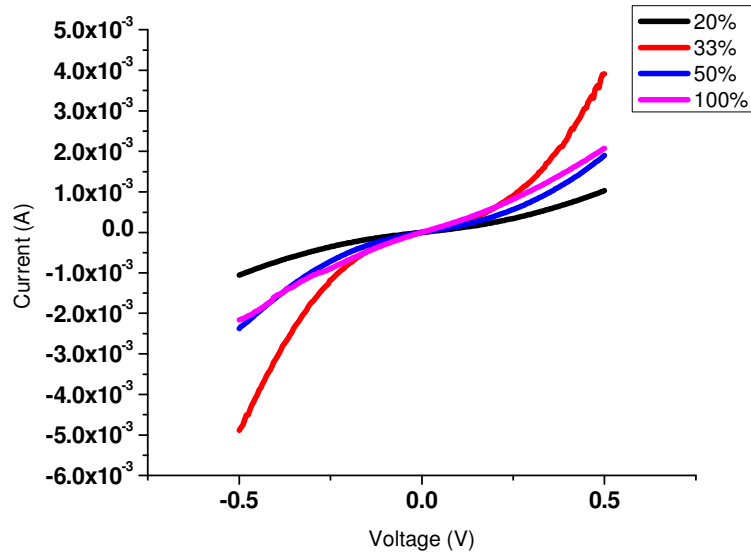


Figure 43. I-V responses of devices fabricated with different oxygen partial pressures.

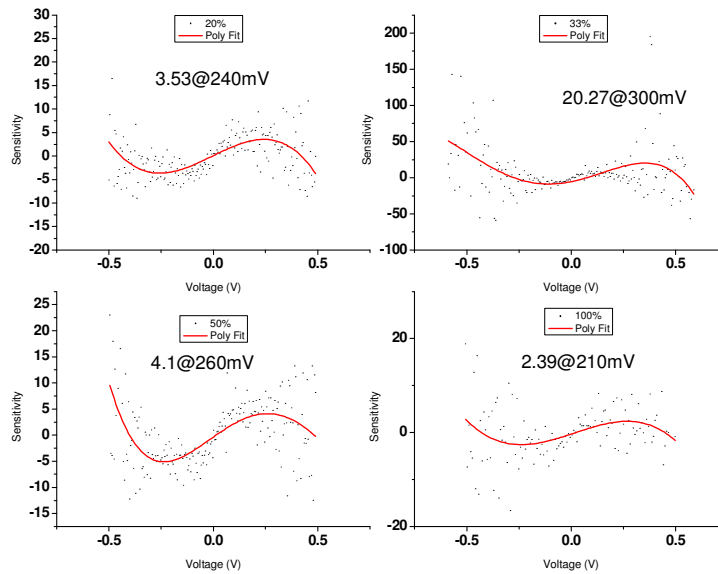


Figure 44. Sensitivities of each device at their fabricated oxygen partial pressures.

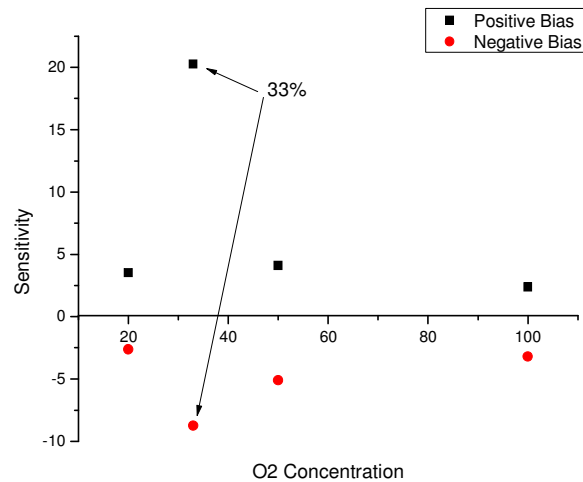


Figure 45. Sensitivities of the device plotted with respect to oxygen partial pressure

As discussed in chapter five, the 3 types of designs (SK, ST and SP) were fabricated and electrical measurements were performed on them. It is evident from the results shown in Fig. 46 that the SP device shows better stability across devices with a reasonable amount of current output as compared to the ST devices.

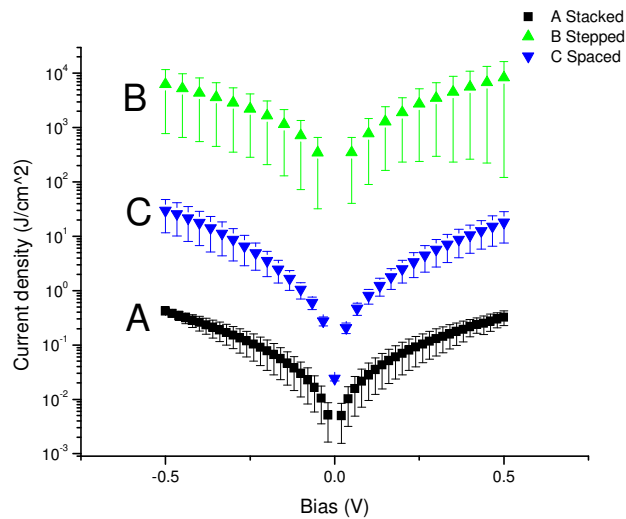


Figure 46. I-V Responses for all 3 generations of devices

The theoretical fit for each structure was also verified using the Simmon's model programmed in Matlab™, shown in Fig. 47, from which the $\Delta\Phi$ was calculated. The values of all the $\Delta\Phi$ s were found to be approximately 0.6eV which corresponded to the work function difference between Ni and Cr. The code for the program is given in Appendix B.

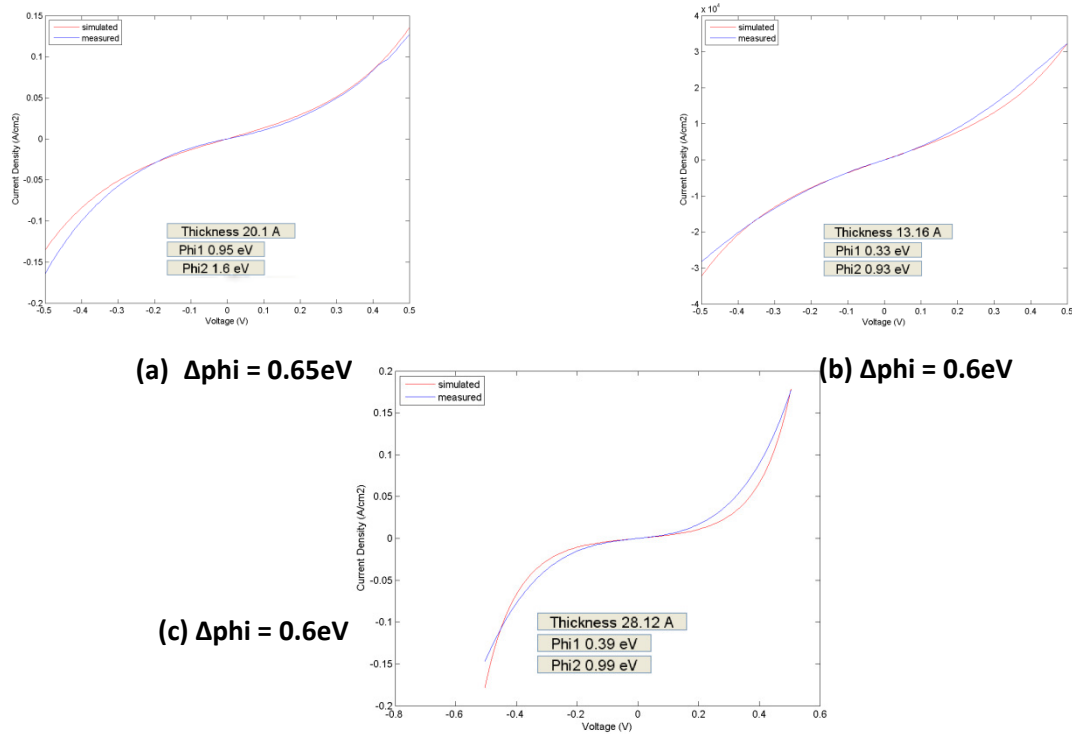


Figure 47. Simmons fit of the 3 devices: (a) Stacked; (b) Stepped; and (c) Spaced

Based on the above studies, 33% NiO layers were used for the fabrication of subsequent devices to evaluate their capability as a detector. The SP design was utilized to fabricate MIM tunnel junction devices in the CPW configuration using NiO, ZnO and their combination as the insulator layers. Comparisons of their I-V responses are given in Fig. 48. The inset shows the I-V response of ZnO devices because their current is too low

to be plotted together. From Fig. 48 it can be observed that the bilayer device has better asymmetry and non-linearity. The measured data was also fitted with the Fowler-Nordheim (FN) model and the Trap Assisted Tunneling (TAT) model to identify which tunneling mechanism was most likely taking place in the insulator layers. $\text{Log}(J/V^2)$ as a function of $(1/V)$ were plotted for the FN fit, and $\text{Log}(J)$ as a function of $(1/V)$ for the TAT fit as shown in Fig. 49 and Fig. 50, where J is the current density in A/cm^2 and V is the applied bias. The FN fit of the NiO based device does not seem to fit well and is giving a positive slope with an unreasonable value for the barrier height. However the ZnO and Bilayer based devices seem to fit well with the FN model, with the ZnO based device fitting better. The TAT fittings of the insulators appear to give more uniform results and more believable barrier heights. A summary of the barrier heights extracted from the two fitting models are given in Table 4 below. Temperature measurements at different voltages were also carried out on the bi-layer samples to confirm if hopping or Hop Assisted Tunneling (HAT) was also a phenomenon present in the working of the device. A Signatone probe-in-a-box system was used and the chuck was modified to pass liquid nitrogen as the coolant. . The Arrhenius plot of $\log(J)$ as a function of temperature is shown in Fig. 52 [96]. It is interesting to note that the linear region (where the current density remains constant) shows little temperature dependence and occurs from around 7°C to 120°C . There appears to be a strong temperature dependence at temperatures above 120°C and below 7°C suggesting that hopping is one of the electron transport mechanisms. There also seems to be a slight decrease and then a sudden increase from 97°C to 143°C hinting that trapped states get thermally excited at 143°C .

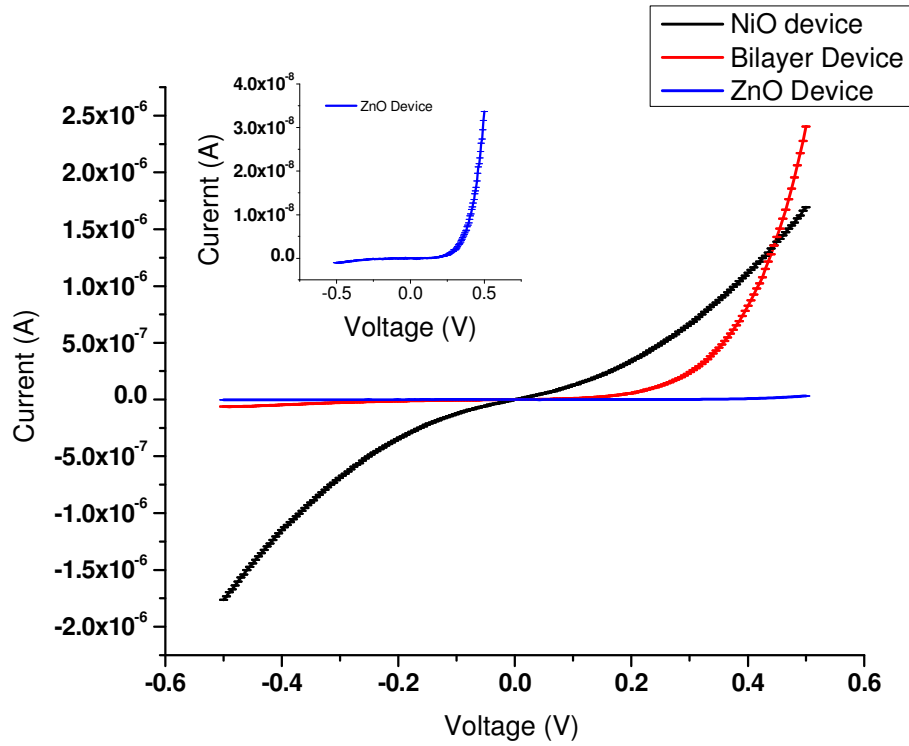


Figure 48. Comparison of I-V responses of devices fabricated with individual films as the insulator layer and the combination of the two.

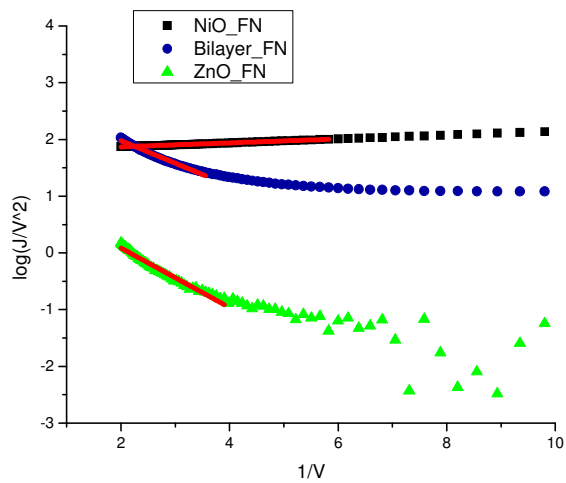


Figure 49. FN fit of the devices

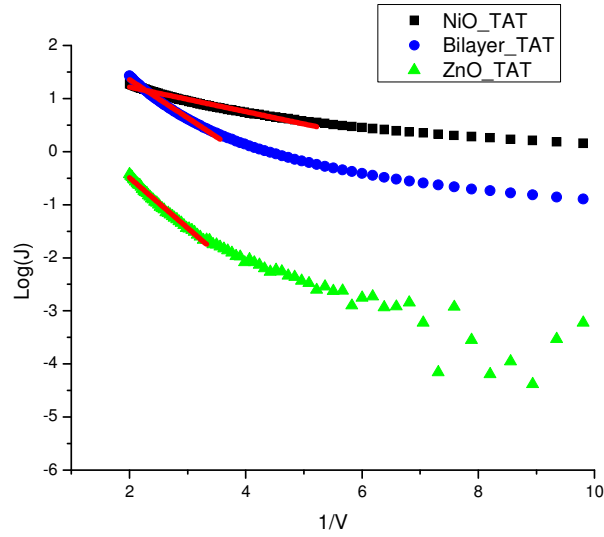


Figure 50. TAT fit of the devices

Table 4 Effective barrier of the devices when fitted with the FN model

	NiO	Bilayer	ZnO
FN	0.03eV	0.3eV	0.5eV
TAT	0.2eV	0.7eV	0.9eV

Measurements were also carried out on the devices to validate their characteristics at low frequencies. The results show excellent rectification characteristics suggesting promising performance at high frequencies which can be seen from Fig. 54 to Fig. 57.

The measurements were performed using a function generator as the signal source and a Rigol Oscilloscope to plot the output response. A schematic of the setup is shown in Fig. 53. It should be noted that the high attenuation of the output in Fig. 57 is attributed to lossy connection in the cables connecting to the DUT.



Figure 51. Modified chuck of Signatone system to allow liquid nitrogen to be used as a coolant.

Sensitivity analyses were performed on the devices to try to validate the theory that a bilayer based MIM tunnel junction would give superior results as a rectifier at high frequencies compared to single layered ones. However, the analyses revealed that each type of device was better suited to a particular function. To be able to rectify efficiently, the diode element of the rectenna should have a high sensitivity at a low turn-on voltage. Fig. 50 shows a distribution of measured devices' sensitivities with respect to their turn on voltages. It can be observed that bi-layered devices do indeed turn on at a lower voltage although they show a lower sensitivity. However some devices show promise of higher sensitivities at low turn on voltages. The yield of such devices can be increased by fine tuning the ZnO layer and increasing the quality of the films. When superimposed on

the application map as illustrated in Fig. 5, the measured sensitivities classify which devices are suitable for which type of application, as depicted in Fig. 59.

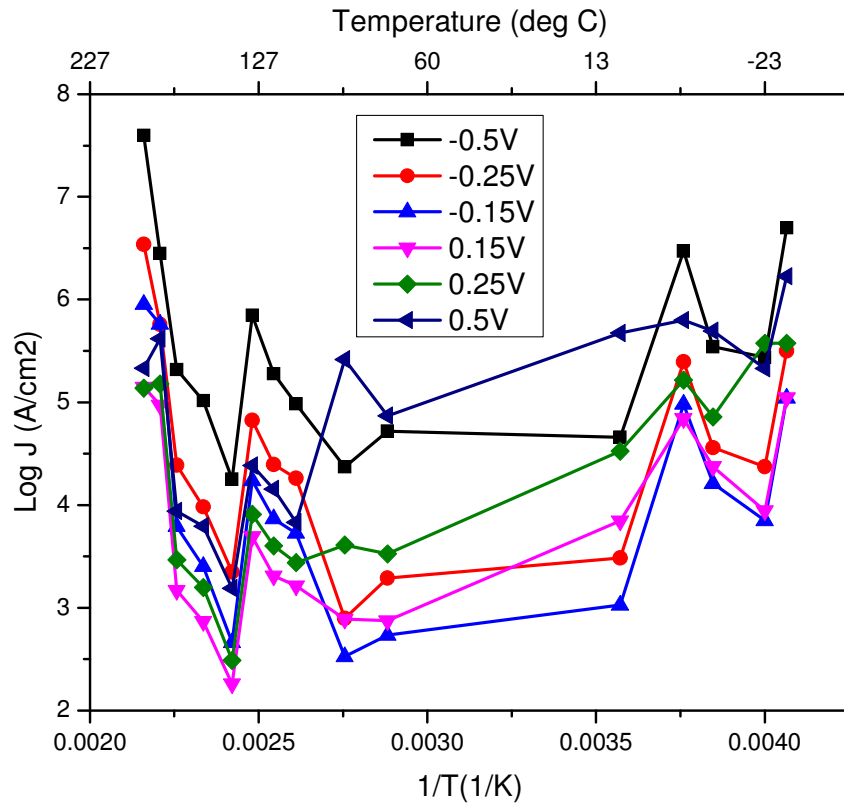


Figure 52. Plot of log (J/V) as a function of temperature at different bias voltage of the Bilayer device.

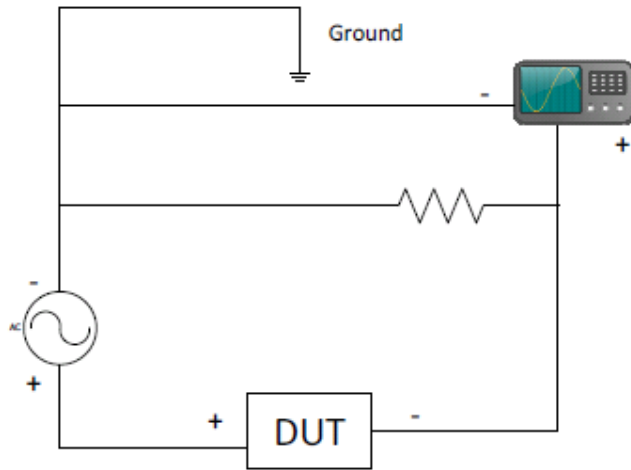


Figure 53. Schematic of the low frequency measurements setup

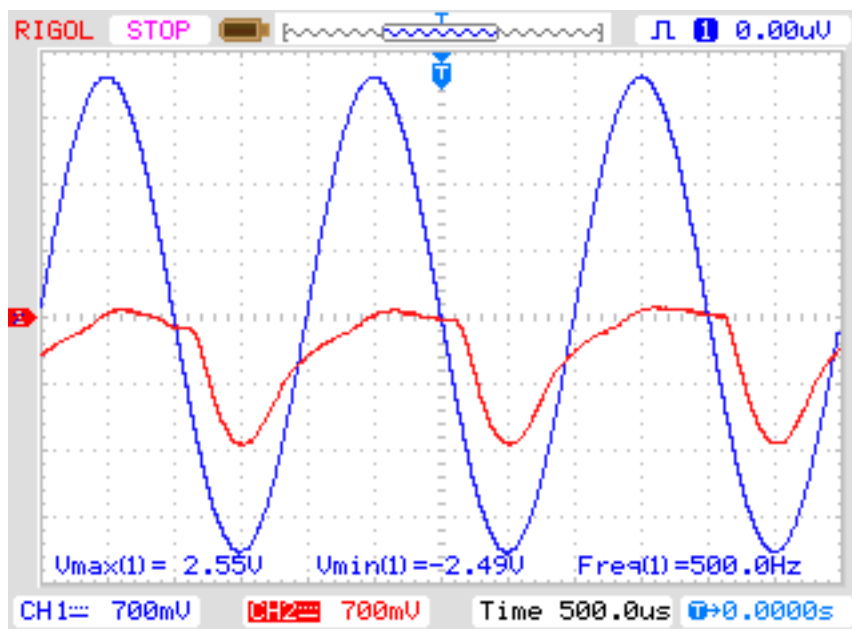


Figure 54. Rectification using the bilayer device at 500Hz

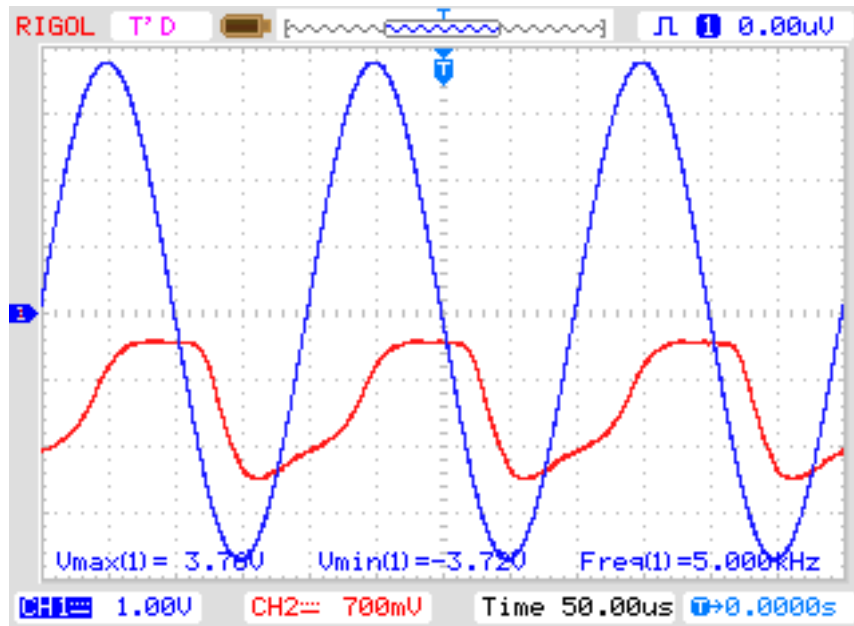


Figure 55. Rectification using the bilayer device at 5 kHz

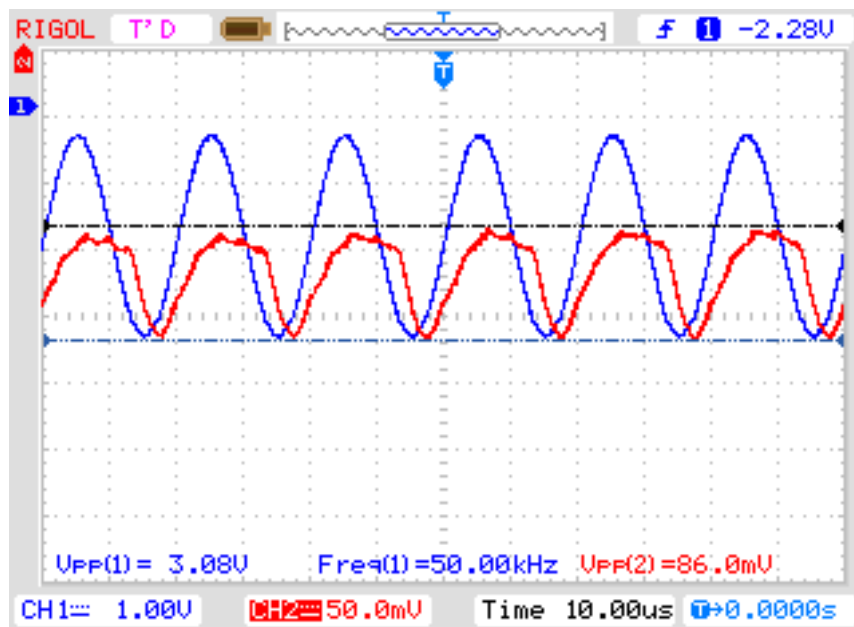


Figure 56. Rectification using the bilayer device at 50 kHz

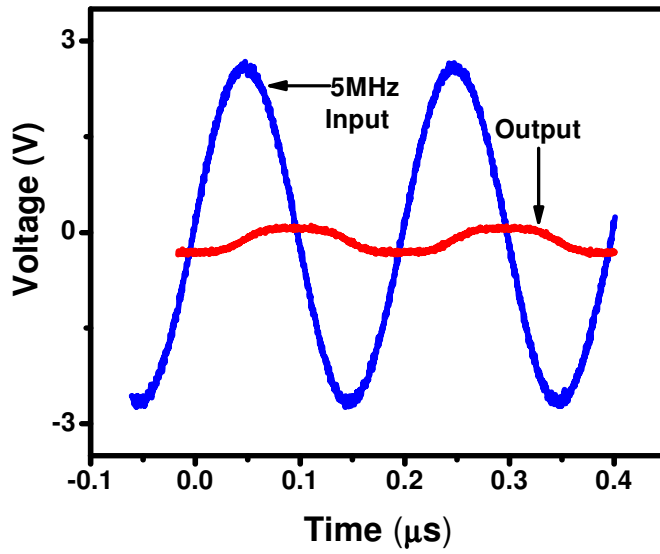


Figure 57. Rectification using the bilayer device at 5 MHz

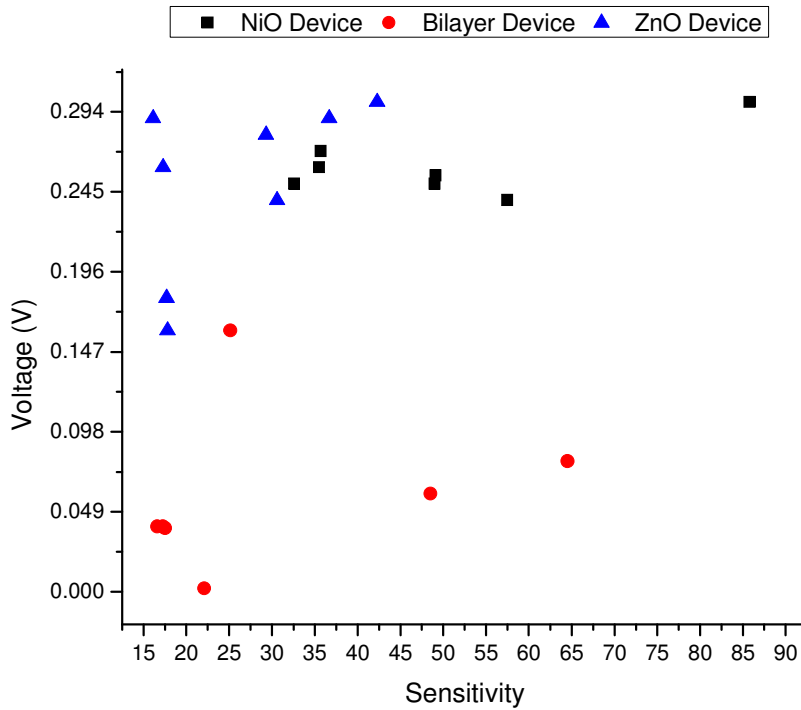


Figure 58. Comparison of sensitivity Vs turn on voltage of the NiO, ZnO and Bilayer based devices

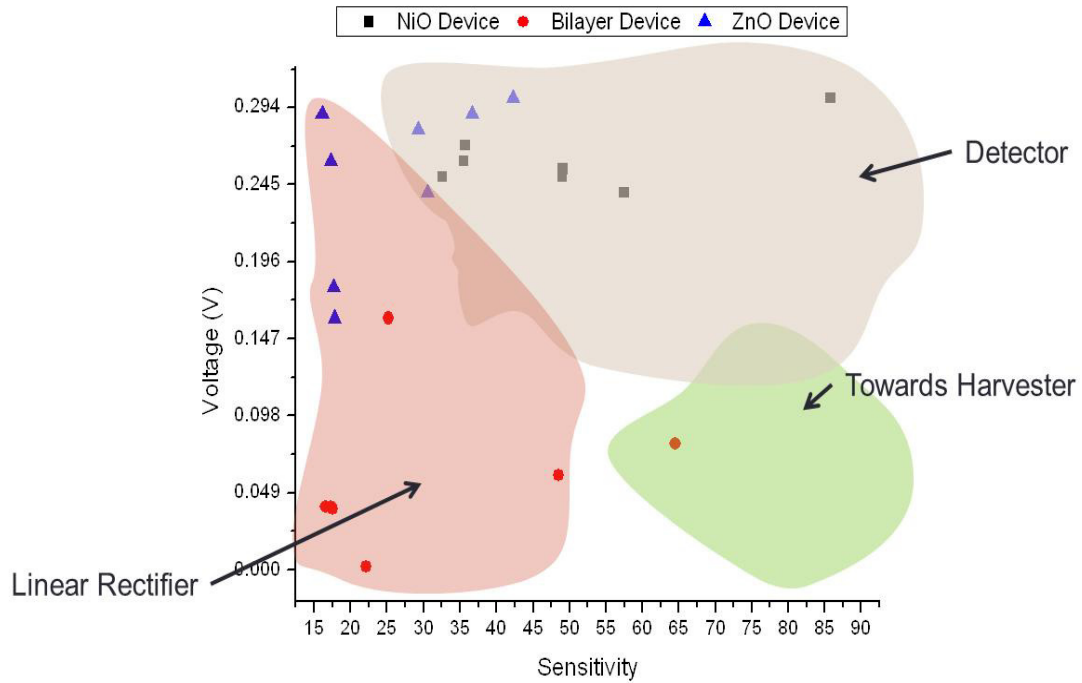


Figure 59. Classification of fabricated devices in this research towards application in high frequency detection

6.2 RF Measurements

To evaluate the performance of the fabricated devices as a rectifier or detector, RF measurements were performed on them. A Vector Network Analyzer (VNA) was used to send the input signals at various frequencies, and two bias tees were used to bias the device at various operating voltages. A schematic of the setup is shown below in Fig. 60 and the results for each device fabricated with their respective material are shown from Fig. 61 to Fig. 64. As mentioned before, the devices were fabricated in a CPW design with the Ground-Signal-Ground (GSG) having pitch sizes 150 μ m-50 μ m-150 μ m, respectively. For frequencies up to 2.5GHz, the gap between the ground and signal lines

was 35 μm . For frequencies above 2.5GHz up to around 100GHz, the gap was 30.4 μm . Since the smallest active area fabricated was 3 μm , the highest operational frequency is around 1GHz, however signal responses were observed up to 10GHz. The RF input was fed to Bias Tee 1 (Picosecond 5543-206) which was then connected to GSG probes to port 1 of the device via a V cable. The positive terminal of an Agilent E3634A power supply was connected to the DC force of Bias Tee 1. Port 2 of the device was connected to Bias Tee 2 (Picosecond 5542-203) using the GSG probes via a V cable. The negative of the power supply was connected to the negative terminal of the Keithley 2400 meter and the positive terminal was connected to the positive terminal of the power supply ensuring that the Keithley was connected in series with the Bias Tee 2 and the power supply. The measurements were performed at 100MHz, 1GHz and 10GHz and were done by turning on the power supply at a particular bias voltage first, then turning on the RF power and noting the increase in rectified current in the Keithley 2400. The bias voltage was determined using the peak values of the sensitivity analysis. The power and efficiencies were calculated by utilizing the DC resistance values at that particular voltage. Only one bias voltage at two different power levels (316 μW and 1mW) was measured and therefore the results are preliminary. Further measurements at different bias voltage and higher frequencies should be done to better illicit a consolidated idea on the rectification properties of the fabricated devices as will be discussed in chapter seven. When the DC bias is turned on, the current corresponding to that voltage flows in the device. When the RF signal is introduced, the signal is superimposed on the DC voltage and is rectified by the device resulting in an increase in the observed current.

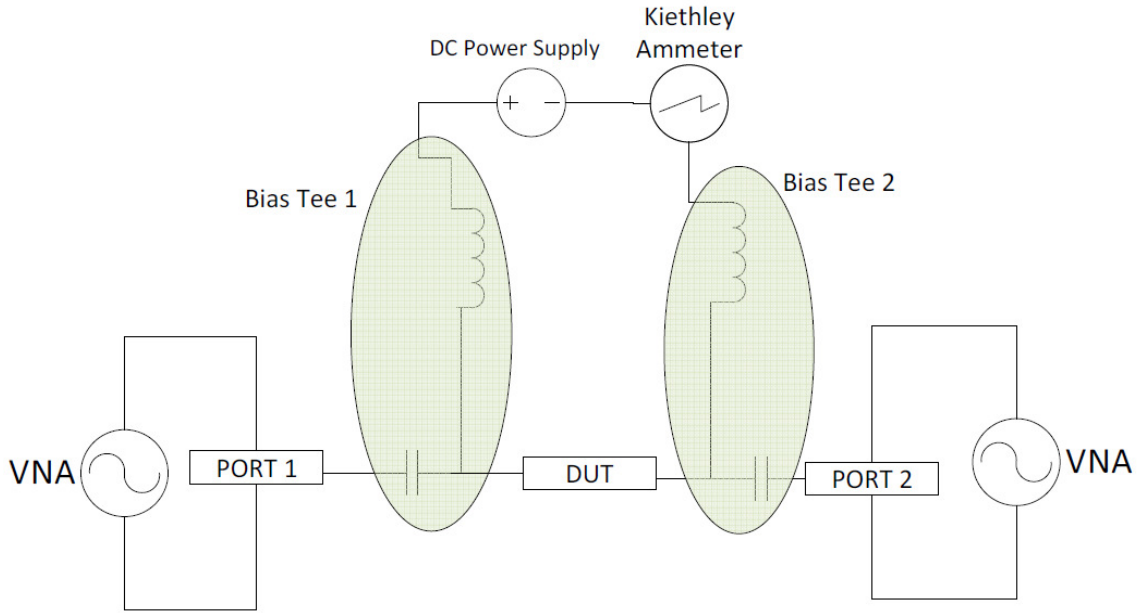


Figure 60. RF Measurement Setup used to detect rectified current with applied bias

From the results, it is interesting to note that the NiO device is very sensitive at lower frequencies and could not handle 1mW. It was also observed that the Bilayer device was very sensitive at power levels of 1mW and below. In the RF responses, the NiO devices registered an excessive enough current with 1mW of input power that they all broke down; as a result, additional measurements were not performed. The ZnO devices were oversensitive with 1mW of input power at 10GHz and 100MHz; however they were stable at 1GHz with 1mW input power. This difference between the two devices could be due to variation within the devices and further study is needed. The bilayer device shows good stability at 10GHz with both 1mW and 316 μ W input power and becomes oversensitive at lower frequencies with an input power of 1mW. It is worthwhile to note that the extreme sensitivity of the bi-layered device is observed by the breakdown of the device at 100MHz even at 316 μ W of input power. This shows promise of the bilayer device being used as a detector with very low input stimulus.

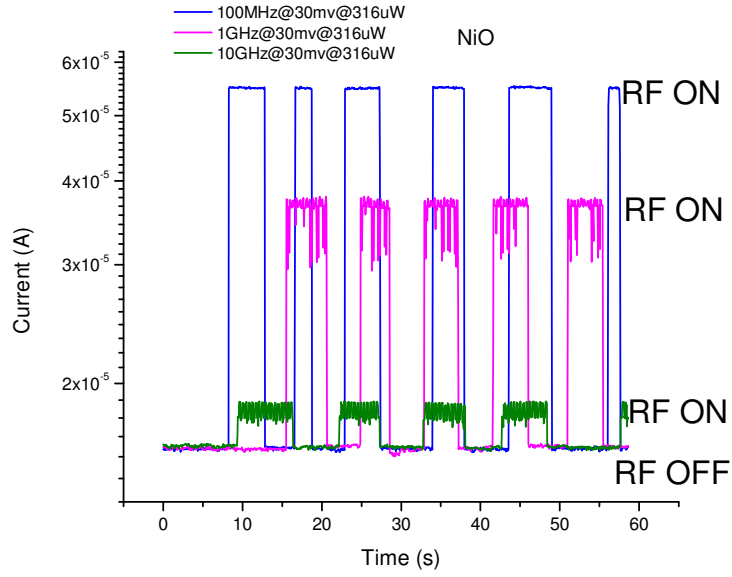


Figure 61. Detected current from NiO devices

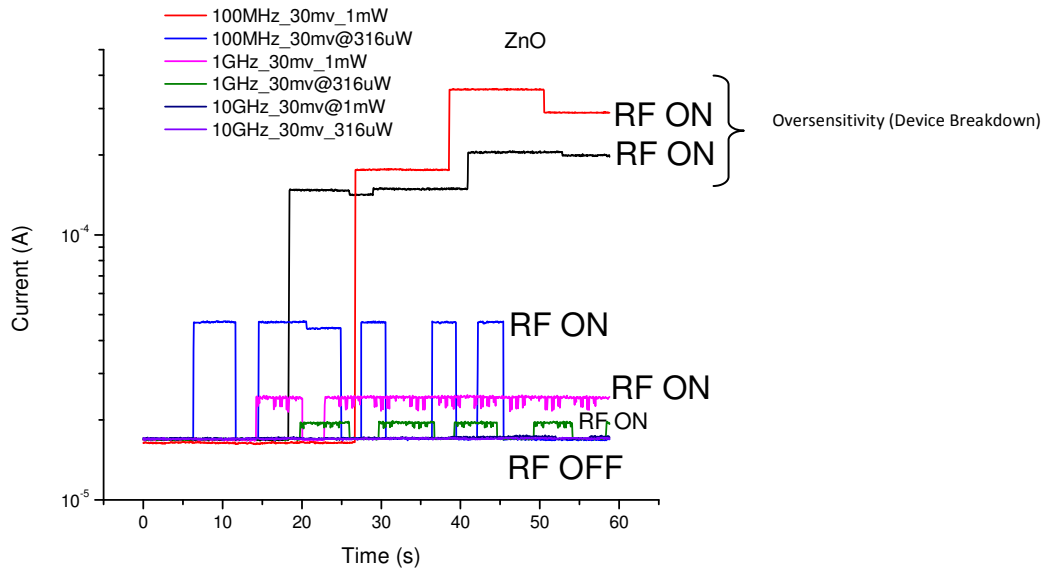


Figure 62. Detected current from ZnO devices

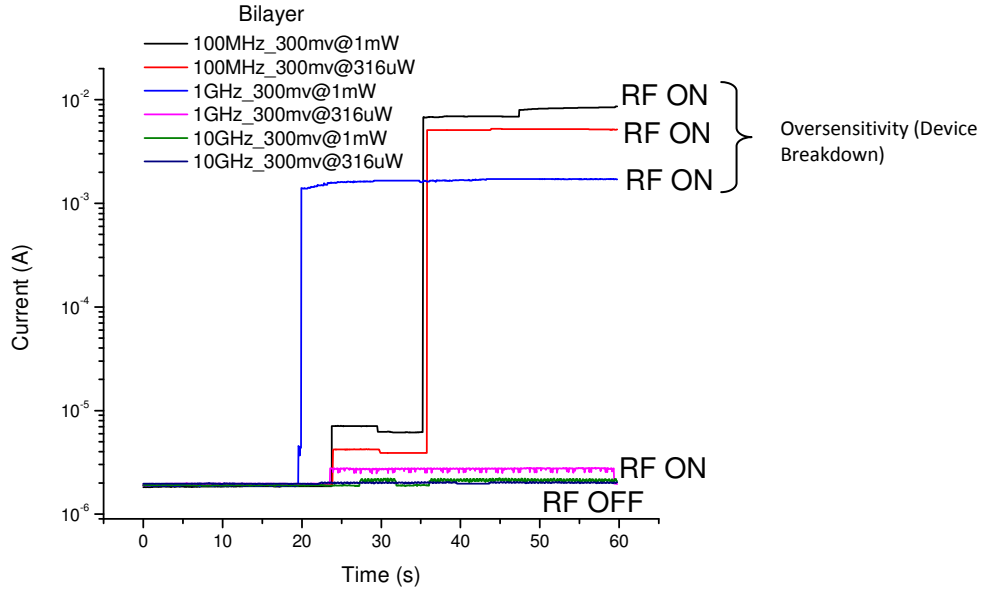


Figure 63. Detected current from Bi-layered devices

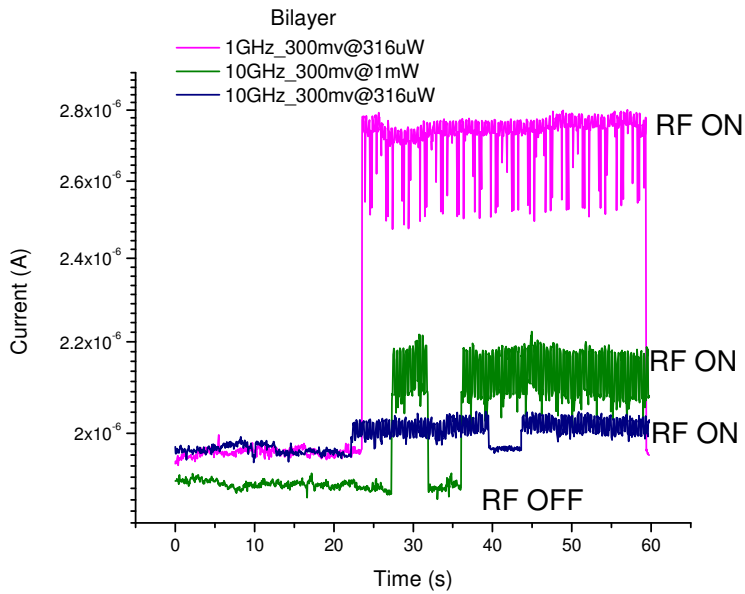


Figure 64. Closeup of the Bilayer devices at 1GHz and 10GHz with 1mW and 316 μ W of input power

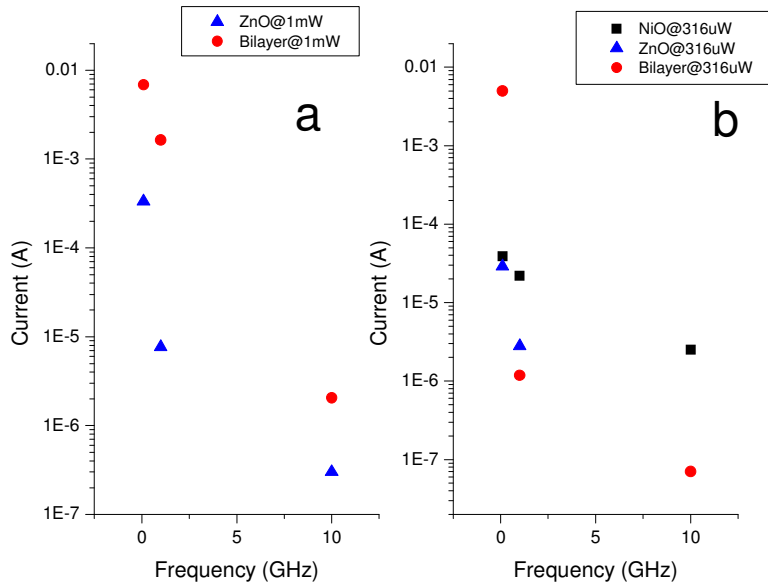


Figure 65. (a) Current vs frequency analysis of NiO, ZnO and bilayer devices with 1mW input power. (b) current vs frequency analysis of NiO, ZnO and bilayer devices with 316µW input power

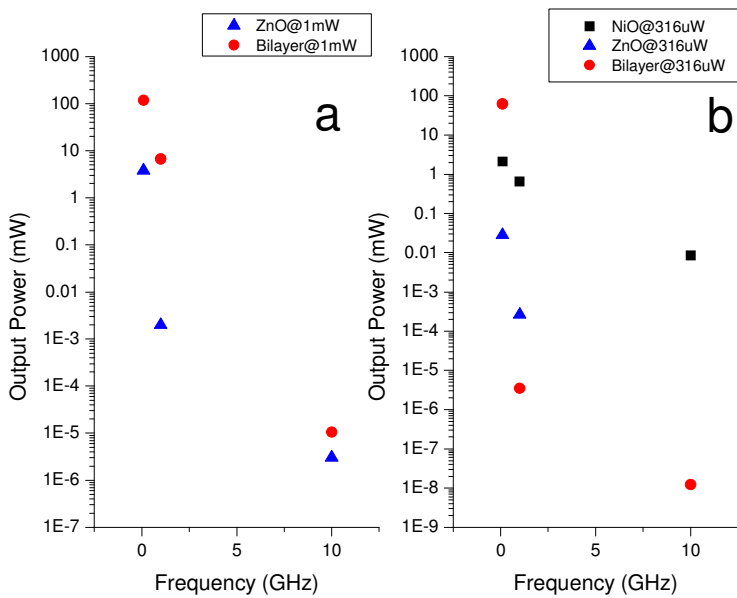


Figure 66. (a) Output power vs frequency analysis of NiO, ZnO and bilayer devices with 1mW input power. (b) output power vs frequency analysis of NiO, ZnO and bilayer devices with 316µW input power

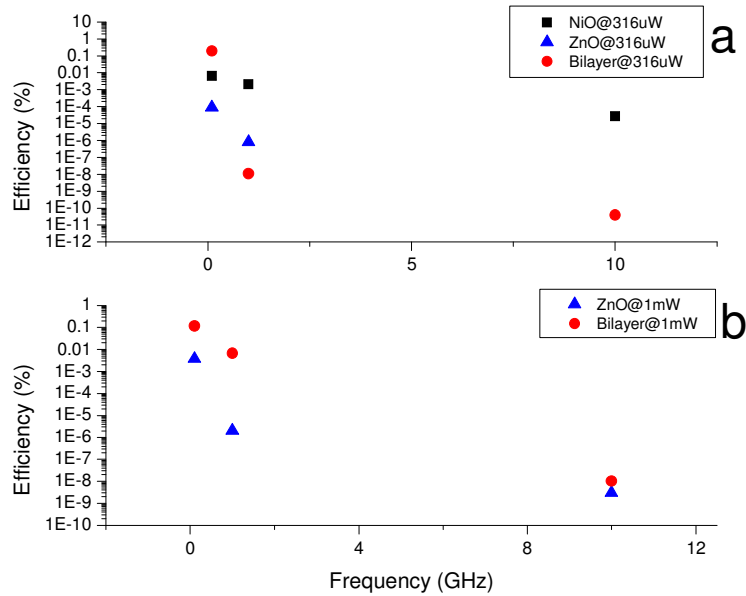


Figure 67. (a) Efficiency vs frequency analysis of NiO, ZnO and bilayer devices with 1mW input power. (b) efficiency vs frequency analysis of NiO, ZnO and bilayer devices with 316µW input power.

Fig. 65 to Fig. 67 show the variation of the devices with respect to output current, output power and efficiency, respectively, as a function of frequency. With 1mW of input power, the bilayer device shows higher current at 100MHz, 1GHz and 10GHz. With a lower input power the bilayer device still exhibits a higher current at low frequencies however; the NiO device proves to be more sensitive at higher frequencies. This is obviously due to the higher impedance of the bilayer and therefore impedance mismatch. The output power and efficiency results reflect the same trend with the bilayer device having a higher efficiency at low frequency and the NiO device having high efficiency at a higher frequency. Table 5 summarizes the RF measurements of the 3 device types. Cells that do not have any values mean that either the device was too sensitive to that input power and broke down, or that it was too noisy to detect any rectified current.

Table 5 Summary of the measured rectified current from each device

Frequency (GHz)		10	1	0.1	
Current (A)	NiO	1mW	--	--	--
		316 μ W	2.50E-06	2.19E-05	3.90E-05
	ZnO	1mW	3.00E-07	7.70E-06	3.36E-04
		316 μ W	--	2.80E-06	2.90E-05
	Bilayer	1mW	2.05E-06	0.00164	0.00688
		316 μ W	7.00E-08	1.18E-06	0.00499
Output Power (mW)	NiO	1mW	--	--	--
		316 μ W	0.00856	0.65707	2.08377
	ZnO	1mW	3.05E-06	0.00201	3.82717
		316 μ W	--	2.66E-04	0.02851
	Bilayer	1mW	1.04E-05	6.67021	117.38931
		316 μ W	1.22E-08	3.45E-06	61.75225
Efficiency (%)	NiO	1mW	--	--	--
		316 μ W	2.71E-05	0.00208	0.00659
	ZnO	1mW	3.05E-09	2.01E-06	0.00383
		316 μ W	--	8.41E-07	9.02E-05
	Bilayer	1mW	1.04E-08	0.00667	0.11739
		316 μ W	3.85E-11	1.09E-08	0.19542

CHAPTER 7: CONCLUSIONS AND RECOMMENDATIONS FOR FUTURE

WORK

MIM tunnel junctions made of different insulator materials (NiO, ZnO and NiO/ZnO) and with different insulator stoichiometries (20%, 33%, 50% and 100%) were designed, fabricated and tested at DC, low and radio frequencies. Three generations of designs (SK, ST, and SP) were fabricated using both optical lithography and conventional shadow mask techniques. It was determined that the design with the spacer showed the greatest reliability. Sensitivity analysis was performed using the I-V responses from DC measurements. The NiO stoichiometry with 33% oxygen during deposition showed the best stability and the highest sensitivity. The diodes with ZnO and NiO/ZnO (bilayer) as the insulator materials showed a very high non linearity and asymmetry, however, the bi-layered device exhibited higher out current characteristics. An application criterion, based on sensitivity and turn-on voltage, for applications as a linear rectifier, detector and energy harvester, was developed to help engineer a device that can function at a desired level. It was found that the bilayer device seemed to be suitable for applications of both the linear rectifier and detector and possibly an energy harvester. Temperature measurements performed on the bilayer device suggest stable operation from 10°C to 120°C. The bi-layered device seemed to behave like a regular rectifier when low frequency signals were fed to it. The responses were very similar to conventional

semiconductor diodes which suggest that this device could possibly replace semiconductor diodes due to its ease of fabrication. The devices also responded well when high frequency signals up to 10GHz were fed to it proving that it can operate in a wide spectrum of frequencies giving reasonable output. The rectified current measured from the bi-layered devices, at high frequencies, was quite high with the highest efficiency of around 0.1% at 100MHz. This performance can be further tuned by fine tuning the thickness and stoichiometry of the bilayer. Further analyses involving different bias voltages and lower power are required to better quantify the rectification capabilities of the devices.

7.1 Future Outlook

The above research in the use of bi-layered tunnel junctions as energy converters is preliminary but promising. A better understanding of the bilayer film with respect to tunneling would greatly benefit the design and fabrication of the device. The variation of current across devices could be attributed to imperfections in the film quality. The lattice match between NiO and ZnO could be improved to increase adhesion between the two and decrease stress. Since even a slight variation of thickness could lead to drastic oscillations in the output current among devices, more uniform methods of deposition of the bilayer could be explored, such as Atomic Layer Deposition. Different stoichiometries of the insulator layer were investigated for the NiO material alone. Further measurements with NiO and ZnO combined, varying the stoichiometry of the NiO, could lead to changes in the tunneling characteristics and might improve the

rectification properties of the device. It would be interesting to inspect the semiconducting properties of the bilayer by performing Hall measurements. Better fits using resonant tunneling models based on traps may be explored to obtain a more accurate barrier height.

Since the most important characteristic of the tunnel junction: its impedance, dictates its matching with the antenna and therefore the efficiency of the device, investigating the effect of varying the stoichiometries on the impedance would help in designing a tunnel junction that can be integrated more efficiently with the antenna. The RF measurements performed require a more exhaustive analysis, based on different applied biases and input power, to better categorize the threshold sensitivities of the devices. Since the smallest area that could be fabricated was $3\mu\text{m}$, a smaller area for operation at frequencies up to 100GHz could be structured by electron beam lithography or Focused Ion Beam (FIB) milling. A useful Design of Experiments (DOE) is suggested in Table 6, below, for possible future research in bi-layered and single layered tunnel junctions.

Table 6 Possible design of experiments to better characterize the bilayer and single layer devices

NiO with Cr/Au dots				ZnO with Cr/Au dots				NiO/ZnO with Cr/Au dots						
O2 conc	Thickness			O2 conc	Thickness			O2 conc	Combined Thickness					
	6nm				6nm				6nm					
10%	IV/CV	AFM, XRD, XPS, Hall		20%	IV/CV	AFM, XRD, XPS, Hall		10%	IV/CV	AFM, XRD, XPS, Hall				
20%	IV/CV			33%	IV/CV			20%	IV/CV					
33%	IV/CV							33%	IV/CV					
50%	IV/CV							50%	IV/CV					
100%	IV/CV							100%	IV/CV					
↓				↓				↓						
Best Concentration Candidate				Best Concentration Candidate				Best Concentration Candidate						
Temperature				Temperature				Temperature						
Thickness	-143C	RT	100C	200C	Thickness	-143C	RT	100C	200C	Combined Thickness	-143C	RT	100C	200C
3nm	IV	IV	IV	IV	3nm	IV	IV	IV	IV	6nm	IV	IV	IV	IV
5nm	IV	IV	IV	IV	5nm	IV	IV	IV	IV	10nm	IV	IV	IV	IV
10nm	IV	IV	IV	IV	10nm	IV	IV	IV	IV	20nm	IV	IV	IV	IV
w.r.t Area				w.r.t Area				w.r.t Area						
Concurrent Experiments														
NiO on CPW Devices				ZnO on CPW Devices				NiO/ZnO on CPW Devices						
Thickness				Thickness				Combined Thickness						
Area	3nm	5nm	10nm	Area	3nm	5nm	10nm	Area	6nm	10nm	20nm			
3um	IV/RF	IV/RF	IV/RF	3um	IV/RF	IV/RF	IV/RF	3um	IV/RF	IV/RF	IV/RF			
5um	IV/RF	IV/RF	IV/RF	5um	IV/RF	IV/RF	IV/RF	5um	IV/RF	IV/RF	IV/RF			
10um	IV/RF	IV/RF	IV/RF	10um	IV/RF	IV/RF	IV/RF	10um	IV/RF	IV/RF	IV/RF			
20um	IV/RF	IV/RF	IV/RF	20um	IV/RF	IV/RF	IV/RF	20um	IV/RF	IV/RF	IV/RF			
↓														
Best Insulator and Area Candidate														
FIB milling for an area of about 1um for checking with 60 and 94GHz														

REFERENCES

1. Holm, R., *The Electric Tunnel Effect across Thin Insulator Films in Contacts*, Journal of Applied Physics, 1951. 22(5): p. 569-574.
2. Esaki, L., *NEW PHENOMENON IN NARROW GERMANIUM PARA-NORMAL-JUNCTIONS*, Physical Review, 1958. 109(2): p. 603-604.
3. Esaki, L., *LONG JOURNEY INTO TUNNELING*, Reviews of Modern Physics, 1974. 46(2): p. 237-244.
4. Wang, S.Y., T. Izawa, and T.K. Gustafson, *COUPLING CHARACTERISTICS OF THIN-FILM METAL-OXIDE-METAL DIODES AT 10.6 MUM*, Applied Physics Letters, 1975. 27(9): p. 481-483.
5. Julliere, M., *TUNNELING BETWEEN FERROMAGNETIC-FILMS*, Physics Letters A, 1975. 54(3): p. 225-226.
6. Frank, R., F. Sewell, and H. Wegener, *Passive film components for Silicon integrated circuits*, Defense technical information center, 1968. 92.
7. Hill, M.T., et al., *Lasing in metal-insulator-metal sub-wavelength plasmonic waveguides*, Optics Express, 2009. 17(13): p. 11107-11112.
8. Krishnan, S., *Thin Film Metal -Insulator-Metal tunnel junctions for millimeter wave detection*. Electrical Engineering. Vol. PhD. 2008, Tampa: University of South Florida.
9. Matyi, G., *Nanoantennas for uncooled, double-band, CMOS compatible, high-speed infrared sensors*, International Journal of Circuit Theory and Applications, 2004. 32(5): p. 425-430.
10. Elwell, C.A., *The development of magnetic tunnel junction fabrication techniques*. Electrical Engineering. Vol. PhD. 2002: University of Cambridge.
11. Heiblum, M., et al., *Characteristics Of Integrated Mom Junctions At Dc And At Optical Frequencies*, IEEE Journal of Quantum Electronics, 1978. 14(3): p. 159-169.

12. Faris, S. M. Gustafson, and J.C. Wiesner, *DETECTION OF OPTICAL AND INFRARED RADIATION WITH DC-BIASED ELECTRON-TUNNELING METAL-BARRIER-METAL DIODES*, IEEE Journal of Quantum Electronics, 1973. QE 9(7): p. 737-745.
13. Gustafson, Tk, S., R. V. Perucca, J. R., *OPTICAL DETECTION IN THIN-FILM METAL-OXIDE-METAL DIODES*, Applied Physics Letters, 1974. 24(12): p. 620-622.
14. Elchinger, G.M., et al., *MECHANISM OF DETECTION OF RADIATION IN A HIGH-SPEED METAL-METAL OXIDE-METAL JUNCTION IN VISIBLE REGION AND AT LONGER WAVELENGTHS*, Journal of Applied Physics, 1976. 47(2): p. 591-594.
15. Masalmeh, S.K., H.K.E. Stadermann, and J. Korving, *Mixing and rectification properties of MIM diodes*, Physica B, 1996. 218(1-4): p. 56-59.
16. Frayne, P.G., N. Chandler, and M.W. Booton, *POINT-CONTACT DIODE SUBMILLIMETER DETECTORS*, Journal of Physics D-Applied Physics, 1978. 11(17): p. 2391-2400.
17. Wiesendanger, E. and F. Kneubuhl, *Thin-film MOM-diodes for infrared detection*, Applied Physics A: Materials Science & Processing, 1977. 13(4): p. 343-349.
18. Frayne, P.G., *VIDEO CRYSTAL DETECTION OF 337MUM MASER RADIATION*, Electronics Letters, 1967. 3(7): p. 338-&.
19. Bernede, J.C. and T. Abachi, *DIFFERENTIAL NEGATIVE-RESISTANCE IN METAL-INSULATOR METAL STRUCTURES WITH AN UPPER BILAYER ELECTRODE*, Thin Solid Films, 1985. 131(3-4): p. L61-L64.
20. Karpov, A., et al., *Low Noise 1 THz–1.4 THz Mixers Using Nb/Al-AlN/NbTiN SIS Junctions*, Applied Superconductivity, IEEE Transactions on, 2007. 17(2): p. 343-346.
21. Tucker, J.R. and M.J. Feldman, *Quantum detection at millimeter wavelengths*, Reviews of Modern Physics, 1985. 57(4): p. 1055-1113.
22. Kwangsik, C., et al., *A Focused Asymmetric Metal–Insulator–Metal Tunneling Diode: Fabrication, DC Characteristics and RF Rectification Analysis*, Electron Devices, IEEE Transactions on, 2011. 58(10): p. 3519-3528.
23. Dees, J.W., *Detection and harmonic generation in the sub-millimeter wavelength region*, Microwave Journal, 1966. 9: p. 48-55.

24. Putley, E.H., *IMPURITY PHOTOCONDUCTIVITY IN N-TYPE INSB*, Proceedings of the Physical Society of London, 1960. 76(491): p. 802-805.
25. Lawson, W.D., et al., *PREPARATION AND PROPERTIES OF HGTE AND MIXED CRYSTALS OF HGTE-CDTE*, Journal of Physics and Chemistry of Solids, 1959. 9(3-4): p. 325-329.
26. Skatrud, P.W.K.a.D.D., *Uncooled Infrared Imaging systems*, in *Semiconductors and Semimetals*1997, Academic Press.
27. Zhao, Y., et al., *Optomechanical uncooled infrared imaging system: Design, microfabrication, and performance*, Journal of Microelectromechanical Systems, 2002. 11(2): p. 136-146.
28. Singh, B.R., *APPLICATION OF METAL-INSULATOR-METAL (MIM) CAPACITORS AS A DC BLOCK IN MICROWAVE INTEGRATED-CIRCUITS*, Thin Solid Films, 1977. 42(3): p. L5-L8.
29. Mondal, J.P., *AN EXPERIMENTAL-VERIFICATION OF A SIMPLE DISTRIBUTED MODEL OF MIM CAPACITORS FOR MMIC APPLICATIONS*, IEEE Transactions on Microwave Theory and Techniques, 1987. 35(4): p. 403-408.
30. Wilke, I., et al., *NANOMETER THIN-FILM NI-NIO-NI DIODES FOR 30 THZ RADIATION*, Applied Physics a-Materials Science & Processing, 1994. 58(4): p. 329-341.
31. Eliasson, B.J., *Metal-Insulator-Metal Diodes for Solar Energy Conversion*. Electrical Engineering. Vol. PhD. 2001, Boulder: University of Colorado.
32. Grover, S. and G. Moddel, *Applicability of Metal/Insulator/Metal (MIM) Diodes to Solar Rectennas*, Photovoltaics, IEEE Journal of, 2011. 1(1): p. 78-83.
33. Grover, S. and G. Moddel, *Engineering the current–voltage characteristics of metal–insulator–metal diodes using double-insulator tunnel barriers*, Solid-State Electronics, 2012. 67(1): p. 94-99.
34. Maraghechi, P., et al., *Enhanced rectifying response from metal-insulator-insulator-metal junctions*, Applied Physics Letters, 2011. 99(25): p. 253503-3.
35. Sanchez, A., et al., *The MOM tunneling diode: Theoretical estimate of its performance at microwave and infrared frequencies*, Journal of Applied Physics, 1978. 49(10): p. 5270-5277.
36. Di Ventra, M., et al., *Indented barrier resonant tunneling rectifiers*, Journal of Applied Physics, 1996. 80(7): p. 4174-4176.

37. Maraghechi, P., et al., *Observation of resonant tunneling phenomenon in metal-insulator-insulator-insulator-metal electron tunnel devices*, Applied Physics Letters, 2012. 100(11): p. 113503-5.
38. Schulz, P.A. and C.E.T.G. da Silva, *Two-step barrier diodes*, Applied Physics Letters, 1988. 52(12): p. 960-962.
39. Oguma, Y., Sashinaka, N., Asada, M., *Terahertz Response with Gradual Change from Square-Law Detection to Photon-Assisted Tunneling in Triple-Barrier Resonant Tunneling Diodes*, Japanese Journal of Applied Physics, 1999. 38: p. L717-L719.
40. Iovan, A., D.B. Haviland, and V. Korenivski, *Diode effect in asymmetric double-tunnel barriers with single-metal nanoclusters*, Applied Physics Letters, 2006. 88(16): p. 163503-163503-3.
41. Hayashi, T., M. Tanaka, and A. Asamitsu, *Tunneling magnetoresistance of a GaMnAs-based double barrier ferromagnetic tunnel junction*, Journal of Applied Physics, 2000. 87(9): p. 4673-4675.
42. Boebinger, G.S., et al., *Direct observation of two-dimensional magnetopolarons in a resonant tunnel junction*, Physical Review Letters, 1990. 65(2): p. 235-238.
43. Chshiev, M., et al., *Magnetic diode effect in double-barrier tunnel junctions*, EPL (Europhysics Letters), 2002. 58(2): p. 257.
44. Almeida, J.M., P. Wisniowski, and P.P. Freitas, *Field detection in single and double barrier MgO magnetic tunnel junction sensors*, Journal of Applied Physics, 2008. 103(7): p. 07E922-07E922-3.
45. Montaigne, F., et al., *Enhanced tunnel magnetoresistance at high bias voltage in double-barrier planar junctions*, Applied Physics Letters, 1998. 73(19): p. 2829-2831.
46. Sze, S.M., *Physics of semiconductor devices*1981: John Wiley & Sons.
47. Sze, S.M., *High-speed semiconductor devices*1990: John Wiley & Sons.
48. WANG, L., *RELIABLE DESIGN OF TUNNEL DIODE AND RESONANT TUNNELLING DIODE BASED MICROWAVE SOURCES*. Electrical Engineering. Vol. PhD. 2011, Glasgow: Glasgow University.
49. Vos, A.D., *Detailed balance limit of the efficiency of tandem solar cells*, Journal of Physics D: Applied Physics, 1980. 13(5): p. 839.

50. Brown, W.C., *Electronic and mechanical improvement of the receiving terminal of a free-space microwave power transmission system*, Raytheon Company, Wayland, MA, Tech. Rep. PT-4964, 1977. CR-135194.
51. Brown, W.C. *An experimental low power density rectenna*. in *Microwave Symposium Digest, 1991., IEEE MTT-S International*. 1991.
52. Yoo, T.W. and K. Chang, *Theoretical and experimental development of 10 and 35 GHz rectennas*, *Microwave Theory and Techniques, IEEE Transactions on*, 1992. 40(6): p. 1259-1266.
53. Brown, W.C., *The History of Power Transmission by Radio Waves*, *Microwave Theory and Techniques, IEEE Transactions on*, 1984. 32(9): p. 1230-1242.
54. Brown, W.C. and J.F. Triner. *Experimental Thin-Film, Etched-Circuit Rectenna*. in *Microwave Symposium Digest, 1982 IEEE MTT-S International*. 1982.
55. Chin, M., et al. *Pt/TiO₂/Ti Metal-insulator-metal Tunnel Diodes for Rectification in an Energy Harvesting System*. in *MRS Fall Meeting*. 2010. ScholarOne.
56. Abdel-Rahman, M.R., F.J. Gonzalez, and G.D. Boreman, *Antenna-coupled metal-oxide-metal diodes for dual-band detection at 92.5 GHz and 28 THz*, *Electronics Letters*, 2004. 40(2): p. 116-118.
57. Bean, J.A., et al., *Thermal infrared detection using dipole antenna-coupled metal-oxide-metal diodes*, *Journal of Vacuum Science & Technology B*, 2009. 27(1): p. 11-14.
58. Esfandiari, P., et al. *Tunable antenna-coupled metal-oxide-metal (MOM) uncooled IR detector (Invited Paper)*. in *Infrared Technology and Applications XXXI*. 2005. Orlando, FL, USA: SPIE.
59. Fumeaux, C., et al., *Nanometer thin-film Ni-NiO-Ni diodes for detection and mixing of 30 THz radiation*, *Infrared Physics & Technology*, 1998. 39(3): p. 123-183.
60. Grover, S., et al., *Traveling-Wave Metal/Insulator/Metal Diodes for Improved Infrared Bandwidth and Efficiency of Antenna-Coupled Rectifiers*, *Nanotechnology, IEEE Transactions on*, 2010. 9(6): p. 716-722.
61. Hu, B.B. and M.C. Nuss, *Imaging with terahertz waves*, *Opt. Lett.*, 1995. 20(16): p. 1716-1718.
62. Kh, S.K., et al., *Investigation of rectenna for microwave power conversion*, *Advances in Natural Sciences: Nanoscience and Nanotechnology*, 2010. 1(3): p. 035002.

63. Ohta, H., et al., *UV-detector based on pn-heterojunction diode composed of transparent oxide semiconductors, p-NiO/n-ZnO*, Thin Solid Films, 2003. 445(2): p. 317-321.
64. Steudel, S., et al., *50 MHz rectifier based on an organic diode*, Nat Mater, 2005. 4(8): p. 597-600.
65. Tiwari, B., et al., *Controlled etching and regrowth of tunnel oxide for antenna-coupled metal-oxide-metal diodes*, Journal of Vacuum Science & Technology B, 2009. 27(5): p. 2153-2160.
66. Twu, B.L. and S.E. Schwarz, *MECHANISM AND PROPERTIES OF POINT-CONTACT METAL-INSULATOR-METAL DIODE DETECTORS AT 10.6-MU*, Applied Physics Letters, 1974. 25(10): p. 595-598.
67. Wilke, I., W. Herrmann, and F.K. Kneubuhl, *INTEGRATED NANOSTRIP DIPOLE ANTENNAS FOR COHERENT 30 THZ INFRARED RADIATION*, Applied Physics B-Lasers and Optics, 1994. 58(2): p. 87-95.
68. Zixu, Z., et al. *Optical rectenna solar cells using graphene geometric diodes. in Photovoltaic Specialists Conference (PVSC), 2011 37th IEEE*. 2011.
69. Pal, B.N., et al., *Pentacene-Zinc Oxide Vertical Diode with Compatible Grains and 15-MHz Rectification*, Advanced Materials, 2008. 20(5): p. 1023-1028.
70. Appleby, R. and R.N. Anderton, *Millimeter-Wave and Submillimeter-Wave Imaging for Security and Surveillance*, Proceedings of the IEEE, 2007. 95(8): p. 1683-1690.
71. Phillips, T.G. and J. Keene, *Submillimeter astronomy [heterodyne spectroscopy]*, Proceedings of the IEEE, 1992. 80(11): p. 1662-1678.
72. Ino, M., T. Ishibashi, and M. Ohmori, *C.W. oscillation with p⁺-n⁺ silicon IMPATT diodes in 200 GHz and 300 GHz bands*, Electronics Letters, 1976. 12(6): p. 148-149.
73. Varani, L., et al., *Numerical modeling of TeraHertz electronic devices*, Journal of Computational Electronics, 2006. 5(2): p. 71-77.
74. Nishizawa, J., K. Motoya, and Y. Okuno, *GaAs TUNNETT Diodes*, Microwave Theory and Techniques, IEEE Transactions on, 1978. 26(12): p. 1029-1035.
75. Radisic, V., et al., *Demonstration of a 311-GHz Fundamental Oscillator Using InP HBT Technology*, Microwave Theory and Techniques, IEEE Transactions on, 2007. 55(11): p. 2329-2335.

76. Radisic, V., et al., *Demonstration of Sub-Millimeter Wave Fundamental Oscillators Using 35-nm InP HEMT Technology*, Microwave and Wireless Components Letters, IEEE, 2007. 17(3): p. 223-225.
77. Siles, J.V. and J. Grajal, *Physics-Based Design and Optimization of Schottky Diode Frequency Multipliers for Terahertz Applications*, Microwave Theory and Techniques, IEEE Transactions on, 2010. 58(7): p. 1933-1942.
78. Brown, E.R., et al., *Oscillations up to 712 GHz in InAs/AlSb resonant-tunneling diodes*, Applied Physics Letters, 1991. 58(20): p. 2291-2293.
79. Brown, E.R., et al., *High-speed resonant-tunneling diodes made from the In_{0.53}Ga_{0.47}As/AlAs material system*, 1990: p. 122-135.
80. Handy, R.M., *Electrode Effects on Aluminum Oxide Tunnel Junctions*, Physical Review, 1962. 126(6): p. 1968-1973.
81. Jun-ichi Shirakashi, K.M., Naruhisa Miura and Makoto Konagai, *Nb/Nb Oxide-Based Planar-Type Metal/Insulator/Metal (MIM) Diodes Fabricated by Atomic Force Microscope (AFM) Nano-Oxidation Process*, Jpn. J. Appl. Phys, 1997. 36: p. L1120-L1122.
82. E. William Cowell III , N.A., Christopher C. Knutson , John F. Conley Jr. , Douglas A. Keszler , Brady J. Gibbons , and John F. Wager, *Advancing MIM Electronics: Amorphous Metal Electrodes*, Adv. Mater., 2011. 23: p. 74-78.
83. Krishnan, S., E. Stefanakos, and S. Bhansali, *Effects of dielectric thickness and contact area on current-voltage characteristics of thin film metal-insulator-metal diodes*, Thin Solid Films, 2008. 516(8): p. 2244-2250.
84. Grossman, E.N., T.E. Harvey, and C.D. Reintsema, *Controlled barrier modification in Nb/NbOx/Ag metal insulator metal tunnel diodes*, Journal of Applied Physics, 2002. 91(12): p. 10134-10139.
85. Guo, W., *Evaluation of e-beam SiO₂ for MIM application*. Chemical and Materials Engineering. Vol. MS. 2010, Edmonton: University of Alberta.
86. Razavy, M., *Quantum theory of tunneling*2003, New Jersey: World Scientific.
87. Kao, K.C., *Dielectric Phenomena in Solids with emphasis on physical concepts of electronic processes*2004: Elsevier Academic Press.
88. Brinkman, W.F., R.C. Dynes, and J.M. Rowell, *TUNNELING CONDUCTANCE OF ASYMMETRICAL BARRIERS*, Journal of Applied Physics, 1970. 41(5): p. 1915-&.

89. Simmons, J.G., *GENERALIZED FORMULA FOR ELECTRIC TUNNEL EFFECT BETWEEN SIMILAR ELECTRODES SEPARATED BY A THIN INSULATING FILM*, Journal of Applied Physics, 1963. 34(6): p. 1793-&.
90. Walmsley, R.B.F.a.D.G., *Tunnelling conductance of clean and doped Al-I-Pb junctions*, J.Phys. C, 1978. 11.
91. Miller, C.W., et al., *Impact of interfacial roughness on tunneling conductance and extracted barrier parameters*, Applied Physics Letters, 2007. 90(4).
92. Simmons, J.G., *ELECTRIC TUNNEL EFFECT BETWEEN DISSIMILAR ELECTRODES SEPARATED BY A THIN INSULATING FILM*, Journal of Applied Physics, 1963. 34(9): p. 2581-&.
93. Miller, C.W., et al., *Origin of the breakdown of Wentzel-Kramers-Brillouin-based tunneling models*, Physical Review B, 2006. 74(21).
94. Lunkenheimer, P., et al., *Correlated barrier hopping in NiO films*, Physical Review B, 1991. 44(11): p. 5927-5930.
95. Ramprasad, R., *Phenomenological theory to model leakage currents in metal-insulator-metal capacitor systems*, Physica Status Solidi B-Basic Research, 2003. 239(1): p. 59-70.
96. Wang, W., T. Lee, and M.A. Reed, *Mechanism of electron conduction in self-assembled alkanethiol monolayer devices*, Physical Review B, 2003. 68(3): p. 035416.
97. Schuegraf, K.F. and C.M. Hu, *RELIABILITY OF THIN SiO₂*, Semiconductor Science and Technology, 1994. 9(5): p. 989-1004.
98. Degraeve, R., B. Kaczer, and G. Groeseneken, *Degradation and breakdown in thin oxide layers: mechanisms, models and reliability prediction*, Microelectronics Reliability, 1999. 39(10): p. 1445-1460.
99. Ghatak, A.K., K. Thyagarajan, and M.R. Shenoy, *A novel numerical technique for solving the one-dimensional Schroedinger equation using matrix approach-application to quantum well structures*, Quantum Electronics, IEEE Journal of, 1988. 24(8): p. 1524-1531.
100. Choi, K., et al., *Geometry enhanced asymmetric rectifying tunneling diodes*, Journal of Vacuum Science & Technology B: Microelectronics and Nanometer Structures. 28(6): p. C6O50-C6O55.
101. Fisher, J.C. and I. Giaever, *TUNNELING THROUGH THIN INSULATING LAYERS*, Journal of Applied Physics, 1961. 32(2): p. 172-&.

102. Wang, C., et al., *I-V characteristics of tantalum oxide film and the effect of defects on its electrical properties*, Thin Solid Films, 2004. 458(1-2): p. 246-250.
103. Havemann, R.H., *Photolithographic fabrication of thin-film metal--oxide--metal diodes with submicrometer-square junction areas*, Journal of Vacuum Science and Technology, 1978. 15(2): p. 389-391.
104. Murarka, S.P. and M.C. Peckerar, *Electronic Materials Science and Technology*, 1989, Academic Press: San Diego. p. 310-320.
105. Jin Tae Kim, S.P., Jung Jin Ju, Seung Koo Park, Min-Su Kim, and Myung-Hyun Lee, *Low-Loss Polymer-Based Long-Range Surface Plasmon-Polariton Waveguide*, IEEE PHOTONICS TECHNOLOGY LETTERS, 2007. 19(18): p. 1374-1376.
106. Jin Tae Kim, S.P., Seung Koo Park, Min-su Kim, Myung-Hyun Lee, and Jung Jin Ju, *Gold Stripe Optical Waveguides Fabricated by a Novel Double-Layered Liftoff Process*, ETRI Journal, 2009. 31(6): p. 778-783.
107. Gupta, S.K., C.M. Singal, and V.K. Srivastava. *Diode Characteristics of a Metal-Insulator-Metal Structure*. ElectroComponent Science and Technology 1976 [cited 3 2]; 119-120].
108. I Hotovy, D.B., S. Hascik and O Nennewitz, *Characterization of NiO thin films deposited by reactive sputtering*, Vacuum, 1998. 50: p. 41-44.
109. Gadzuk, J.W., *RESONANCE TUNNELING THROUGH IMPURITY STATES IN METAL-INSULATOR-METAL JUNCTIONS*, Journal of Applied Physics, 1970. 41(1): p. 286-&.
110. Sasi, B. and K.G. Gopchandran, *Preparation and characterization of nanostructured NiO thin films by reactive-pulsed laser ablation technique*, Solar Energy Materials and Solar Cells, 2007. 91(15-16): p. 1505-1509.
111. Hotovy, I., et al., *Sensing characteristics of NiO thin films as NO₂ gas sensor*, Thin Solid Films, 2002. 418(1): p. 9-15.
112. Hotovy, I., et al., *Preparation of nickel oxide thin films for gas sensors applications*, Sensors and Actuators B: Chemical, 1999. 57(1-3): p. 147-152.
113. Lu, Y.M., et al., *Properties of nickel oxide thin films deposited by RF reactive magnetron sputtering*, Thin Solid Films, 2002. 420-421: p. 54-61.
114. Hotový, I., et al., *Deposition and properties of nickel oxide films produced by DC reactive magnetron sputtering*, Vacuum, 1998. 51(2): p. 157-160.

115. R.Ratnadurai, S.K., E.Stefanakos, D.Y.Goswami, S. Bhansali. *Effects of Dielectric Deposition on the Electrical Characteristics of MIM Tunnel Junctions.* in *Eurosensors XXIV*. 2010. Linz.
116. J. Mannhart, D.H.A.B., H.Y. Hwang, A.J. Millis and J.-M. Triscone, *Two-Dimensional Electron Gases at Oxide Interfaces.*, MRS Bulletin, 2008. 33: p. 1027-1034.
117. Grochowski, J., et al. *Fabrication and characterization of p-NiO/n-ZnO heterojunction towards transparent diode.* in *Electronics Technology (ISSE), 2012 35th International Spring Seminar on*. 2012.
118. Imen, S., et al. *Fabrication and characterization of NiO/ZnO p-n junctions by sol-gel spin coating technique.* in *Renewable Energies and Vehicular Technology (REVET), 2012 First International Conference on*. 2012.
119. Ajimsha, R.S., M.K. Jayaraj, and L.M. Kukreja, *Electrical characteristics of n-ZnO/p-Si heterojunction diodes grown by pulsed laser deposition at different oxygen pressures*, Journal of Electronic Materials, 2008. 37(5): p. 770-775.
120. Ondo-Ndong, R., et al., *Electrical properties of zinc oxide sputtered thin films*, Microelectronics Journal, 2003. 34(11): p. 1087-1092.
121. Ondo-Ndong, R., et al., *Properties of RF magnetron sputtered zinc oxide thin films*, Journal of Crystal Growth, 2003. 255(1–2): p. 130-135.
122. Murphy, A.B., *Band-gap determination from diffuse reflectance measurements of semiconductor films, and application to photoelectrochemical water-splitting*, Solar Energy Materials and Solar Cells, 2007. 91(14): p. 1326-1337.
123. Tan, S.T., et al., *Blueshift of optical band gap in ZnO thin films grown by metal-organic chemical-vapor deposition*, Journal of Applied Physics, 2005. 98(1): p. 013505-5.
124. Kumar, V., et al., *Band gap determination in thick films from reflectance measurements*, Optical Materials, 1999. 12(1): p. 115-119.
125. Nel, J.M., et al., *Fabrication and characterisation of NiO/ZnO structures*, Sensors and Actuators B: Chemical, 2004. 100(1–2): p. 270-276.
126. R. Ratnadurai, S.K., E. Stefanakos, D.Y. Goswami and S. Bhansali. *Nanomanufacturability Of Thin Film MIM Diodes.* in *International Conference on Physics of Emerging Functional Materials*. 2010. Mumbai.

127. Riaziat, M., R. Majidi-Ahy, and I.J. Feng, *Propagation modes and dispersion characteristics of coplanar waveguides*, Microwave Theory and Techniques, IEEE Transactions on, 1990. 38(3): p. 245-251.
128. Rockwell, S., et al. *Characterization and Modeling of Metal/Double-Insulator/Metal Diodes for Millimeter Wave Wireless Receiver Applications*. in *Radio Frequency Integrated Circuits (RFIC) Symposium, 2007 IEEE*. 2007.
129. Krishnan, S., Bhansali, S., Stefanakos, E., and Goswami, Y., 2009, "*Thin film metal-insulator-metal junction for millimeter wave detection*" *Procedia Chemistry*, 1(1), pp. 409-412.
130. Krishnan, S., Bhansali, S., Buckle, K., and Stefanakos, E., 2006, "*Fabrication and Characterization of Thin-film Metal-Insulator-Metal Diode for use in Rectenna as Infrared Detector*," *Mater. Res. Soc. Symp. Proc*, 935, pp. 40-47.

APPENDICES

Appendix A: Process Flow of SK Design

Step 1: Substrate Cleaning

RCA 1 Clean : Remove organic contaminants

Immerse the substrate in 1:1:5 solution of $\text{NH}_4\text{OH} + \text{H}_2\text{O}_2 + \text{H}_2\text{O}$ at 75°C for 15 minutes

Oxide removal: Short Immersion of 1:10 $\text{HF} + \text{H}_2\text{O}$ to remove the native silicon

dioxide formed on the surface of the substrate

RCA 2 Clean : Remove Ionic contaminants

Immerse the substrates in 1:1:5 solution of $\text{HCl} + \text{H}_2\text{O}_2 + \text{H}_2\text{O}$ at 75°C for 15 minutes.

Rinse it with water and N_2 dry.

Step2: Thermal Oxidation

Load sample in oxidation tube furnace. Heat up to 1100°C . Oxygen and Hydrogen flow rate corresponds for growing $1\ \mu\text{m}$ thick oxide.

Step 3: Bottom electrode deposition

DC Sputtering - Ni

Base pressure- $3\ \mu\text{Torr}$ Power- 100 W; Working pressure – 3 mTorr; Sputter time ~ 20mins

Appendix A (Continued)

Step 3: Photolithography

Layer 1- Pattern for bottom electrode contact

Spin coat – Futurrex 1000 PY negative resist:

5 sec at 500 RPM with 168 acceleration

40 sec at 5000 RPM with 504 acceleration

5 sec at 0 RPM with 504 deceleration

Soft bake – Oven; T=120°C for 10 min

UV Expose – Karl Sues Mask aligner; 3 sec at 20mW

Hard bake – Oven; T=100°C for 10 min

Develop – RD 6 developer; Immersion developing at room temperature for 20 sec

Rinse in DI water and N2 dry

Pattern check: Optical Microscope

Thickness check: Dektak Profilometer

Alternatively, a shadow mask may be used such as Kapton™ tape.

Appendix A (Continued)

Step 4: Insulator Deposition

Reactive DC sputtering – NiO

Power- 30W; Working Pressure- 10mTorr; Sputter Time- 7mins

RF Reactive Compound sputtering- ZnO

Power- 100W; Working Pressure- 10mTorr; Sputter Time- 7mins

Step 5: Lift-Off and Ultrasonic clean

Immerse the substrate in Acetone until all the unwanted metals peel off from the substrate. Lift-off may be aided with ultrasonic bath

Check thickness using Profilometer

Step 6: Photolithography

Layer 2- Pattern for top electrode contact

Spin coat – Futurrex 1000 PY negative resist:

5 sec at 500 RPM with 168 acceleration

40 sec at 5000 RPM with 504 acceleration

5 sec at 0 RPM with 504 deceleration

Soft bake – Oven; T=120°C for 10 min

UV Expose – Karl Sues Mask aligner; 3 sec at 20mW

Appendix A (Continued)

Hard bake – Oven; T=100°C for 10 min

Develop – RD 6 developer; Immersion developing at room temperature for 20 sec

Rinse in DI water and N2 dry

Pattern check: Optical Microscope

Thickness check: Dektak Profilometer

Alternatively, a shadow mask may be used such as an Aluminum plate with holes

Step 7: Lift-Off and Ultrasonic clean

Immerse the substrate in Acetone until all the unwanted layers peel off from the substrate. Lift-off may be aided with ultrasonic bath

Check thickness using Profilometer

Appendix B: Process Flow of ST Design

Step 1: Substrate Cleaning

RCA 1 Clean : Remove organic contaminants

Immerse the substrate in 1:1:5 solution of $\text{NH}_4\text{OH} + \text{H}_2\text{O}_2 + \text{H}_2\text{O}$ at 75°C for 15 minutes

Oxide removal: Short Immersion of 1:10 $\text{HF} + \text{H}_2\text{O}$ to remove the native silicon

dioxide formed on the surface of the substrate

RCA 2 Clean : Remove Ionic contaminants

Immerse the substrates in 1:1:5 solution of $\text{HCl} + \text{H}_2\text{O}_2 + \text{H}_2\text{O}$ at 75°C for 15 minutes.

Rinse it with water and N_2 dry.

Step2: Thermal Oxidation

Load sample in oxidation tube furnace. Heat up to 1100°C . Oxygen and Hydrogen flow rate corresponds for growing $1\ \mu\text{m}$ thick oxide.

Step 3: Photolithography

Layer 1- Contacts and Ground

Spin coat – Futurrex 1000 PY negative resist:

5 sec at 500 RPM with 168 acceleration

40 sec at 5000 RPM with 504 acceleration

5 sec at 0 RPM with 504 deceleration

Appendix B (Continued)

Soft bake – Oven; T=120°C for 10 min

UV Expose – Karl Suss Mask aligner; 3 sec at 20mW

Hard bake – Oven; T=100°C for 10 min

Develop – RD 6 developer; Immersion developing at room temperature for 20 sec

Rinse in DI water and N2 dry

Pattern check: Optical Microscope

Thickness check: Dektak Profilometer

Step 4: Metal Deposition

Thermal Evaporation - Cr and Au

Pressure – 3 μ Torr, Current- 70 and 200 A for Cr and Au, respectively; Deposition rate – 0.5 \AA /sec for Cr and 3 \AA /sec for Au.

Step 5: Lift-Off and Ultrasonic clean

Immerse the substrate in Acetone until all the unwanted metals peel off from the substrate. Lift-off aided with ultrasonic bath

Check thickness using Profilometer

Step 6: Photolithography

Layer 2- Bottom Electrode and Insulator

Appendix B (Continued)

Spin coat – Futurrex 1000 PY negative resist:

5 sec at 500 RPM with 168 acceleration

40 sec at 5000 RPM with 504 acceleration

5 sec at 0 RPM with 504 deceleration

Soft bake – Oven; T=120°C for 10 min

UV Expose – Karl Sues Mask aligner; 3 sec at 20mW

Hard bake – Oven; T=100°C for 10 min

Develop – RD 6 developer; Immersion developing at room temperature for 20 sec

Rinse in DI water and N2 dry

Pattern check: Optical Microscope

Thickness check: Dektak Profilometer

Step 7: Metal and Insulator Deposition

DC Sputtering - Ni

Base pressure- 3 μ Torr Power- 100 W; Working pressure – 3 mTorr; Sputter time ~
20mins

Reactive DC sputtering – NiO

Power- 30W; Working Pressure- 10mTorr; Sputter Time- 7mins

Appendix B (Continued)

RF Reactive Compound sputtering- ZnO

Power- 100W; Working Pressure- 10mTorr; Sputter Time- 7mins

Step 8: Lift-Off and Ultrasonic clean

Immerse the substrate in Acetone until all the unwanted layers peel off from the substrate. Lift-off aided with ultrasonic bath

Check thickness using Profilometer

Step 9: Photolithography

Layer 3- Top Electrode

Spin coat – Futurrex 1000 PY negative resist:

5 sec at 500 RPM with 168 acceleration

40 sec at 5000 RPM with 504 acceleration

5 sec at 0 RPM with 504 deceleration

Soft bake – Oven; T=120°C for 10 min

UV Expose – Karl Sues Mask aligner; 3 sec at 20mW

Hard bake – Oven; T=100°C for 10 min

Develop – RD 6 developer; Immersion developing at room temperature for 20 sec

Rinse in DI water and N2 dry

Appendix B (Continued)

Pattern check: Optical Microscope

Thickness check: Dektak Profilometer

Step 10: Metal Deposition

Thermal Evaporation - Cr and Au

Pressure – 3 μ Torr, Current- 70 and 200 A for Cr and Au, respectively; Deposition rate – 0.5 \AA /sec for Cr and 3 \AA /sec for Au.

Step 11: Lift-Off and Ultrasonic clean

Immerse the substrate in Acetone until all the unwanted layers peel off from the substrate. Lift-off aided with ultrasonic bath; Check thickness using Profilometer

Appendix C: Process Flow of SP Design

Step 1: Substrate Cleaning

RCA 1 Clean : Remove organic contaminants

Immerse the substrate in 1:1:5 solution of $\text{NH}_4\text{OH} + \text{H}_2\text{O}_2 + \text{H}_2\text{O}$ at 75°C for 15 minutes

Oxide removal: Short Immersion of 1:10 $\text{HF} + \text{H}_2\text{O}$ to remove the native silicon

dioxide formed on the surface of the substrate

RCA 2 Clean : Remove Ionic contaminants

Immerse the substrates in 1:1:5 solution of $\text{HCl} + \text{H}_2\text{O}_2 + \text{H}_2\text{O}$ at 75°C for 15 minutes.

Rinse it with water and N_2 dry.

Step2: Thermal Oxidation

Load sample in oxidation tube furnace. Heat up to 1100°C . Oxygen and Hydrogen flow rate corresponds for growing $1\ \mu\text{m}$ thick oxide.

Step 3: Photolithography

Layer 1- Contacts and Ground

Spin coat – Futurrex 1000 PY negative resist:

5 sec at 500 RPM with 168 acceleration

40 sec at 5000 RPM with 504 acceleration

5 sec at 0 RPM with 504 deceleration

Appendix C (Continued)

Soft bake – Oven; T=120°C for 10 min

UV Expose – Karl Suss Mask aligner; 3 sec at 20mW

Hard bake – Oven; T=100°C for 10 min

Develop – RD 6 developer; Immersion developing at room temperature for 20 sec

Rinse in DI water and N2 dry

Pattern check: Optical Microscope

Thickness check: Dektak Profilometer

Step 4: Metal Deposition

Thermal Evaporation - Cr and Au

Pressure – 3 μ Torr, Current- 70 and 200 A for Cr and Au, respectively; Deposition rate – 0.5 \AA /sec for Cr and 3 \AA /sec for Au.

Step 5: Lift-Off and Ultrasonic clean

Immerse the substrate in Acetone until all the unwanted metals peel off from the substrate. Lift-off aided with ultrasonic bath

Check thickness using Profilometer

Step 6: Photolithography

Layer 2- Bottom Electrode and Insulator

Appendix C (Continued)

Spin coat – Futurrex 1000 PY negative resist:

5 sec at 500 RPM with 168 acceleration

40 sec at 5000 RPM with 504 acceleration

5 sec at 0 RPM with 504 deceleration

Soft bake – Oven; T=120°C for 10 min

UV Expose – Karl Suess Mask aligner; 3 sec at 20mW

Hard bake – Oven; T=100°C for 10 min

Develop – RD 6 developer; Immersion developing at room temperature for 20 sec

Rinse in DI water and N2 dry

Pattern check: Optical Microscope

Thickness check: Dektak Profilometer

Step 7: Metal and Insulator Deposition

DC Sputtering - Ni

Base pressure- 3 μ Torr Power- 100 W; Working pressure – 3 mTorr; Sputter time ~
20mins

Reactive DC sputtering – NiO

Power- 30W; Working Pressure- 10mTorr; Sputter Time- 7mins

Appendix C (Continued)

RF Reactive Compound sputtering- ZnO

Power- 100W; Working Pressure- 10mTorr; Sputter Time- 7mins

Step 8: Lift-Off and Ultrasonic clean

Immerse the substrate in Acetone until all the unwanted layers peel off from the substrate. Lift-off aided with ultrasonic bath

Check thickness using Profilometer

Step 9: Photolithography

Layer 3- Spacer

Spin coat – Futurrex 1000 PY negative resist:

5 sec at 500 RPM with 168 acceleration

40 sec at 2500 RPM with 504 acceleration

5 sec at 0 RPM with 504 deceleration

Soft bake – Oven; T=120°C for 10 min

UV Expose – Karl Suss Mask aligner; 3 sec at 20mW

Hard bake – Oven; T=100°C for 10 min

Develop – RD 6 developer; Immersion developing at room temperature for 20 sec

Rinse in DI water and N2 dry

Appendix C (Continued)

Pattern check: Optical Microscope

Thickness check: Dektak Profilometer

Step 10: Spacer Oxide Deposition

RF Compound Reactive Sputtering – SiO₂

Base pressure- 3 μ Torr Power- 100 W; Working pressure – 10 mTorr; Sputter time ~ 90mins

Step 11: Lift-Off and Ultrasonic clean

Immerse the substrate in Acetone until all the unwanted layers peel off from the substrate. Lift-off aided with ultrasonic bath

Check thickness using Profilometer

Step 12: Photolithography

Layer 4- Top Contact

Spin coat – Futurrex 1000 PY negative resist:

5 sec at 500 RPM with 168 acceleration

40 sec at 5000 RPM with 504 acceleration

5 sec at 0 RPM with 504 deceleration

Soft bake – Oven; T=120°C for 10 min

Appendix C (Continued)

UV Expose – Karl Süss Mask aligner; 3 sec at 20mW

Hard bake – Oven; T=100°C for 10 min

Develop – RD 6 developer; Immersion developing at room temperature for 20 sec

Rinse in DI water and N₂ dry

Pattern check: Optical Microscope

Thickness check: Dektak Profilometer

Step 13: Metal Deposition

Thermal Evaporation - Cr and Au

Pressure – 3 μ Torr, Current- 70 and 200 A for Cr and Au, respectively; Deposition rate – 0.5 \AA /sec for Cr and 3 \AA /sec for Au.

Step 14: Lift-Off and Ultrasonic clean

Immerse the substrate in Acetone until all the unwanted metals peel off from the substrate. Lift-off aided with ultrasonic bath

Check thickness using Profilometer

Appendix D: Matlab Code for Simmons Fit

Fitting function

```
function [] = simslidev5()
```

```
%% Cleanup
```

```
clc;
```

```
clear all;
```

```
close all;
```

```
%% Parameter Declaration
```

```
global filenamee s phi1 phi2 a A
```

```
filenamee=input('Enter name of excel file (Should have only two columns with only numbers) ', 's');
```

```
% filenamee=('r2d1.xls');
```

```
% s=input('Enter initial Thickness value in A ');
```

```
% phi1=input('Enter initial Phi1 value in eV ');
```

```
% phi2=input('Enter initial Phi2 value in eV ');
```

```
% a=input('Enter initial Area value in um ');
```

```
% A=(a*1e-4)^2;
```

```
s=20.51; %Thickness in angstroms
```

Appendix D (Continued)

```
phi1=0.6; % Potential Barrier one

phi2=1.38; % Potential barrier two

a=1950;

A=(a*1e-4)^2;

Jplot(filenameee,phi1,phi2,s,A);

%% Slider Declaration

S.fh = figure('units','pixels',...

    'position',[1500 300 550 220],...

    'menubar','none',...

    'name','Simmons Fit Control Panel (Rudran{TM})',...

    'numbertitle','off',...

    'resize','on');

S.pb = uicontrol('style','push',...

    'unit','pix',...

    'position',[220 175 130 30],...

    'string','Dont let it go!!');
```


Appendix D (Continued)

```
S.ls(1) = uicontrol('style','list',... %Thickness
```

```
    'unit','pix',...
```

```
    'position',[10 10 130 25],...
```

```
    'min',0,'max',2,...
```

```
    'fontsize',14,...
```

```
    'string',{'Thickness A'});
```

```
S.ls(2) = uicontrol('style','list',... %Phi 1
```

```
    'unit','pix',...
```

```
    'position',[10 50 120 25],...
```

```
    'min',0,'max',2,...
```

```
    'fontsize',14,...
```

```
    'string',{'Phi 1 eV'});
```

```
S.ls(3) = uicontrol('style','list',... %Phi2
```

```
    'unit','pix',...
```

```
    'position',[10 90 120 25],...
```

```
    'min',0,'max',2,...
```

Appendix D (Continued)

```
'fontsize',14,...  
  
'string',{'Phi 2 eV'});  
  
S.ls(4) = uicontrol('style','list',...    %Area  
  
    'unit','pix',...  
  
    'position',[10 140 140 25],...  
  
    'min',0,'max',2,...  
  
    'fontsize',14,...  
  
    'string',{'Area um x um'});  
  
S.sl(1) = uicontrol('style','slide',...  
  
    'unit','pix',...  
  
    'position',[150 10 270 25],...  
  
    'min',1,'max',100,'val',s,'SliderStep',[0.001 0.05]);  
  
S.sl(2) = uicontrol('style','slide',...  
  
    'unit','pix',...  
  
    'position',[150 50 270 25],...  
  
    'min',0,'max',5,'val',phi1,'SliderStep',[0.001 0.005]);
```

Appendix D (Continued)

```
S.sl(3) = uicontrol('style','slide',...  
  
    'unit','pix',...  
  
    'position',[150 90 270 25],...  
  
    'min',0,'max',5,'val',phi2,'SliderStep',[0.001 0.005]);  
  
S.sl(4) = uicontrol('style','slide',...  
  
    'unit','pix',...  
  
    'position',[150 140 270 25],...  
  
    'min',1,'max',1000000,'val',a,'SliderStep',[0.01 0.05]);  
  
S.ed(1) = uicontrol('style','edit',...  
  
    'unit','pix',...  
  
    'position',[450 10 90 25],...  
  
    'fontsize',16,...  
  
    'string',s);  
  
S.ed(2) = uicontrol('style','edit',...  
  
    'unit','pix',...  
  
    'position',[450 50 90 25],...
```

Appendix D (Continued)

```
'fontsize',16,...

'string',phi1);

S.ed(3) = uicontrol('style','edit',...

    'unit','pix',...

    'position',[450 90 90 25],...

    'fontsize',16,...

    'string',phi2);

S.ed(4) = uicontrol('style','edit',...

    'unit','pix',...

    'position',[450 140 90 25],...

    'fontsize',16,...

    'string', a);

set(S.pb,'callback',{ @pb_call,S})

set([S.ed(:);S.sl(:)],'call',{ @curvefit,S}); % Shared Callback.

end

function [] = curvefit(varargin)
```

Appendix D (Continued)

```
%% Parameter Declaration

global filename s phi1 phi2 a A L1 L2 L3 L4

% phiparam=textread('param.txt','%f');

% phi1=hiparam(1);

% phi2=hiparam(2);

% s=hiparam(3);

[h,S] = varargin{[1,3]}; % Get calling handle and structure.

L1 = get(S.sl(1),{'min','max','value'});

L2 = get(S.sl(2),{'min','max','value'});

L3 = get(S.sl(3),{'min','max','value'});

L4 = get(S.sl(4),{'min','max','value'});

%% Slider

switch h

case S.ed(1)

    s = str2double(get(h,'string')); % Numerical edit string.

    Jplot(filename,phi1,phi2,s,A);
```

Appendix D (Continued)

```
if s >= L1{1} && s <= L1{2}

    set(S.sl(1),'value',s) % E falls within range of slider.

else

    set(h,'string',L1{3}) % User tried to set slider out of range.

end

case S.ed(2)

    phi1 = str2double(get(h,'string')); % Numerical edit string.

    Jplot(filenameee,phi1,phi2,s,A);

    if phi1 >= L2{1} && phi1 <= L2{2}

        set(S.sl(2),'value',phi1) % E falls within range of slider.

    else

        set(h,'string',L2{3}) % User tried to set slider out of range.

    end

case S.ed(3)

    phi2 = str2double(get(h,'string')); % Numerical edit string.

    Jplot(filenameee,phi1,phi2,s,A);
```

Appendix D (Continued)

```
if phi2 >= L3{1} && phi2 <= L3{2}

    set(S.sl(3),'value',phi2) % E falls within range of slider.

else

    set(h,'string',L3{3}) % User tried to set slider out of range.

end

case S.ed(4)

    a = str2double(get(h,'string')); % Numerical edit string.

    A=(a*1e-4)^2;

    Jplot(filenameee,phi1,phi2,s,A);

    if a >= L4{1} && a <= L4{2}

        set(S.sl(4),'value',a) % E falls within range of slider.

    else

        set(h,'string',L4{3}) % User tried to set slider out of range.

    end

case S.sl(1)

    s=L1{3};
```

Appendix D (Continued)

```
set(S.ed(1),'string',get(h,'value')) % Set edit to current slider.

Jplot(filenameee,phi 1,phi2,s,A);

case S.sl(2)

    phi1=L2{3};

    set(S.ed(2),'string',get(h,'value')) % Set edit to current slider.

    Jplot(filenameee,phi 1,phi2,s,A);

case S.sl(3)

    phi2=L3{3};

    set(S.ed(3),'string',get(h,'value')) % Set edit to current slider.

    Jplot(filenameee,phi 1,phi2,s,A);

case S.sl(4)

    a=L4{3};

    A=(a*1e-4)^2;

    set(S.ed(4),'string',get(h,'value')) % Set edit to current slider.

    Jplot(filenameee,phi 1,phi2,s,A);

end
```


Appendix D (Continued)

```
end

%% Exporting

function [] = pb_call(varargin)

global table

outname=input('Enter stem name of the datafiles ', 's');

exten='.txt';

pname=strcat(outname,exten);

fid = fopen(pfname, 'w');

fprintf(fid, '%s %s %s %s\r\n', table{1,1:end});

fprintf(fid, '\r\n%f %f %f %f\r\n', table{2,1:end});

fclose(fid);

han=figure(1);

saveas(han, outname, 'tiff')

end
```

Appendix D (Continued)

Plotting Function

```
function [] = Jplot(filenameee,phi1,phi2,s,A)
```

```
global table
```

```
extens='.xlsx';
```

```
xlsfilename=strcat(filenameee,extens);
```

```
RAW=xlsread(xlsfilename,'Sheet1');
```

```
V=RAW(2:end,1);
```

```
len=length(V);
```

```
I=RAW(2:end,2); %Collecting experimental current values
```

```
for i=1:len
```

```
    phi(i)=(phi1+phi2-(V(i)))/2;
```

```
    %phip(i)=(phi1+phi2-(V(i)));
```

```
    J_fwd(i)=(6.2e10/(s^2))*((phi(i)*exp(-1.025*s*sqrt(phi(i))))-((phi(i)+V(i))*exp(-1.025*s*sqrt(phi(i)+V(i))));
```

```
    %J_fwd(i)=(6.2e10/(s^2))*((2*phi(i)*exp(-1.025*s*sqrt(phi(i))))-((phip(i)+V(i))*exp(-1.025*s*sqrt(phip(i))));
```

```
    %J_fwd(i)=J_fwd(i)*A;
```

Appendix D (Continued)

```
J(i)=I(i)/A;

end

% Zerobias_Resistance=V(502)/J_fwd(502)

% Zerobias_Current=J_fwd(502)

are=sqrt(A)/(1e-4);

c={' '};

thickness=strcat('Thickness',c,num2str(s),c,'A');

phi1name=strcat('Phi1',c,num2str(phi1),c,'eV');

phi2name=strcat('Phi2',c,num2str(phi2),c,'eV');

Area=strcat('Area',c,num2str(are),c,'um2');

%% Plotting

figure(1)

graph=plot(V,J_fwd);

set(graph,'Color','red');

xlabel('Voltage (V)')

ylabel('Current Density (A/cm2)')
```

Appendix D (Continued)

hold on

```
plot(V,J);
```

```
h=legend('simulated','measured',2);
```

```
set(h, 'interpreter', 'none')
```

```
uicontrol('style','edit',...
```

```
    'unit','pix',...
```

```
    'position',[300 170 210 25],...
```

```
    'fontsize',16,...
```

```
    'string',thickness);
```

```
uicontrol('style','edit',...
```

```
    'unit','pix',...
```

```
    'position',[300 140 160 25],...
```

```
    'fontsize',16,...
```

```
    'string',phi1 name);
```

```
uicontrol('style','edit',...
```

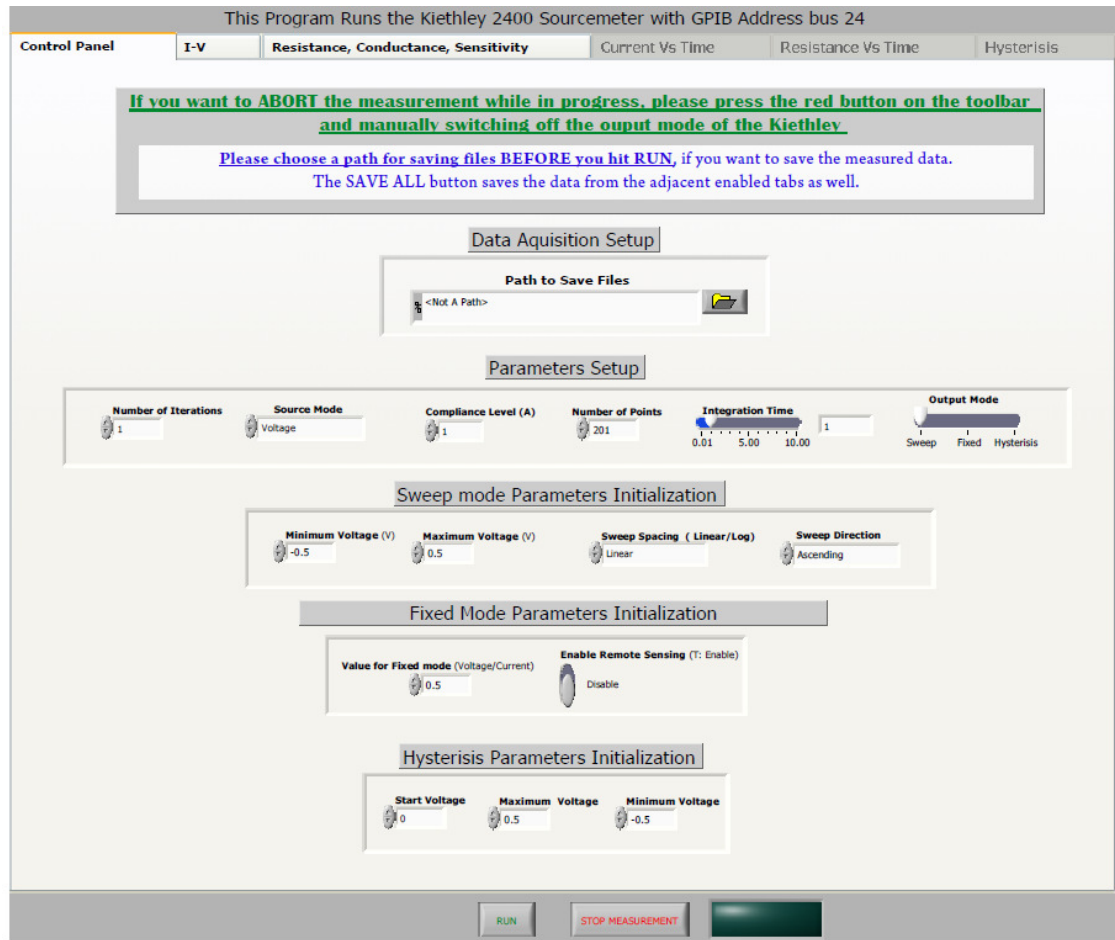
```
    'unit','pix',...
```

Appendix D (Continued)


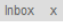
```
'position',[300 110 160 25],...  
  
'fontsize',16,...  
  
'string',phi2name);  
  
uicontrol('style','edit',...  
  
'unit','pix',...  
  
'position',[300 80 210 25],...  
  
'fontsize',16,...  
  
'string',Area);  
  
hold off  
  
% J=transpose(J_fwd);  
  
table={'thickness', 'Area', 'phi1', 'phi2';s, A, phi1, phi2};  
  
% dlmwrite('J.txt',J,'delimiter', '\n');  
  
end
```

Appendix E: Labview Program for Electrical Measurements - Front Control

Panel



Appendix F: Permissions

permission to 2 figures in my PhD thesis  



 **Leo Wang** leo.liqwang@gmail.com
to me 

Nov 12   

Dear Rudy,

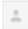

It is glad to know that you want to quote two figures in my PhD thesis!




Here, I confirm that I give you my permission to use the 2 figures(1.1 and 1.2). let me know whether you have any other questions.

Best Wishes,
Leo

Permission to use Fig 4.6 from dissertation   





 **Rudran** rratnadu@mail.usf.edu
to Subbu 


Nov 27 (2 days ago)   

Hi Subbu,
Could you please grant me permission to use fig 4.6 from you dissertation?
Thank You

Regards,

Rudran
Clean Energy Research Center (CERC)
EE Dept.
University of South Florida

 **Subramanian Krishnan**
to me 

Nov 27 (2 days ago)   

Dear Rudran,

This is in response to your email below, in which you have requested permission to reprint, in your upcoming dissertation, one copyrighted figure. I am happy to grant this permission to be used in your dissertation.

Regards,
Subbu.

Appendix F (Continued)

Supplier	Elsevier Limited The Boulevard, Langford Lane Kidlington, Oxford, OX5 1GB, UK
Registered Company Number	1982084
Customer name	Rudran Ratnadurai
Customer address	4506 blue tee ct tampa, FL 33613
License number	3037260815860
License date	Nov 27, 2012
Licensed content publisher	Elsevier
Licensed content publication	Microelectronics Reliability
Licensed content title	Degradation and breakdown in thin oxide layers: mechanisms, models and reliability prediction
Licensed content author	R. Degraeve, B. Kaczer, G. Groeseneken
Licensed content date	October 1999
Licensed content volume number	39
Licensed content issue number	10
Number of pages	16
Start Page	1445
End Page	1460
Type of Use	reuse in a thesis/dissertation
Portion	figures/tables/illustrations
Number of figures/tables /illustrations	1
Format	both print and electronic
Are you the author of this Elsevier article?	No
Will you be translating?	No
Order reference number	
Title of your thesis/dissertation	Development of a Reliable Metal-Insulator-Metal Bilayer Tunnel Junction for Wideband Detectors

Appendix F (Continued)

INTRODUCTION

1. The publisher for this copyrighted material is Elsevier. By clicking "accept" in connection with completing this licensing transaction, you agree that the following terms and conditions apply to this transaction (along with the Billing and Payment terms and conditions established by Copyright Clearance Center, Inc. ("CCC"), at the time that you opened your Rightslink account and that are available at any time at <http://myaccount.copyright.com>).

GENERAL TERMS

2. Elsevier hereby grants you permission to reproduce the aforementioned material subject to the terms and conditions indicated.

3. Acknowledgement: If any part of the material to be used (for example, figures) has appeared in our publication with credit or acknowledgement to another source, permission must also be sought from that source. If such permission is not obtained then that material may not be included in your publication/copies. Suitable acknowledgement to the source must be made, either as a footnote or in a reference list at the end of your publication, as follows: